

Correlated phenomena in graphene at high and low carrier density

Von der Fakultät Mathematik und Physik
der Universität Stuttgart zur Erlangung der Würde eines
Doktors der Naturwissenschaften (Dr. rer. nat.)
genehmigte Abhandlung

vorgelegt von
Johannes Geurs
aus Gerhardsbergen, Belgien

Hauptberichter: Dr. Jurgen H. Smet
Vorsitzender: Prof. Dr. Hans Peter Büchler
Mitberichter: Prof. Dr. Martin Dressel
Tag der Mündlichen Prüfung: 18. Januar 2021

Max-Planck-Institut für Festkörperforschung
Stuttgart, 2021

PER VISIBILIA AD INVISIBILIA

ERASMUS

Contents

| | |
|--|------------|
| Introduction | vii |
| 1 Electronic transport in graphene | 1 |
| 1.1 The band structure of graphene | 1 |
| 1.1.1 Graphene at low densities | 2 |
| 1.1.2 Graphene at high densities | 3 |
| 1.2 Electronic transport in a magnetic field | 6 |
| 1.2.1 Classical Hall effect | 7 |
| 1.2.2 Electrons in two dimensions | 9 |
| 1.2.3 Quantization in strong magnetic fields | 10 |
| 1.2.4 Degeneracy | 12 |
| 1.2.5 Symmetric gauge | 13 |
| 1.2.6 The role of spin | 15 |
| 1.2.7 Landau levels in an electric field | 17 |
| 1.2.8 Quantum Hall resistance | 18 |
| 1.2.9 Disorder in the quantum Hall effect | 20 |
| 1.2.10 Edges of the sample | 22 |
| 1.2.11 Shubnikov-de Haas oscillations | 24 |
| 1.2.12 Quantum Hall effect in graphene | 25 |
| 1.2.13 Beyond the last Landau level | 26 |
| 1.3 Electron hydrodynamics | 29 |
| 1.3.1 Demonstrations of electron hydrodynamics in graphene | 30 |
| 1.4 Electron-hole puddles | 33 |
| 1.5 Superlattice effects in graphene | 34 |
| 1.6 Controlling the carrier concentration | 41 |
| 2 Graphene and graphene devices | 45 |
| 2.1 Fabrication of graphene stacks | 45 |
| 2.1.1 Exfoliation of two-dimensional materials | 45 |
| 2.1.2 Van der Waals heterostructures | 46 |
| 2.1.3 Final steps | 48 |
| 2.2 Highly-doped intercalated graphene | 52 |
| 2.2.1 Doping graphene to the VHS | 52 |
| 2.2.2 Characterization of intercalated graphene | 53 |
| 2.2.3 Contacting and manipulation of intercalated graphene | 53 |
| 2.3 ARPES | 54 |

| | | |
|----------|--|------------|
| 3 | Magnetotransport at the VHS | 61 |
| 3.1 | Pseudogap in cuprate superconductors | 61 |
| 3.1.1 | <i>d</i> -wave gap and pseudogap | 64 |
| 3.1.2 | Transport signatures in the pseudogapped cuprates | 64 |
| 3.2 | Results | 68 |
| 3.3 | Discussion | 69 |
| 3.4 | Outlook | 75 |
| 4 | Viscous rectification in graphene | 77 |
| 4.1 | Principles of operation | 77 |
| 4.2 | Transistors | 81 |
| 4.2.1 | Transistor equation | 81 |
| 4.2.2 | Graphene transistor with electron-hole puddles . . | 83 |
| 4.2.3 | Transistor with four terminals | 85 |
| 4.3 | Results | 88 |
| 4.3.1 | An electronic viscous diode | 90 |
| 4.3.2 | Superlattice effects in rectification | 99 |
| 4.4 | Discussion | 109 |
| 4.4.1 | Diodicity | 109 |
| 4.4.2 | Measurement setup | 109 |
| 4.4.3 | Particle flow | 111 |
| 4.4.4 | Limits of operation | 111 |
| 4.4.5 | Umklapp processes in Moiré superlattices | 113 |
| 4.4.6 | Maximizing diodicity | 113 |
| 4.4.7 | Square versus valve | 114 |
| 4.5 | Outlook | 114 |
| 5 | Conclusion | 115 |
| 6 | Zusammenfassung | 117 |
| 7 | Samenvatting | 129 |
| | Acknowledgements | 131 |
| A | Recipes for van der Waals heterostructure fabrication | 133 |
| B | Measurements with alternating current | 135 |
| B.1 | Principles of lock-in measurements | 135 |

Introduction

Condensed matter physics is the branch of physics that studies electrons in solids. It can be both intensely theoretical, with close connections to group theory, topology, particle physics and atomic physics, and very practical, with discoveries that have transformed our lives, such as the transistor, the light emitting diode and the solid-state laser.

Electronic transport is at the heart of this field of research. By sending currents through a material and measuring voltages at large magnetic field and low temperatures, new electronic phases such as superconductivity and the quantum Hall effect have been observed.

A material that has recently received a torrent of attention is graphene. Graphene is a single layer of carbon, only one atom thick and with remarkable mechanical and electrical properties. Surprisingly, high quality graphene can be isolated simply by mechanical exfoliation with scotch tape. This discovery earned A. Geim and K. Novoselov in 2010 the Nobel Prize in physics. Graphene has become a mainstay in modern condensed matter physics, a flexible playground in which new electronic phenomena can be discovered.

This thesis concerns two new observations in electron transport in graphene, at both very large and very small carrier density.

The first chapter of this thesis introduces some of the properties of graphene, and some of the observables that will be measured. The physics of graphene, the Van Hove singularity and electron hydrodynamics are presented.

The second chapter describes the fabrication and characterization of graphene samples with the desired electron density. Highly doped graphene is produced by processing SiC substrates and intercalating the graphene layer that is formed on top. High quality lowly doped graphene is fabricated by exfoliation and encapsulation in a two-dimensional insulator.

Chapter 3 describes highly doped graphene, in which the carrier density reaches the Van Hove singularity. Many interesting electronic phases have been predicted in this regime, where the effective mass and density of states diverge. We find that as the temperature is lowered, several transport characteristics change behaviour simultaneously. The only other system with similar observations are the cuprates, where this change in transport has been connected with the formation of a pseudogap. This enigmatic phase is linked to the superconductivity at high temperatures

in this material class.

The fourth chapter concerns graphene at low carrier density. If the crystal is clean enough, it has been predicted that the electrons will no longer obey Ohm's law, but flow like water. In this hydrodynamic regime, the electron system will behave like a viscous liquid. We present an electron viscometer, the electronic "Tesla valve", which demonstrates the existence of electron hydrodynamics and its crossover into more conventional transport modes.

We hope this thesis advances the understanding of correlated electron systems, and shows that through careful observations of electronic transport, we can glean knowledge about the nature of electrons in graphene.

The findings in this thesis were also reported in:

- Johannes Geurs, Gihun Ryu, Chengtian Lin, and Jurgen H. Smet. Anomalously large spin-current voltages on the surface of SmB_6 . *Physical Review B*, 100(3):035435, 2019.
- Johannes Geurs, Youngwook Kim, Kenji Watanabe, Takashi Taniguchi, Pilkyung Moon, Jurgen H. Smet. Rectification by hydrodynamic flow in an encapsulated graphene Tesla valve. *arXiv:2008.04862*. Submitted.
- Johannes Geurs, Stefan Link, Pascal Nigge, Andrea Damascelli, Ulrich Starke, Jurgen H. Smet. Pseudogap and Lifshitz transition in graphene at the Van Hove singularity. *In preparation*.

1 Electronic transport in graphene

This chapter introduces the material at the heart of this thesis: graphene. It is a single layer of carbon atoms, with multiple remarkable properties. First, the band structure of graphene will be presented, the basis of our understanding. Later, the effects of magnetic and electric fields are considered. The final sections concern the effects of electron-hole puddles and superlattices imposed on graphene.

The realization of graphene layers will be considered in a separate chapter.

1.1 The band structure of graphene

The electronic properties of graphene [1] are captured in its band structure (Fig. 1). It specifies the allowed values of energy E as a function of wavevector, \mathbf{k} , of an electron in equilibrium in a graphene crystal.

The low-energy bands are shown in the left panel of Fig. 1. At zero temperature, all electrons will be in the states with the lowest energy. Every state with a higher energy will be unoccupied. The energy up to which states are filled is called the Fermi energy E_F . For intrinsic graphene, the Fermi energy lies at the Dirac points, visible in Fig. 1 as the points where the yellow and blue bands touch. The yellow band, completely empty at $T = 0$, is called the conductance band; the blue band, completely filled at $T = 0$, the valence band.

At higher temperature, it is possible for electrons to be thermally excited to an empty state in the conductance band, described by Fermi-Dirac statistics [2]. This leaves a positively charged vacancy in the valence band, called a hole. Both electrons and holes are mobile and contribute to charge transport when an electric field is applied.

The density of states (DOS) describes how many states exist at a given energy. It is shown in the right panel of Fig. 1. At $E = 0$, there are no available states. Away from the Dirac point, the DOS increases linearly. At very high energies ($E \approx \pm 2.7eV$), the DOS diverges to infinity, which is called a Van Hove singularity (VHS). This is visible in the band structure as a saddle point, where the band is flat.

This thesis concerns both graphene at low and high carrier densities. These regimes are discussed separately, below. The methods of changing the carrier concentration in an experiment will be discussed in section 1.6.

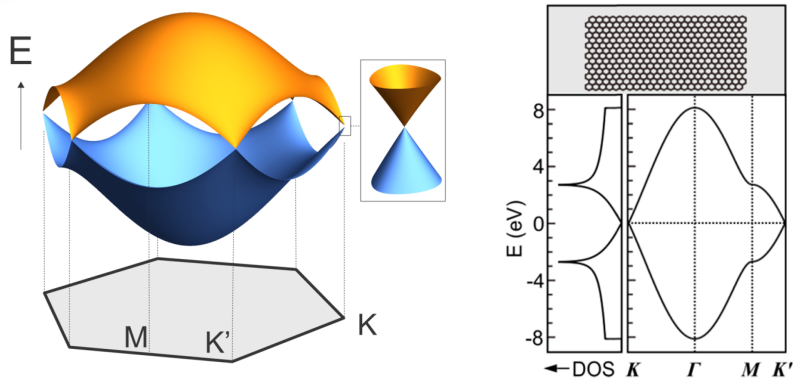


Figure 1: The band structure of monolayer graphene. The Brillouin zone is a hexagon (grey, bottom left) with vertices marked K and K' . The conduction and valence bands touch at these points (magnified in inset). On the right, the density of states is shown. It is linear around $E = 0$ and has a peak (Van Hove singularity) when the Fermi level is raised to M . Adapted from Ref. [3].

1.1.1 Graphene at low densities

The low-density band structure of graphene is visible in the inset of Fig. 1. At the Dirac point, the conduction and valence bands touch, creating a conical band structure at the K and K' points. Here, the band structure can be approximated by the linear relation [1]

$$E(\mathbf{k}) = \pm \hbar v_F \cdot |\mathbf{k}|, \quad (1)$$

where the wavevector \mathbf{k} is measured relatively to K (or K') and v_F is the Fermi velocity. This band structure is remarkable in multiple respects:

- The band structure is linear. This is a striking difference with the usual quadratic relation, $E(k) = \hbar^2 k^2 / 2m$ where m is the band mass of the electrons, reminiscent of the classic Newtonian $E(p) = p^2 / 2m$, where p is momentum. In fact, graphene is the first material with a linear band structure.
- The Fermi velocity $v_F \approx 1 \cdot 10^6$ m/s $\approx c/300$, where c is the speed of light in vacuum. It can be considered to be the speed at which

electrons travel, and it is a fraction of the speed of light. It does not depend on the Fermi energy.

- The linear band structure and the large Fermi velocity make the electrons analogous to the ultra-relativistic particles described by the Dirac equation [1], as opposed to the usual parabolic Schrödinger equation. This has led to several relativistic effects being observed in graphene, such as Klein tunnelling [4]. The non-trivial Berry phase (section 1.2.12) of graphene also stems from its linear band structure.
- The effective mass m in graphene is very small and depends on the Fermi energy: $m = \frac{E_F}{v_F^2} = \frac{k_F}{v_F}$. This corresponds to $0.03m_0$ at a moderate density of $15 \cdot 10^{11} \text{cm}^{-2}$, where m_0 is the free electron mass.

The Fermi surface at low density consists of two small pockets around the K and K' points, visible in Fig. 2.

1.1.2 Graphene at high densities

This section concentrates on graphene at the VHS, visible in Fig. 1 as the divergence in DOS near $E \approx 2.7$ eV.

When the Fermi level is raised, away from the Dirac points, the Fermi surfaces around K and K' undergo trigonal warping, visible in Fig. 3. Eventually, the pockets are stretched to touch each other at the M points, indicated in violet. At this point, the VHS has been reached. The Fermi surface is now one hole-like large pocket around Γ , instead of electron-like pockets around K and K' . The change in carrier type originating from a change in Fermi surface topology is called a Lifshitz transition [2].

The VHS in graphene is a saddle point. This creates a divergence in DOS, and a divergence in effective mass. When moving the Fermi level up to the VHS, the carrier mass evolves from massless around the Dirac point to a very large, divergent mass at high doping.

Of note is the high degree of nesting possible in the hexagonal Fermi surface. A single scattering vector \mathbf{q} , shown in black in Fig. 3 connects large portions of the Fermi surface.

The combination of a divergent DOS, divergent effective mass and near-nested Fermi surface strongly enhances the effect of electronic interactions [6]. Graphene at the VHS has been the topic of several theoretical

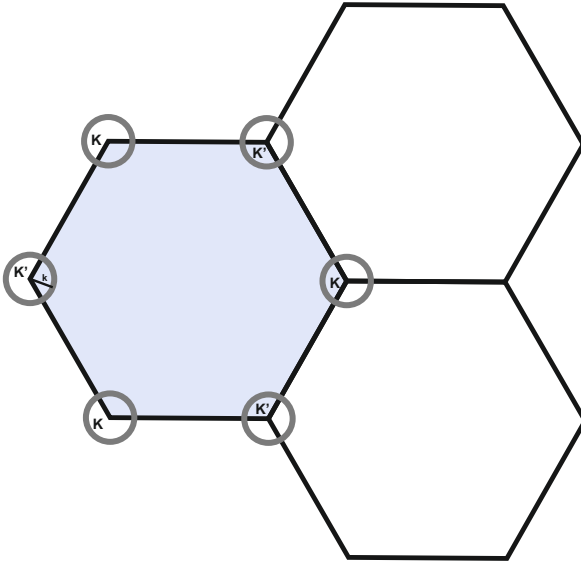


Figure 2: The Fermi surface of graphene at low carrier densities. Two pockets around K and K' are shown in grey. The wavevector \mathbf{k} is indicated in one of the pockets. The first Brillouin zone is shaded in purple.

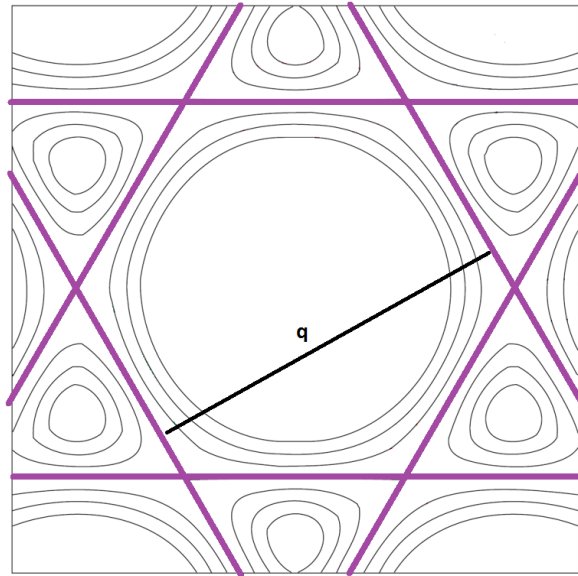


Figure 3: Contour plot of the constant energy surfaces around the VHS in graphene. The regular hexagonal Fermi surface at the VHS is marked in violet. A nesting vector \mathbf{q} is indicated in black. Modified from Ref. [5].

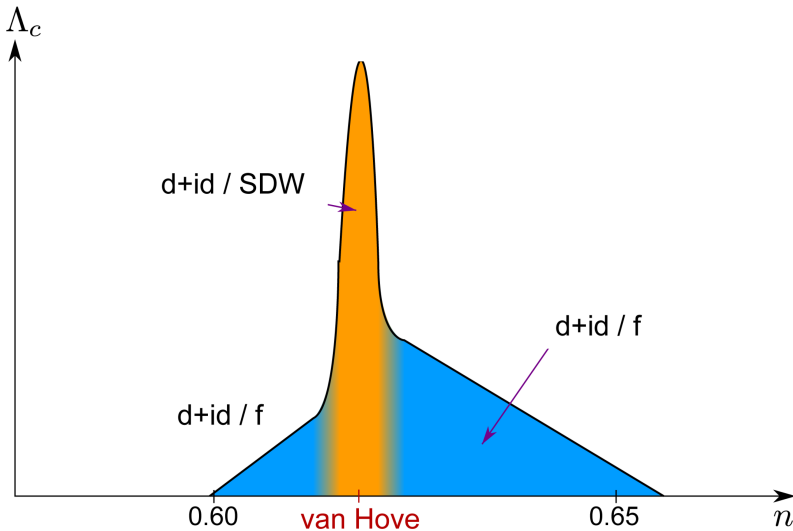


Figure 4: Predicted phase diagram of graphene at the VHS, showing the dominant instabilities at different carrier densities. $d+id$ and f signify the superconducting order parameter; SDW a spin density wave. Modified from Ref. [11].

studies. Predictions include spin-density waves [7], d -wave superconductivity [8], spontaneous quantum Hall states [9], $d+id$ -wave superconductivity [5, 10, 11] or a Chern insulator [10].

“However, clearly graphene at the M point cannot be simultaneously superconducting, metallic and insulating.” [5] Studies based on renormalization flow, which treat all potential instabilities on equal footing, seem to converge to the same phase diagram [12], shown in Fig. 4.

In these calculations, the dominant instability is a $d+id$ chiral superconductor, competing with a spin-density wave. Away from the VHS, the dominant instabilities are the $d+id$ and f -wave superconductors.

1.2 Electronic transport in a magnetic field

In this section we will derive equations that describe how electrons behave in two-dimensional systems subjected to a perpendicular magnetic field. These will be the basic quantities we measure in graphene, such as the

Hall effect, Shubnikov-de Haas oscillations and the quantum Hall effect.

First, we will derive the classical Drude model in section 1.2.1, applicable at high temperatures and small magnetic fields. At low temperatures and high magnetic field, this approach is no longer valid. The quantum mechanical treatment is presented in the next sections, 1.2.3 to 1.2.13.

1.2.1 Classical Hall effect

The behaviour of electrons in small magnetic fields can be described by the Drude model. In a two-dimensional conductor in the xy -plane, the motion of electrons is influenced by an electric field \mathbf{E} and a magnetic field \mathbf{B} . The scattering of electrons in the sample is modelled as a friction-like effect that limits the electrons' velocity. All scattering processes are described by a single scattering lifetime τ . Writing out Newton's law $\mathbf{F} = \frac{d\mathbf{p}}{dt}$, which states the sum of all forces \mathbf{F} is the change in momentum $\mathbf{p} = m\mathbf{v}$, then yields

$$m \frac{d\mathbf{v}}{dt} = -\frac{m\mathbf{v}}{\tau} - e\mathbf{E} - e\mathbf{v} \times \mathbf{B}. \quad (2)$$

The electron with charge $-e$ and velocity \mathbf{v} is deflected by the Lorentz force $-e\mathbf{v} \times \mathbf{B}$. The electron mass m is the effective band mass of electrons in the material.

In steady-state ($\frac{d\mathbf{v}}{dt} = 0$) and assuming the magnetic field is perpendicular to the sample ($\mathbf{B} = B\mathbf{e}_z$), Eq. 2 can be written out as

$$\begin{pmatrix} E_x \\ E_y \end{pmatrix} = \begin{pmatrix} \frac{-m}{e\tau} & -B \\ B & \frac{-m}{e\tau} \end{pmatrix} \begin{pmatrix} v_x \\ v_y \end{pmatrix}, \quad (3)$$

or as a function of the current density $\mathbf{j} = -nev$:

$$\begin{pmatrix} E_x \\ E_y \end{pmatrix} = \begin{pmatrix} \frac{m}{n\tau e^2} & \frac{B}{ne} \\ \frac{-B}{ne} & \frac{m}{n\tau e^2} \end{pmatrix} \begin{pmatrix} j_x \\ j_y \end{pmatrix} = \begin{pmatrix} \rho_{xx} & \rho_{xy} \\ \rho_{yx} & \rho_{yy} \end{pmatrix} \begin{pmatrix} j_x \\ j_y \end{pmatrix}. \quad (4)$$

A few remarks on Eq. 4:

- As expected from an isotropic system, $\rho_{xx} = \rho_{yy}$ and $\rho_{xy} = -\rho_{yx}$.
- The longitudinal resistivity ρ_{xx} is independent of the magnetic field.

- The magnetic field creates an electric field perpendicular to the direction of the current: the Hall electric field. It increases linearly with magnetic field strength and current density:

$$E_y = \frac{-B}{ne} \cdot j_x. \quad (5)$$

This electric field will counteract the deflection of the electrons by the magnetic field.

- Therefore, the carrier density n can be determined from a measurement of the Hall effect. The sign of the Hall signal will be different for electron or hole carriers.
- The scattering time τ or the mobility $\mu = \frac{e\tau}{m}$ can then be extracted from $\rho_{xx} = 1/\mu en$ or from the identity $\mu B = \frac{\rho_{xy}}{\rho_{xx}}$.

A typical sample geometry for Hall measurements is shown in Fig. 5. The current is confined in a well-defined region. The electric fields and current densities in Eq. 4 can now be related to observable voltages and currents:

$$\begin{aligned} V_{xx} &= E_x \cdot L & V_H &= E_y \cdot W \\ I_x &= j_x \cdot W & j_y &= 0. \end{aligned} \quad (6)$$

The resulting resistances and resistivities are:

$$R_{xx} = \frac{V_{xx}}{I_x} = \frac{E_x}{j_x} \cdot \frac{L}{W} = \rho_{xx} \cdot \frac{L}{W}, \quad (7)$$

$$R_{xy} = \frac{V_H}{I_x} = \frac{E_y}{j_x} = \rho_{yx} \quad (8)$$

Measuring the Hall *resistance* is the same as measuring transversal *resistivity*. This quantity does not depend on sample geometry. A method of measuring these quantities using ac excitations is described in Appendix B.

This classical treatment of the Hall effect is no longer valid in the regime of strong magnetic fields and low temperatures. The quantum mechanical treatment is described in the following sections.

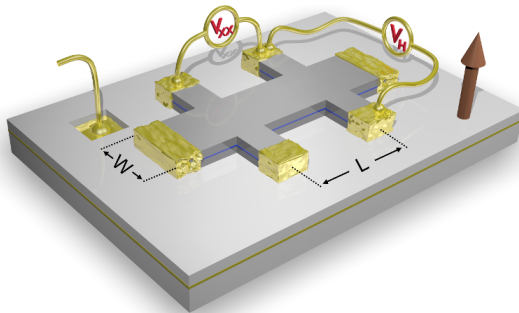


Figure 5: The Hall bar, a common geometry to characterize two-dimensional samples. Current flows between the two contacts spanning the entire width of the Hall bar. Longitudinal (V_{xx}) and transversal (V_H) voltages are measured. The magnetic field (brown arrow) is perpendicular to the sample. From [13].

1.2.2 Electrons in two dimensions

In this section, we will see why electrons, confined in a narrow well, can be considered to be two-dimensional. This treatment naturally applies to graphene, where the electrons are confined to one atomic layer. The realization of a layer of graphene will be discussed in section 2.1.

An electron is contained in an infinite one-dimensional potential well with width d and is free to move in the xy -plane: $V(z) = 0$ when $0 < z < d$, and $V(z) = \infty$ otherwise. The well-known solutions are displayed in Fig. 6. Their energies are given by

$$E = E_z + \frac{\hbar^2 k_x^2}{2m} + \frac{\hbar^2 k_y^2}{2m}. \quad (9)$$

Since the electron is still free to move in the xy -plane, the wavevectors k_x and k_y can take on any value. If we solve the Schrödinger equation for this system, we will see the confinement in the z -direction will quantize $k_z = i\pi/d$ with $i = 1, 2, 3, \dots$:

$$E_z = \frac{\hbar^2 k_i^2}{2m} = \frac{\hbar^2 \pi^2 i^2}{2md^2}. \quad (10)$$

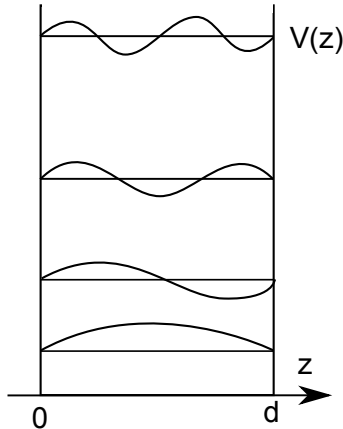


Figure 6: Solutions to the one-dimensional infinite well, an electron in a box.

The narrower the potential well, the broader the spacing between the energy levels will be. In a physical system, we can make sure all electrons will have the lowest k_z , so that only the lowest subband ($i = 1$) is occupied. Even though the physical quantum well has a finite thickness, the electrons will then behave as in a purely two-dimensional conductor.

1.2.3 Quantization in strong magnetic fields

A correct description of behaviour of electrons in a strong magnetic field requires a purely quantum mechanical description of the system. The following treatment is based on [14] and [15]. The task at hand is to calculate the wave functions and energy spectrum of a particle in a magnetic field, described by the Hamiltonian

$$H = \frac{1}{2m} (\mathbf{p} + e\mathbf{A})^2. \quad (11)$$

Here we assume a parabolic dispersion, as we consider free particles. This treatment trivially extends to materials with a parabolic dispersion, such as GaAs. The more difficult case of graphene, with its linear band structure (Eq. 1), will be explained later, in section 1.2.12. We

assume the particle is restricted to the xy -plane and the magnetic field is perpendicular to this plane: $\mathbf{B} = B\mathbf{e}_z = \nabla \times \mathbf{A}$.

The vector potential \mathbf{A} is not uniquely defined by this relation. The choice of gauge will not change the end result, but might make the calculation easier. In this section, we choose the *Landau gauge* $\mathbf{A} = xB\mathbf{e}_y$.

We write down the Schrödinger equation

$$-\frac{\hbar^2}{2m} \frac{\partial^2}{\partial x^2} \psi + \frac{1}{2m} \left(-i\hbar \frac{\partial}{\partial y} + eBx \right)^2 \psi = E\psi \quad (12)$$

$$\frac{\partial^2}{\partial x^2} \psi + \left(\frac{\partial}{\partial y} + \frac{ieBx}{\hbar} \right)^2 \psi = -\frac{2mE}{\hbar^2} \psi. \quad (13)$$

This equation is translationally invariant in the y -direction, so our Ansatz can contain plane waves in this direction. This is not true for x (consider Eq. 13 at $x = 0$). Hence:

$$\psi = e^{-ik_y y} \cdot f(x). \quad (14)$$

After some straightforward algebra, Eq. 13 becomes

$$\frac{d^2 f}{dx^2} + \left[\frac{2mE}{\hbar^2} - \left(\frac{eBx}{\hbar} - k_y \right)^2 \right] f = 0, \quad (15)$$

and after substituting

$$x' = x - \frac{\hbar k_y}{eB},$$

$$\omega_c = \frac{eB}{m},$$

we can write it as

$$\frac{d^2 f}{dx'^2} + \frac{2m}{\hbar^2} \left[E - \frac{1}{2} m \omega_c^2 x'^2 \right] f = 0. \quad (16)$$

Eq. 16 describes a one-dimensional harmonic oscillator, so we can simply write down the energy of the system

$$E = E_l = \hbar\omega_c \left(l + \frac{1}{2} \right) \quad (17)$$

with quantum numbers $l = 0, 1, 2, \dots$. The eigenfunctions are

$$\psi_{l, k_y} = A e^{-ik_y y} \cdot H_l(x - k_y l_B^2) \cdot e^{-(x - k_y l_B^2)^2 / 2l_B^2} \quad (18)$$

with some normalization factor A and H_l the Hermite polynomials for a harmonic oscillator.

Considering these wave functions, we note that:

- The oscillator frequency is $\omega_c = eB/m$, the cyclotron frequency.
- The particle oscillates around a central coordinate $x' = x - k_y l_B^2$ where we introduced the magnetic length $l_B = \sqrt{\hbar/eB}$, the length scale for particles in a magnetic field. At 1 Tesla, it equals 25.7 nm.
- The *momentum* in the y -direction now takes the role of *position* in the x -direction.
- The system is described by two quantum numbers: the wavevector k_y and the quantum number l for a harmonic oscillator.
- The particle is free in the y -direction, but is exponentially confined in x by the length scale l_B .
- All particles in a magnetic field now reside in *Landau levels*, a highly degenerate state with energy E_l .

1.2.4 Degeneracy

We can count the degeneracy of these wavefunctions in a two-dimensional system. We restrict the particle to a box with dimensions L_x and L_y .

The y -direction is translationally invariant (see the discussion of Eq. 13), so having a finite size L_y is the same as putting the particle in a box in this direction. k_y is therefore quantized in units of $2\pi/L_y$.

We know the wavefunctions are localized around $x = k_y l_B^2$. The sample is restricted to $0 \leq x \leq L_x$, so informally, we can restrict k_y to $0 \leq k_y \leq L_x/l_B^2$.

The total degeneracy is therefore

$$\mathcal{N} = \frac{L_y}{2\pi} \cdot \frac{L_x}{l_B^2} = \frac{A}{2\pi l_B^2} = \frac{eBA}{h} = \frac{\Phi}{\Phi_0}, \quad (19)$$

where we have used the area of the sample $A = L_x L_y$ and the flux quantum $\Phi_0 = h/e$. This result confirms the picture that one particle occupies a real-space area of $l_B^2 = h/eB$.

Note that the degeneracy of one Landau level is very large, and grows with increasing magnetic field. After all, the magnetic length l_B shrinks as the field increases, allowing more particles to fit in the same level.

The degeneracy of a Landau level can also be determined by considering the conservation of the number of states. Without a magnetic field, the states are equally spaced in reciprocal space (Fig. 7a) and the density of states is constant ($\text{DOS} = \frac{m}{\pi\hbar^2}$).

In a large magnetic field, all states condense into Landau levels (Fig. 7b). The DOS now consists of widely separated ($\hbar\omega_c$) and highly degenerate (degeneracy factor \mathcal{N}) peaks.

Since the number of electrons does not change when a magnetic field is applied, the number of electrons in a single filled Landau level ($2\mathcal{N}$) equals the number of electrons within a range of $\pm \frac{\hbar\omega_c}{2}$.

$$2\mathcal{N} = A \cdot \text{DOS} \cdot \hbar\omega_c \quad (20)$$

$$\mathcal{N} = \frac{A}{2} \cdot \frac{m}{\pi\hbar^2} \cdot \hbar \frac{eB}{m} \quad (21)$$

$$\mathcal{N} = \frac{eBA}{h} \quad (22)$$

$$\mathcal{N} = \frac{\Phi}{\Phi_0} \quad (23)$$

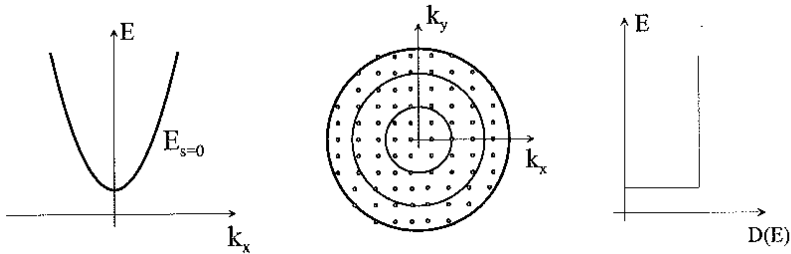
where the flux through the sample $\Phi = B \cdot A$, the flux quantum $\Phi_0 = h/e$ and the cyclotron frequency $\omega_c = eB/m$ were used as before. This is the same result as Eq. 19.

1.2.5 Symmetric gauge

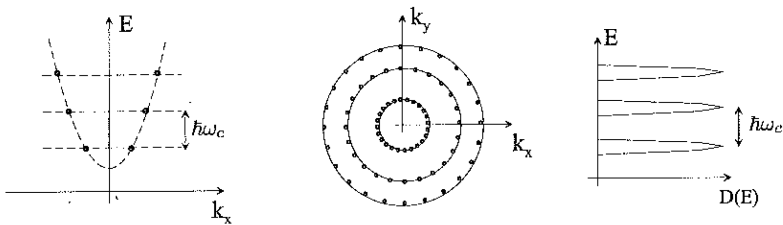
We can rederive the Landau level spectrum for the symmetric gauge:

$$\mathbf{A} = -\frac{1}{2}\mathbf{B} \times \mathbf{r} \quad (24)$$

$$\mathbf{A} = -\frac{yB}{2}\mathbf{e}_x + \frac{xB}{2}\mathbf{e}_y. \quad (25)$$



(a) Without a magnetic field, the two-dimensional electrons in the lowest sub-band (left panel) are spaced equally throughout k -space (middle panel). If the dispersion is quadratic, the density of states (right panel) is a constant.



(b) When a magnetic field is applied, Landau levels form (separated by $\hbar\omega_c$). In k -space, all states fall on concentric circles. The DOS is now divided in discrete and highly degenerate Landau levels.

Figure 7: Landau levels and DOS (denoted as $D(E)$) at zero magnetic field and large magnetic field.

This gauge is not translationally invariant in both x - and y -directions. It is rotationally symmetric. As a result, the angular momentum is a well-defined quantity in this gauge.

The complete derivation can be found in [14] and [15]. The results are presented below. Observables such as energies and degeneracy of a Landau level are identical. Gauge-dependent quantities such as the wavefunctions are not.

The wavefunctions are determined by the radial quantum number n and the angular momentum m . Because of their rotational symmetry, they are best expressed in cylindrical coordinates:

$$\psi_{n,m}(r, \theta) = A \cdot \left(\frac{r^2}{2l_B^2} \right)^{|m|/2} \cdot e^{-\frac{r^2}{4l_B^2}} \cdot L_n^{|m|} \left(\frac{r^2}{2l_B^2} \right) \cdot e^{im\theta}. \quad (26)$$

A is here an appropriate normalization factor and $L_n^{|m|}$ the associated Laguerre polynomial. The first few wavefunctions are sketched in Fig. 8. The radial quantum number $n = 0, 1, 2, \dots$ counts the number of nodes in the wavefunction and determines the energy of the particle $E_n = \hbar\omega_c(n + 1/2)$. The angular momentum m (in units of \hbar) pushes the function away from the origin. The probability to find the particle at the origin is only nonzero if $m \neq 0$. Particles circle around the origin with a larger radius and therefore higher angular momentum as m increases.

The maximal probability amplitude of the wavefunctions described in Eq. 26 is at $r = \sqrt{2m}l_B$. We can again estimate the number of allowed states in a single Landau level. Limit the sample now to a disk with area $A = \pi R^2$. The number of allowed states is then

$$R = \sqrt{2\mathcal{N}} \cdot l_B, \quad (27)$$

$$\mathcal{N} = \frac{R^2}{2l_B^2} = \frac{eBA}{h} = \frac{\Phi}{\Phi_0}. \quad (28)$$

This is the same result as before, Eq. 19.

1.2.6 The role of spin

So far we have neglected the spin degree of freedom. Every particle can be spin-up or spin-down, meaning the Landau level degeneracy of Eq. (19) is missing a factor of two.

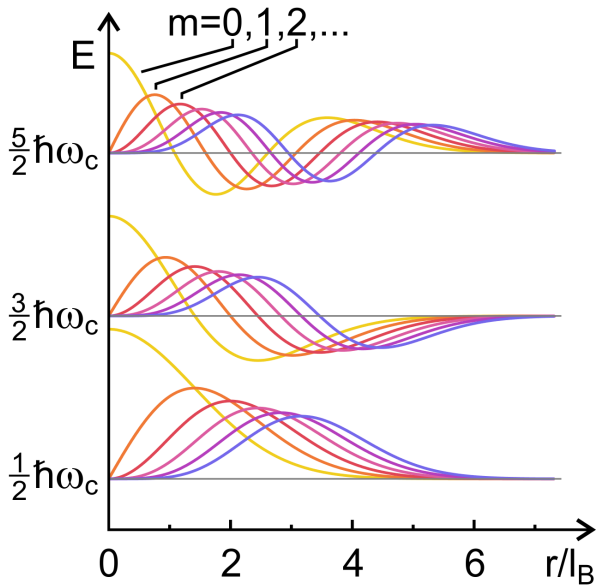


Figure 8: The wavefunctions in the symmetric gauge, plotted against distance from the origin for the first few n and m . From [13].

Spins and the magnetic field interact via the *Zeeman effect*. The energy difference between particles with opposite spin orientation is

$$E_z = g\mu_B B, \quad (29)$$

the Zeeman energy with the Bohr magneton $\mu_B = e\hbar/2m$ and g the g -factor of the material. This effect splits every Landau level in a spin-up and spin-down branch, each with degeneracy \mathcal{N} .

We can now calculate the number of occupied branches in a sample with N carriers, which we define as the *filling factor* ν

$$\nu = \frac{N}{\mathcal{N}} = \frac{hN}{eBA} = \frac{hn}{eB} \quad (30)$$

with carrier density n . It is customary to count both branches of a Landau level. Hence, $\nu = 1$ corresponds to a fully occupied spin-up branch of the lowest Landau level, with the spin-down branch empty. For $\nu = 2$, the entire lowest Landau level is filled, and the electron system is unpolarized.

1.2.7 Landau levels in an electric field

Finally we include an electric field to this model in order to make predictions about observables such as voltages and currents. It is implemented by adding the electric field potential $\phi = -eEx$ to the Hamiltonian. To solve this problem, we use the Landau gauge.

$$H = \frac{1}{2m}(\mathbf{p} + e\mathbf{A})^2 - \phi \quad (31)$$

$$= \frac{1}{2m}(p_x^2 + (p_y + eBx)^2) - eEx \quad (32)$$

Our Ansatz (Eq. 14) is still valid. If we complete the square in Eq. 32, we can write it as a displaced harmonic oscillator (Eq. (10.7.12) in [15]). The displacement of the guiding center becomes

$$x' = x - k_y l_B^2 - \frac{mE}{eB^2}. \quad (33)$$

In this case, the energy of the particle depends on electric field and the large degeneracy of the $E = 0$ case above is lifted.

$$E_{l,k_y,k_z} = \hbar\omega_c \left(l + \frac{1}{2} \right) - eE \left(k_y l_B^2 + \frac{mE}{eB^2} \right) + \frac{m}{2} \frac{E^2}{B^2} \quad (34)$$

These eigenvalues vary with momentum k_y , which means there is drift in this direction. The group velocity

$$v_y = \frac{1}{\hbar} \frac{\partial E_{l,k_y,k_z}}{\partial k_y} = -\frac{eEl_B^2}{\hbar} = -\frac{E}{B} \quad (35)$$

nicely reproduces the classical physics. The electric field E_x is applied perpendicular to the magnetic field B_z , resulting in a drift velocity v_y in the $\mathbf{E} \times \mathbf{B}$ -direction.

1.2.8 Quantum Hall resistance

The group velocity calculated above is different from the velocity of a single particle. We can calculate it from

$$m\dot{\mathbf{x}} = \mathbf{p} + e\mathbf{A}. \quad (36)$$

Current $\mathbf{I} = -e\dot{\mathbf{x}}$ is then the expectation value of the velocity of all N electrons in the system.

$$\mathbf{I} = -e \sum_{\text{filled states}} \langle \psi | \dot{\mathbf{x}} | \psi \rangle \quad (37)$$

$$= -\frac{e}{m} \sum_{\text{filled states}} \langle \psi | -i\hbar\nabla + e\mathbf{A} | \psi \rangle \quad (38)$$

Once again we use the Landau gauge $\mathbf{A} = xB\mathbf{e}_y$. We assume that ν Landau levels are fully occupied and calculate I_x and I_y .

$$I_x = -\frac{e}{m} \sum_{n=1}^{\nu} \sum_k \langle \psi_{n,k} | -i\hbar \frac{\partial}{\partial x} | \psi_{n,k} \rangle = 0 \quad (39)$$

This equals zero because the momentum expectation values of all eigenstates of a harmonic oscillator are zero.

$$I_y = -\frac{e}{m} \sum_{n=1}^{\nu} \sum_k \langle \psi_{n,k} | -i\hbar \frac{\partial}{\partial y} + eBx | \psi_{n,k} \rangle \quad (40)$$

$$= -\frac{e}{m} \sum_{n=1}^{\nu} \sum_k \langle \psi_{n,k} | \hbar k_y + eBx | \psi_{n,k} \rangle \quad (41)$$

We know from equation 33 the position expectation value $\langle x \rangle$ is shifted from the origin:

$$\langle \psi | x | \psi \rangle = -k_y l_B^2 - \frac{mE}{eB^2}. \quad (42)$$

The first term $-k_y l_B^2$ cancels the term $\langle \phi | \hbar k_y | \psi \rangle$ in Eq. 41, so that finally

$$I_y = -e \sum_{n=1}^{\nu} \sum_k \frac{E}{B}. \quad (43)$$

Note in the case $E = 0$ all terms in (41) would have cancelled and $I_y = 0$.

We assume that all Landau levels contribute equally. One Landau level contains \mathcal{N} states (Eq. 19).

$$I_y = e\nu \frac{\Phi}{\Phi_0} \frac{E}{B} \quad (44)$$

$$J_y = \frac{I_y}{A} = \nu \frac{e^2}{h} \cdot E \quad (45)$$

We can now write down the resistivity matrix (Eq. 4).

$$\mathbf{E} = \rho \cdot \mathbf{J} \quad (46)$$

$$\begin{pmatrix} E_x \\ E_y \end{pmatrix} = \begin{pmatrix} \rho_{xx} & \rho_{xy} \\ \rho_{yx} & \rho_{yy} \end{pmatrix} \cdot \begin{pmatrix} j_x \\ j_y \end{pmatrix} \quad (47)$$

$$\begin{pmatrix} E \\ 0 \end{pmatrix} = \begin{pmatrix} 0 & \frac{h}{\nu e^2} \\ -\frac{h}{\nu e^2} & 0 \end{pmatrix} \cdot \begin{pmatrix} 0 \\ \nu \frac{e^2}{h} E \end{pmatrix} \quad (48)$$

At long last we have calculated the *quantum Hall resistance*:

$$\rho_{xx} = 0 \text{ and } \rho_{xy} = h/\nu e^2. \quad (49)$$

The transversal resistivity ρ_{xy} only depends on the fundamental constants e and h , regardless of the sample material or dimensions [16]. This remarkable fact lies at the base of the decision in 2019 to make the quantum Hall effect one of the cornerstones of the new SI, based on fundamental constants of nature [17].

It is possible to invert the matrix (47) to write down the longitudinal and transversal *conductivity*:

$$\sigma_{xx} = \frac{\rho_{xx}}{\rho_{xx}^2 + \rho_{xy}^2} = 0, \quad (50)$$

$$\sigma_{xy} = \frac{\rho_{xy}}{\rho_{xx}^2 + \rho_{xy}^2} = \nu \frac{e^2}{h}. \quad (51)$$

These results are valid if the filling factor takes on an integer value. However, we can see in experiments (Fig. 9) that the Hall resistance is still quantized away from integer filling factor. To understand this, we need to look into the role of disorder and the edges of the sample.

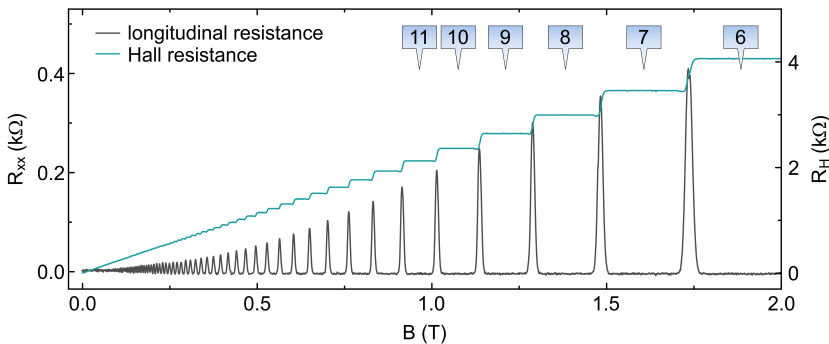


Figure 9: Longitudinal resistance R_{xx} and Hall resistance $R_{xy} = R_H$ of a GaAs/AlGaAs quantum well. The sample is cooled down to 20 mK and subjected to a perpendicular magnetic field. Several quantum Hall plateaus, the regions with quantized R_H and zero R_{xx} , are visible. The blue labels indicate the locations of corresponding integer filling factors. From Ref. [13].

1.2.9 Disorder in the quantum Hall effect

The emergence of Landau levels in the previous section is valid for free particles. Electrons in a crystal can be modelled to behave like free electrons by working with the effective mass ($m_e \rightarrow m^*$), if they obey a parabolic dispersion. In reality, some disorder is always present because of impurities or ionized donor atoms.

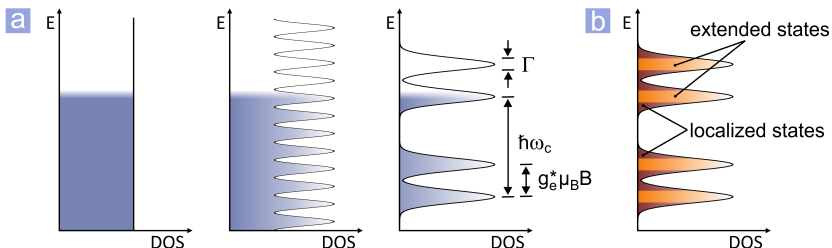


Figure 10: (a) Landau levels in real samples are no longer infinitely sharp, but evolve gradually from the continuous density of states at zero field to peaks at high perpendicular field. (b) They are separated in extended and localized states, which behave differently in transport. From [13].

Random disorder adds a perturbation $V(\mathbf{r})$ to the Hamiltonian in Eq. 11. As long as the perturbation is small ($|V(\mathbf{r})| \ll \hbar\omega_c$), the calculations above are still valid. The large degeneracy (Eq. 19) is now lifted, and Landau levels are no longer sharp δ -like peaks, but have a certain width in energy Γ , as shown in Fig. 10.

Ideally, wavefunctions extend indefinitely over the entire sample (e.g. Eq. 18). In a disordered sample this is no longer the case. Electrons can be localized by disorder and be contained in a small area of constant potential, sketched in Fig. 11.

This distinction between localized and extended wavefunctions can explain why the longitudinal conductance σ_{xx} is zero not only at integer filling factors, but also at values around it.

When a band is fully filled, all electrons are localized and no charge can flow through the system: $\sigma_{xx} = \rho_{xx} = 0$. Increasing the number of electrons will only occupy localized states, which does not change the conductivity. Only when extended states become filled, can charge move along the system and can we measure a nonzero conductivity. Note that disorder stabilizes the quantum Hall effect: with no disorder, any additional electron would occupy an extended state in the next Landau level.

Therefore, the zero longitudinal resistance can be seen at a range of filling factors around an integer. The reason for the exact quantization of transversal resistance will appear in the next section, when we look at the role of edges.

Experimentally, the longitudinal resistance is never exactly zero, but

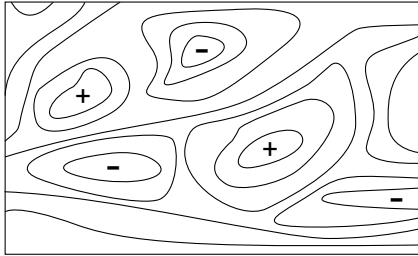


Figure 11: Disorder localizes electrons. Most electrons are confined to equipotentials around hills (+) or troughs (-) in the disorder potential. Only if the Fermi level is in the middle of the Landau level, a few states can extend over the entire sample.

is *vanishingly small*. It exhibits thermally activated behaviour,

$$R_{xx} \propto e^{-\frac{\Delta_\nu}{2k_B T}}. \quad (52)$$

An Arrhenius plot of $\log(R_{xx})$ versus $1/T$ allows for the extraction of Δ_ν , the energy gap of the quantum Hall state. Reducing the electron temperature makes the longitudinal resistance arbitrarily small.

Naively, the condition $\sigma_{xx} = \rho_{xx} = 0$ appears to contradict itself. It is indeed impossible when considering Ohmic resistors. Only with the absence of dissipation can this condition be met. Carriers injected at the source stay at the source potential along the length of the Hall bar. Only at the drain contact is energy dissipated in a so-called “hot spot”. This very localized heating has even been observed experimentally.

1.2.10 Edges of the sample

When moving towards the edge of a two-dimensional system, the Landau levels bend upwards because of the pinning of the Fermi energy in the semiconductor band gap. Consequently, the electron density and filling factor drop to zero. In a modern graphene stack, the edge is quite narrow, on the order of 100 nm [18].

The bending of the Landau levels is sketched in Fig. 12. At some point all Landau levels will cross the Fermi energy, creating one-dimensional channels with electronic states at the Fermi surface. These lines are normally characterized as Landauer-Büttiker edge channels which carry

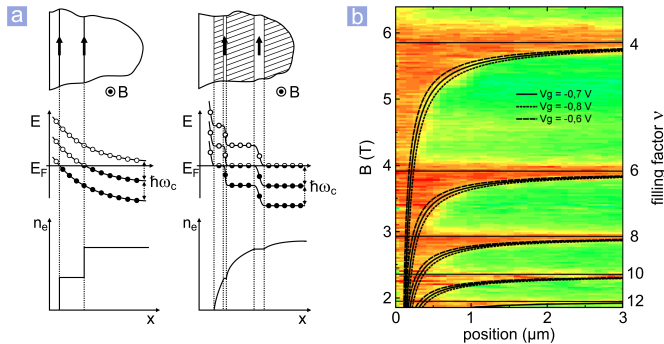


Figure 12: Influence of the sample edges on the quantum Hall effect. (a, left) Landauer-Büttiker picture of band bending. The current is carried in one-dimensional stripes, carrier density n is discontinuous. This is unrealistic. (a, right) Compressible and incompressible stripes form according to the self-consistent calculations of Chklovskii et al. [19]. The Landau levels arrange themselves in compressible or incompressible regions where Landau levels are partly or completely occupied. Carrier density now smoothly decreases to zero when approaching the edge. Diamagnetic (equilibration) currents flow in the regions of incompressible stripes where Landau levels are tilted. (b) Scan of the Hall potential at multiple filling factors near the edge of a Hall bar [20]. The voltage drops (from red to green) at the location the current flows, indicating the innermost compressible stripe (black lines). This stripe moves away from the edge when approaching a full Landau level.

the external current. When calculating the electron density in this region (Fig. 12, bottom left), discontinuities will appear. This is unphysical when electrons interact with each other via Coulomb forces. Furthermore, the current density in these one-dimensional channels has to be infinite.

Adding Coulomb interactions to this picture, the bending of the Landau levels must be calculated self-consistently [19]. The model shown in Fig. 12a, right emerges. The carrier density now decreases smoothly when approaching the edge. The electron gas is divided in alternating strips of *compressible* and *incompressible* states.

Compressible stripes are the region where a Landau level meets the Fermi energy. These stripes with electronic states at the Fermi energy

are able to adopt a well-defined electrochemical potential. They have a certain width in which the carrier density changes.

In the incompressible stripes, the Fermi level is between Landau levels. This is the region in which the carrier density is constant and characterized by an integer filling factor.

The Landau levels are bent, which means there is an electric field in the x -direction. With the strong magnetic field perpendicular to the plane, the electrons in the incompressible stripe drift in the y -direction. In many sketches these persistent, dissipationless currents are visualized as skipping orbits. Additional potential drops across incompressible stripes due to finite Hall voltage increase or decrease these equilibration currents.

All current in the quantum Hall state will therefore flow in the incompressible stripes. Calculations show [19] the incompressible stripes are always more narrow than the compressible regions, and they are wider and more stable far away from the edge.

This microscopic picture was confirmed by scanning probe experiments (Fig. 12b) [21] [20]. The local Hall potential was measured at different filling factors. The innermost compressible stripe carries all the current and moves inward with decreasing filling factor. At precisely integer filling, the entire bulk is incompressible, and the current will flow through the bulk of the sample.

The voltage drop across a stripe is proportional to the current flowing inside. Only the innermost stripe carries current and accounts for the complete voltage drop. The filling factor of this stripe is always the highest of the entire sample, consequently this filling factor quantizes the measured resistivity (Eq. 49): $\rho_{xy} = h/\nu e^2$.

1.2.11 Shubnikov-de Haas oscillations

The density of states of a material in a magnetic field is already modified before Landau quantization occurs. As Fig. 10 shows, wiggles in the density of states emerge at intermediate fields. Variations of the density of states are visible in many different experiments. This section will focus on the resulting oscillations of resistance, Shubnikov-de Haas oscillations.

Consider moving the chemical potential in the second panel of Fig. 10. If the Fermi level lies at one of the peaks in the density of states, there are many states available to scatter into, and the resistivity is high. Moving the Fermi level to a minimum reduces the scattering and lowers resistivity.

The same oscillating behaviour will occur when the magnetic field is increased and the peaks' spacing increases. The locations of the oscillations' minima allow us to calculate the carrier density very accurately: exactly one Landau level (containing \mathcal{N} electrons) is filled or emptied when moving to the next minimum.

At the i -th minimum, i Landau levels are filled. The total number of electrons N is then

$$N = 2i \frac{\Phi}{\Phi_0} = 2i \frac{eB_i A}{h}. \quad (53)$$

At the $i + 1$ -th minimum, the number of electrons is still the same

$$N = (i + 1) \frac{eB_{i+1} A}{h}, \quad (54)$$

so that

$$\frac{1}{B_{i+1}} - \frac{1}{B_i} = \Delta \left(\frac{1}{B} \right) = \frac{2e}{nh}, \quad (55)$$

where $n = N/A$ is the carrier density, the number of carriers per unit area.

1.2.12 Quantum Hall effect in graphene

The linear dispersion of graphene, $E(k) = \hbar v_f k$, near the Dirac points (Fig. 13) modifies the derivation above. The Hamiltonian for graphene in a magnetic field is now

$$H = v_f \mathbf{p} + e\mathbf{A}, \quad (56)$$

different from the Hamiltonian in Eq. (11) which was valid for quadratic dispersions such as in GaAs. The full derivation of electronic properties is performed in [1], we will simply state the results.

The Landau levels are no longer equidistant (Fig. 14, right):

$$E_l = \pm \sqrt{2\hbar v_f^2 e B l} \text{ with } l = 0, 1, 2, \dots \quad (57)$$

The density of states of graphene depends on energy (Fig. 14), as opposed to the constant density of materials with a parabolic dispersion.

When considering Eq. 57, we note the following:

- The conical band structure allows both electrons and holes, depending on the location of the Fermi energy. A strong magnetic field will quantize both branches, creating Landau levels with positive and negative index (Fig. 13).
- The unit cell of graphene has two atoms, creating an extra degree of freedom for an electron in the lattice. This is why there are two Dirac cones in the Brillouin zone, at K and K' .
- Together with spin, this makes every Landau level *fourfold* degenerate.
- Quantum Hall plateaus are therefore $\frac{h}{4e^2}$ apart [22], unless spin or valley symmetry is broken.
- The zeroth Landau level ($l = 0$) is special. Its energy will always be at the Dirac point, and does not depend on magnetic field. The fourfold degeneracy of this Landau level is shared between electrons and holes. This creates an offset of 2 for other Landau levels, resulting in the typical quantum Hall sequence $\nu = \pm 2, \pm 6, \pm 10 \dots$ if the fourfold degeneracy is not yet lifted. It is the origin of many profound effects in graphene, relating to the Berry phase of π when the Fermi surface circles the Dirac points at K and K' . In the quantum Hall regime it causes a shift [23] of $\frac{1}{2}$ (the so-called Berry shift) in the filling factor:

$$\nu = 4 \cdot \left(n + \frac{1}{2} \right). \quad (58)$$

- The Berry shift can be measured directly in Shubnikov-de Haas oscillations. When considering fully spin-split Landau levels, the numbering will be shifted by $\frac{1}{2}$ [22].

1.2.13 Beyond the last Landau level

Filling factor $\nu = 1$ would be the last plateau in the model of section 1.2.7. In very high quality samples, fractional plateaus with $\nu = \frac{p}{q}$ have been observed. They originate from electron-electron interactions forming gaps in the many-particle electron system. A single-particle picture no longer can capture the physics of the fractional quantum Hall effect, and new models with novel quasiparticles have been developed. An overview of some of the astonishing features of these states is given in Ref. [24].

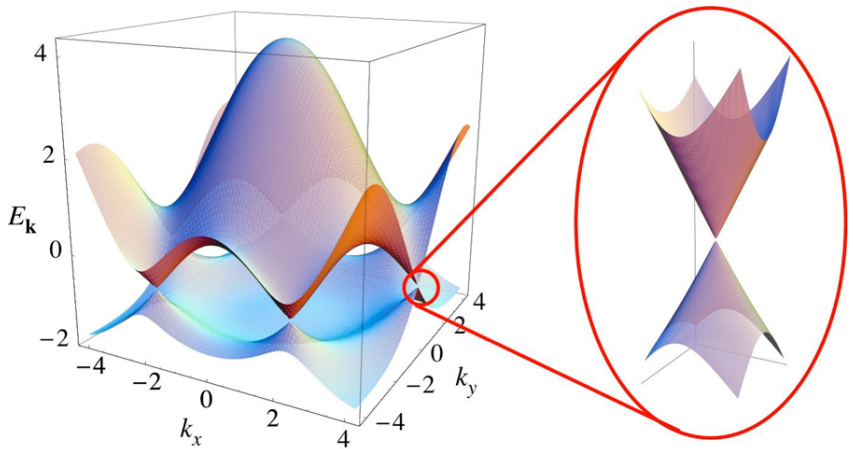


Figure 13: Band structure of graphene. The hexagonal Brillouin zone has six vertices, labeled alternatingly K and K' . The conduction and valence band touch at these points, the Dirac points, around which the bands are linear (inset). In undoped graphene, the Fermi level is exactly at this point. From [1].

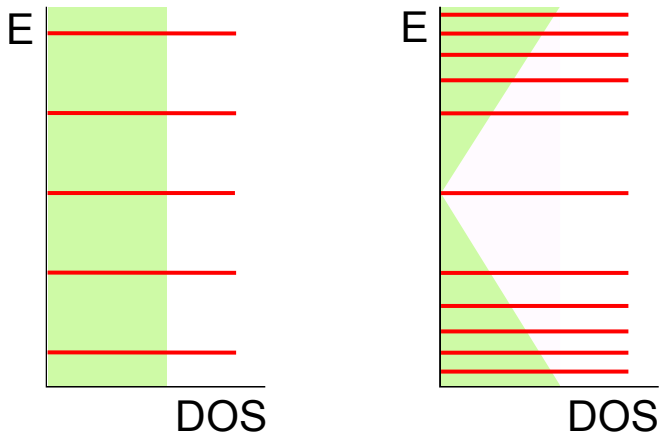


Figure 14: Effect of magnetic field on the density of states (DOS) of a two-dimensional conductor. In green, DOS for zero field; in red, for a strong perpendicular magnetic field. Left panel shows the result for the usual quadratic dispersion, on the right, for the graphene-like linear dispersion.

1.3 Electron hydrodynamics

This section describes an emergent phenomenon in very high quality electron systems, called electron hydrodynamics. After developing the notion of *viscosity*, we will determine conditions for electron hydrodynamics, and present recent experiments.

The relation between viscosity and momentum transport can be intuitively understood by comparing the similarities between the three relations that govern transport phenomena:

$$q = -\kappa \cdot \frac{\partial T}{\partial x} \quad \text{Fourier's law of heat transport,} \quad (59)$$

$$J = -D \cdot \frac{\partial C}{\partial x} \quad \text{Fick's law of diffusion,} \quad (60)$$

$$\tau = \eta \cdot \frac{\partial u}{\partial y} \quad \text{Newton's law of viscosity.} \quad (61)$$

Here, q is heat flux and J is mass flux. κ (thermal conductivity) and D (diffusion constant) are the constants that relate q and J to a temperature (T) or concentration (C) gradient. The same interpretation works for Newton's law of viscosity. The shear stress τ (in units of momentum per unit of time per area) is then considered as *momentum flux*, and is related to a velocity gradient ($\frac{\partial u}{\partial y}$) by the viscosity, η . It means momentum will flow across velocity gradients in viscous fluids, shown in Fig. 15.

The Eqs. (59) to (61) are the only ones of their kind in the study of transport phenomena. They reflect the conservation of energy (heat), mass and momentum, respectively. Only because these quantities are conserved in the microscopic interactions inside the fluid, are they conserved over macroscopic length scales and do the equations hold.

The requirement for viscous flow, global momentum conservation, is easily satisfied in common hydrodynamic fluids such as water or steam. The only scattering mechanism present in these fluids are elastic particle-particle collisions if the walls containing the fluid are far away. These will randomize an *individual* particle's momentum, but will preserve the *collective* momentum of all particles.

Global momentum conservation is a much more stringent criterion for electron liquids. The lattice in which the electrons flow is usually the strongest source of scattering. In this case, the carriers are completely thermalized with the lattice [25] and the diffusive Drude behaviour (Eq. 2) is recovered.

If we want to observe hydrodynamic effects in an electron fluid, the above considerations place a few constraints on the system [25]:

- Electron-electron scattering must be the dominant scattering mechanism. It is the only interaction that preserves momentum on a global scale. Therefore, the electron-electron interaction should be strong.
- Impurity scattering should be minimal. The momentum of an electron is changed when it scatters on a lattice impurity, destroying the conservation of global momentum. A fraction of impurity scattering events is inelastic [26] and emit or absorb a phonon, modifying both the momentum and energy of the electron.
- Similarly, electron-phonon scattering should be minimized. Inelastic scattering on a phonon does not conserve global momentum.
- A final intrinsic source of momentum is Umklapp scattering. Consider the process in Fig. 16 where particles 1 and 2 (wavevectors in blue) interact. On the left, the resulting wavevector 3 (in red) falls inside the Brillouin zone and crystal momentum is conserved ($k_1 + k_2 = k_3$). Because crystal momentum is only defined up to a reciprocal lattice vector \mathbf{G} , the process on the right is also allowed: $k_1 + k_2 = k'_3 = k_3 + \mathbf{G}$. In this case, two wavevectors that point to the left add up to a wavevector pointing to the right. A material in which momentum is conserved in the electron liquid cannot allow for Umklapp processes.

1.3.1 Demonstrations of electron hydrodynamics in graphene

Early investigations of hydrodynamic transport [27] used the two-dimensional electron system in (Al,Ga)As heterostructures. In this material, there is very little coupling between hot electrons and the lattice, and the hydrodynamic regime is thought to be achieved. A drop in $\frac{dV}{dI}$ was attributed to the Gurzhi effect [28, 29], a regime where the viscous electron liquid assumes a Poiseuille-like flow.

The study of electron hydrodynamics received a large impulse with the discovery of graphene. For multiple reasons, monolayer graphene is an excellent material for achieving this regime:

- The electron-electron interaction in clean graphene is remarkably large [30, 31], is strengthened by the lack of screening near charge neutrality, and grows quickly with temperature [25] ($\tau_{ee}^{-1} \propto T^2$).
- Encapsulation in hBN allows exceptionally clean and flat devices [32], which reduces the impurity density and scattering on corrugations.
- At low carrier density, the coupling between carriers and phonons is minimal. When considering the low density Fermi surface (Fig. 13), there are only few possibilities for phonons to scatter electrons. The lattice's stiffness limits the phonon scattering rate [25], which only grows as $\tau_{e-ph}^{-1} \propto T$.
- Umklapp scattering is not allowed in monolayer graphene. Consider the diagram in Fig. 17, showing the first few Brillouin zones of monolayer graphene. The Fermi surface has been shifted to fall entirely inside by choosing a different unit cell [33], leaving the reciprocal lattice vectors \mathbf{G}_1 and \mathbf{G}_2 unchanged. An intravalley Umklapp event has been shown on the left, showing two electrons being scattered from an occupied state (creating a hole, the open circle) to an empty state (creating an excited electron, the full circle). For this scattering to be allowed, the condition

$$k'_1 - k_1 + k'_2 - k_2 = \mathbf{G} \quad (62)$$

must be fulfilled, but for a Fermi surface as small as this, it is obvious this can never be true [34]. The other possible Umklapp scattering, between different valleys, is shown on the bottom right. Again, the condition in Eq. 62 can never be met, since the change in momentum (both solid arrows) can never point in the direction of a reciprocal lattice vectors. With both scenarios (inter- and intravalley) Umklapp prohibited, this cannot be a source of momentum relaxation in monolayer graphene.

Now we can calculate the regime in which hydrodynamic effects should be the strongest in graphene. Fig. 18 from Ref. [35] shows the “hydrodynamic window” of monolayer and bilayer graphene. The ratio between the electron-electron scattering rate and the largest competing (global momentum-destroying) scattering rate is plotted for both materials, as a function of carrier density and temperature. Coloured areas show

where electron-electron scattering dominates, and viscous effects can be expected.

Impurity scattering dominates at low temperature, because it is the only scattering mechanism still present. Phonons are only available at higher temperatures. Impurities are screened more effectively when the carrier density increases, reducing the scattering rate. This explains the white line in the left panel of Fig. 18, which separates the area with stronger electron-phonon scattering from that with stronger impurity scattering.

Recently, there have been a number of experiments trying to find viscous effects in graphene. After their prediction [36], whirlpools in the electron liquids were observed [37] in graphene. The idea is shown in Fig. 19. A fluid with no viscosity flows as shown in the bottom panel: the streamlines (solid white lines) go from source to drain and the potential along them decreases monotonically. This situation changes when there is nonzero viscosity in the fluid, illustrated in the panel on top. Now that momentum will diffuse away from the streamlines (the definition of viscosity), the fluid can be “dragged along” and form whirlpools, shown at both ends of the strip. The resulting potential profile now has many more features, such as a region of opposite potential near the source and drain contacts. These can be measured directly by a local potential probe, proving the existence of viscous electron flow. Another interesting feature is the viscous backflow due to the whirlpools. Counter-intuitively, the electrons flow in the opposite direction at either side of the rectangular geometry. The local resistance would then be negative.

This negative nonlocal resistance is measured in Ref. [37]. In high quality, encapsulated monolayer and bilayer graphene devices, the existence of viscous flow and current whirlpools is indirectly confirmed by the backflow of electrons. The result is shown in Fig. 20 for monolayer (left panel) and bilayer graphene (right panel). The nonlocal resistance R_V is shown in colour as a function of carrier density n and temperature. The blue areas, where it is negative, are then the areas where the viscous effects are strongest. There is a qualitative agreement with the simulation of Fig. 18. For example, the area of negative nonlocal resistance in monolayer graphene is bounded by high and low temperature. The nonlocal resistance is strongest at an intermediate temperature, and fades gradually when the carrier density increases. At low density, a large positive R_V is seen. The authors in Ref. [37] exclude this area from their analysis, claiming it *“is a region our hydrodynamic analysis is not*

expected to be applicable".

A recent theoretical work [38] carefully investigates the whirlpool scenario described above. In the hydrodynamic regime, there is no longer a one-to-one relation between the potential and current distribution in a sample, making it difficult to infer the existence of whirlpools from negative nonlocal resistance. Another study [39] corroborates this and emphasizes the importance of the sample geometry in attributing negative nonlocal resistance to ballistic [40] or hydrodynamic [37] effects.

Another approach to measuring hydrodynamic flow is to study the flow through constrictions [41]. In this experiment, submicrometer constrictions were made in a high quality graphene sheet. In the case of purely ballistic transport, the conductivity of a constriction with width W is given by Landauer's formula [42]:

$$G_{ball} = \frac{2e^2}{h} \cdot N, \quad (63)$$

where $N \approx \frac{2W}{\lambda_F}$ is the number of channels in the constriction, and $\frac{e^2}{h}$ is the quantum of conductance. A factor of two accounts for spin degeneracy. An additive correction is predicted for hydrodynamic flow [43]:

$$G_{vis} = \frac{\pi n^2 e^2 W^2}{32\eta}, \quad (64)$$

where n and η are the carrier density and viscosity. The better-than-ballistic conductivity $G_{tot} = G_{ball} + G_{vis}$ can be understood by considering the velocity distribution of carriers inside the constriction. The ballistic case has a constant velocity profile across the constriction, but in the hydrodynamic regime carriers will form streams that centre in the middle of the constriction, avoiding interactions with the boundaries (Poiseuille flow) [43]. The experiments in [41] confirmed this, and verified a W^2 term in $G_{tot}(W)$.

The experiments above describe small corrections to the conductivity. There has been an ongoing search for unequivocal, "crisp" [44] evidence for electron hydrodynamics in transport.

1.4 Electron-hole puddles

At the Dirac point in graphene (Fig. 1), the DOS is zero. This means there are no available states at this energy, and no free carriers (at zero

temperature). This picture predicts zero conductivity when the chemical potential is brought to the Dirac point.

However, even the earliest experiments on graphene [45, 46] showed a finite resistance at the lowest carrier densities. This was explained [47] by the formation of puddles of electrons or holes.

A study based on scanning tunnelling microscopy (STM) linked the appearance of charge puddles to charged impurities below the graphene sheet [48]. Later, it was shown [49] that charged impurities can only modify the electron density locally, and cannot lead to the smooth variation seen in observations. This work shows, both theoretically and experimentally, that corrugations in height break up the electron liquid in puddles of holes and electrons.

Encapsulating the graphene in boron nitride should then decrease the amplitude of electron-hole puddles. Indeed, an STM study of graphene resting on a hBN flake [50] showed that the charge carrier density in the puddles was up to 100 times smaller than in graphene resting on SiO₂.

A straightforward model of the carrier density n is given in Ref. [51, 52]:

$$n^2 = n_0^2 + (C \cdot V_G)^2. \quad (65)$$

This expression provides a smooth transition between the minimal carrier density n_0 and the carriers originating from a field effect with gate voltage V_G and capacitance C (see section 66).

A thorough investigation on the dominant source of scattering in high-quality graphene [53] linked random strain fluctuations to the strength of the impurity density n_0 . Random fluctuations of the strain in the graphene sheet create pseudomagnetic fields. These fields are the dominant scattering mechanism for charge carriers. This was proven through careful analysis of weak localization and Raman spectroscopy.

1.5 Superlattice effects in graphene

The Brillouin zone in which we have worked so far corresponds to the unit cell of graphene, containing two carbon atoms. This stems from the fact that the largest possible period of potentials in a graphene crystal must be that of the lattice spacing itself.

This situation changes when a potential with an even larger period is imposed upon the graphene sheet. The example we will encounter is that of graphene in contact with a layer of hexagonal boron nitride

(hBN). This is an insulator with a lattice spacing slightly larger (1.8% [54]) than that of graphene. When its lattice is aligned with that of graphene, the hBN will create a Moiré superlattice [55] with a period of 13 nm, far larger than the size of the unit cell.

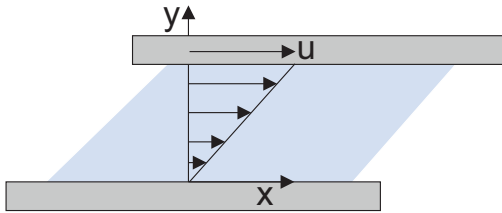


Figure 15: Viscosity as momentum diffusion. The blue liquid is trapped between moving (top) and stationary (bottom) plates. The velocity profile u (arrows) varies linearly from zero at the bottom to maximum at the top. The viscous fluid transmits transversal momentum in the vertical direction.

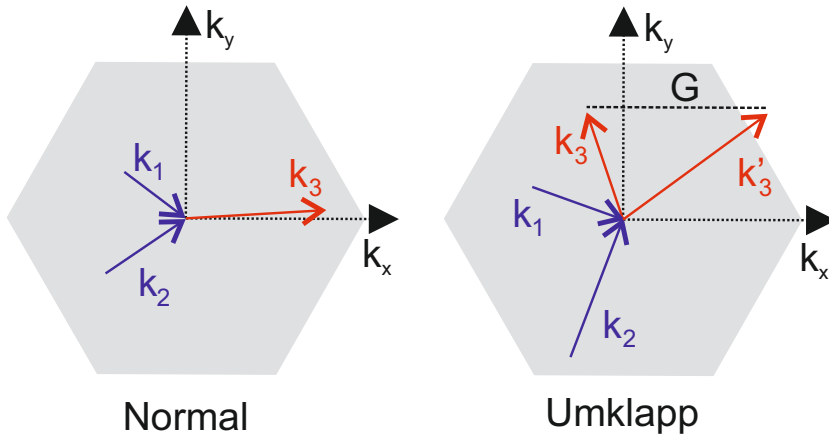


Figure 16: Normal and Umklapp scattering. The normal process on the left conserves crystal momentum ($k_1 + k_2 = k_3$); the Umklapp process on the right does not ($k_1 + k_2 = k'_3 = k_3 + G$). This is allowed since G is a reciprocal lattice vector.

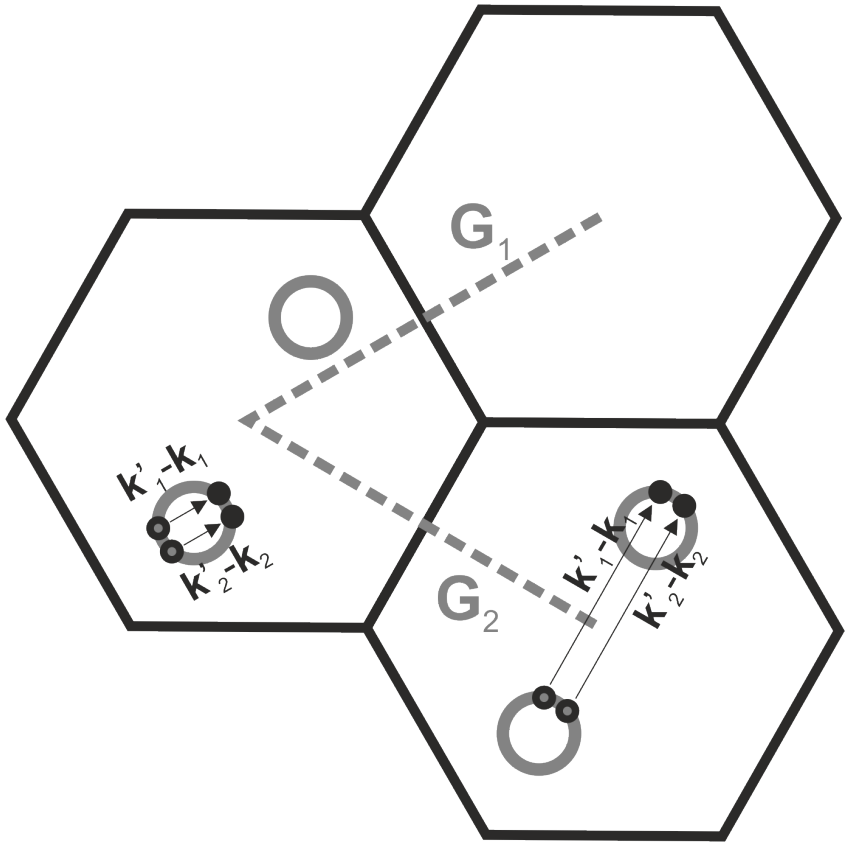


Figure 17: Electron-electron Umklapp processes are not allowed in monolayer graphene. The black hexagons are the Brillouin zone of graphene, shifted to have the Fermi surface (grey circles) completely inside. Two reciprocal lattice vectors are shown in grey (\mathbf{G}_1 , \mathbf{G}_2). On the left, a hypothetical intravalley e-e Umklapp is shown. It is not allowed because the change in momentum ($k'_1 - k_1 + k'_2 - k_2$) will never be a full reciprocal lattice vector. On the bottom right, a hypothetical intervalley e-e Umklapp is shown. The change in momentum will never point in the direction of a reciprocal lattice vector, preventing this process as well.

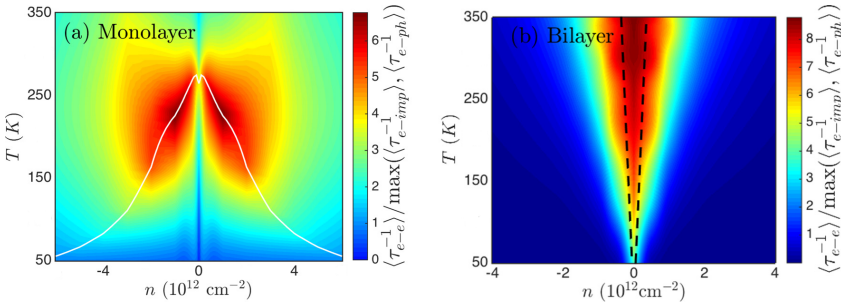


Figure 18: The “hydrodynamic window” as calculated in [35]. The electron-electron scattering rate τ_{ee}^{-1} is compared with the scattering rate of the largest competing mechanism (impurity scattering τ_{e-imp}^{-1} or phonon scattering τ_{e-ph}^{-1}). The results are shown for monolayer (left) and bilayer (right) graphene. The white solid line in the left panel separates the area where $\tau_{e-imp}^{-1} > \tau_{e-ph}^{-1}$ (at low n , T) from the reverse. The black dashed line in the right panel indicates the area at low n where both hole and electron carriers are thermally excited. An impurity density $n_{imp} = 9 \cdot 10^9 \text{ cm}^{-2}$ was used in the simulation, which can be reached in high quality devices. From Ref. [35].

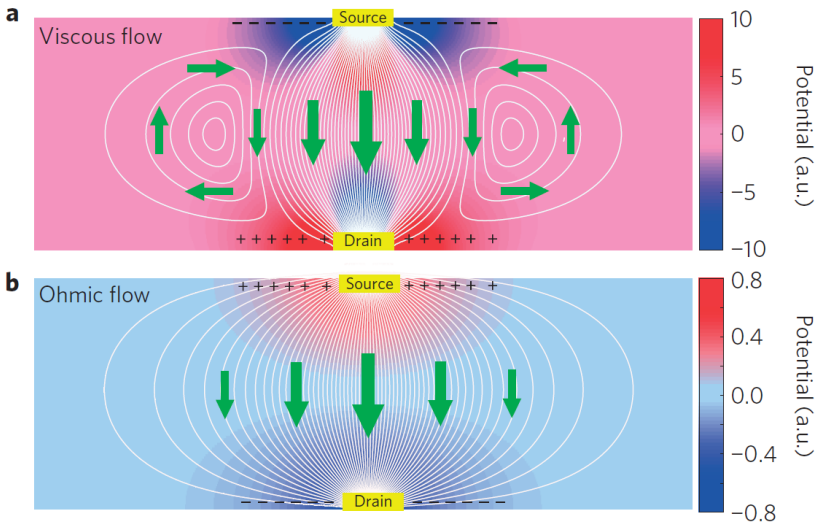


Figure 19: Viscous fluids flow differently. In both panels, current flows from the source at the top of the rectangular strip to the drain at the bottom. The local potential is shown in colour, and the streamlines in solid white lines. The usual Ohmic case is shown in the bottom panel, where the streamlines go straight from source to drain and the potential decreases monotonically along them. In the top panel, whirlpools are predicted to occur. In this case, the streamlines can form closed loops, with multiple sign reversals of the potential along them. From [36].

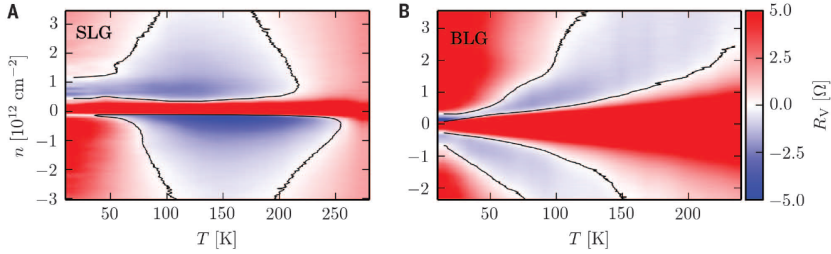


Figure 20: Results of negative nonlocal resistance measurements [37]. The blue areas indicate where a backflow of current is measured, and shows where the viscosity of the electron fluid is strongest. Notice the qualitative agreement with Fig. 18.

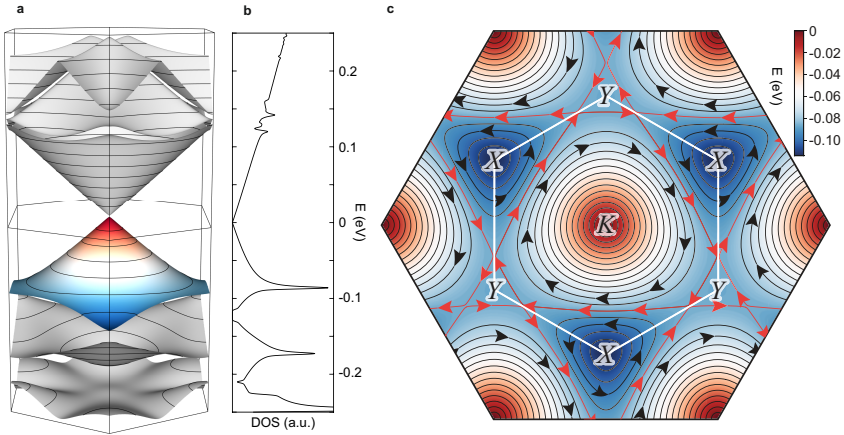


Figure 21: Effects of a Moiré superlattice on the band structure of graphene. (a) New bands in the reduced Brillouin zone. (b) Density of states around $E = 0$. Note the similarity with Fig. 1, and the drastically lower energies. (c) Contour plot of the conductance band. At low enough energies, the Fermi contours no longer encircle K (red, electrons), but encircle X (blue, holes).

This additional potential with a large period will shrink the Brillouin zone, and the bands of Fig. 1 will be folded back. The new situation is illustrated in Fig. 21. The band structure in the reduced Brillouin zone is shown in panel a; the new DOS in panel b. The Dirac cone around K is shaded in red at $E = 0$. At lower and higher energies, a VHS is visible. Note the great similarity with the band structure of Fig. 1. The greatest distinction, however, is the compressed energy scale. Zone folding brings the VHS from 2.7 eV down to approximately 100 meV. This is well within the reach of conventional capacitive gating.

Panel b shows minima and maxima in DOS that were absent in Fig. 1. It is worth noting that these minima in DOS are directly visible in experiment as additional maxima in resistivity at the matching gate voltage [3]. The observation of these peaks proves the presence of a superlattice potential, and allows to calculate the corresponding twist angle [54, 55].

Panel c shows the contour plots of the valence band. Around $E = 0$, the charge carriers circle around K and are electron-like. As the chemical potential is lowered, the contours become larger until they shift into pockets around X . The charge carriers are now hole-like. This is again a Lifshitz transition caused by the change in Fermi surface topology. Hence, the Lifshitz transition in graphene in a Moiré superlattice is available at lower energies than the one in Fig. 3. This was used in several studies [55, 3] to study the physics of a VHS. They found a change in carrier type, a change in Berry phase and an enhancement of the effective mass at the expected densities.

1.6 Controlling the carrier concentration

While the chemical potential μ of intrinsic graphene lies at the Dirac point ($E = 0$ in Fig. 1), it is useful to be able to control its location. The most convenient manner is by using a *gate*. Graphene is placed on a thin insulator (e.g. SiO₂ or hBN). A conductive layer (doped Si or graphite) lies on the other side. In this way, the graphene and the metal gate are capacitively coupled, and a bias across them changes the carrier concentration in the graphene.

Generally, the induced charge carrier concentration n depends linearly on bias voltage V :

$$e \cdot n = C \cdot V \tag{66}$$

where C is the total capacitance. The different components to the total capacitance are discussed below.

This expression can be expanded to encompass very low carrier densities when the Fermi level is brought to the Dirac point. Instead of the complete absence of charge carriers, $n = 0$, “puddles” of electrons and holes will spontaneously form [47], as treated in section 1.4. These cannot be avoided, but the resultant *impurity density* n_0 can be reduced by improving the quality of the graphene devices. It represents the carrier density below which the graphene cannot be depleted, creating a minimal conductivity. The carrier density will saturate when the Fermi level is brought to this region, described by Eq. 65.

We now turn to the different contributions to the capacitance C in Eq. 66. The largest contribution to C is C_{geo} , the geometric capacitance.

$$C_{geo} = \frac{\epsilon\epsilon_0}{t} \quad (67)$$

In this expression, ϵ is the electric permittivity of the insulator (e.g. $\epsilon = 3.9$ for SiO_2 [56] or $\epsilon = 3 - 4$ for hBN [32]), $\epsilon_0 = 8.85 \cdot 10^{-12} \text{F/m}$ is the permittivity of vacuum and t is thickness of the insulator.

As charge carriers are added to the layer of graphene, the chemical potential shifts. This is described by the thermodynamic compressibility $\frac{\partial n}{\partial \mu}$, which is equal to the noninteracting DOS of the material, plus exchange and correlation effects [57, 58]. This effect contributes to C [59] as the “quantum capacitance” $C_Q = e^2 \cdot \frac{\partial n}{\partial \mu}$ so that the total capacitance is given by $C^{-1} = C_{geo}^{-1} + C_Q^{-1}$.

In the limited window of operation of a capacitive gate (a few volts before a hBN dielectric layer breaks down, around 100 V for a SiO_2 dielectric), the linear DOS of graphene (Fig. 1) around $E = 0$ makes the quantum capacitance a vanishingly small contribution to the capacitance. However, at large enough biases, measuring the quantum capacitance is a viable way of determining the DOS of two-dimensional materials [57]. In what follows, we will assume that the capacitive coupling between graphene and metal gate only encompasses the geometric contribution C_{geo} .

Capacitive gating is a very convenient way of controlling the chemical potential around the Dirac point, but cannot reach the multiple eV required to reach the VHS. Electrolytic gating is a more powerful technique, where the dielectric and gate are replaced with a conductive liquid, the electrolyte. The electrolyte directly touches the graphene, and

when biased, the charged components of the liquid will cluster directly on top of the graphene. This creates an extremely thin capacitor (with a displacement of around 1 nm) [61] that can induce a very large charge carrier concentration (on the order of 10^{14} carriers per cm^2). Still, this is not enough to reach the VHS [62, 63], which would require a density of $9.5 \cdot 10^{14} \text{cm}^{-2}$ in a tight-binding model [64].

An even more drastic method of inducing charge carriers in graphene was described in Ref. [60] and is shown in Fig. 22. By repeated deposition, adsorption and intercalation of alkali metals, a large electron concentration can be achieved. The succession of figures represents different combinations of metals, culminating in the largest doping level, where the VHS was reached. This is visible in the final panel by the spectral intensity at M . The deposited monolayers of K and Ca are however extremely unstable, and cannot survive outside of the growth chamber.

This is the approach we will follow to study graphene at the VHS. A different intercalant, Gd, was used to circumvent the stability issues. The complete description of the growth process is described in section 2.2.1.

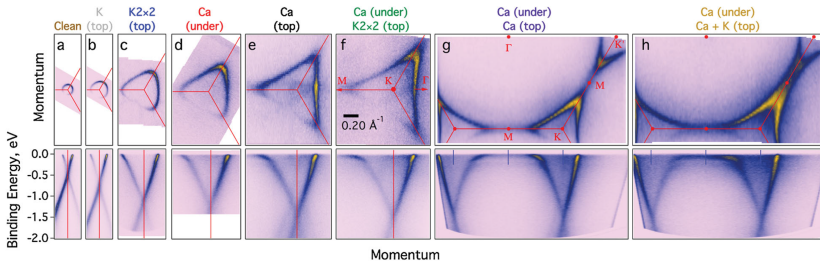


Figure 22: Band structure of intercalated graphene. By depositing various combinations of alkali metals, electrons are induced in graphene, visible in the wider Fermi contours (upper panels) and lowering of the Dirac point (lower panels). From Ref. [60].

2 Fabrication and characterization of graphene devices

Graphene devices at low and very high carrier density require very different fabrication methods. This chapter describes first how high-quality van der Waals heterostructures (“stacks”) are made. The other part will concern the growth and intercalation of graphene layers from a SiC host crystal, required to reach high doping levels.

2.1 Fabrication of graphene stacks

As-grown bulk crystals of two-dimensional materials all consist of individual layers that are weakly bound by one another by van der Waals forces [65]. The key realization that these crystals could be cleaved by simple mechanical exfoliation was the start of the field of two-dimensional materials [66]. The van der Waals heterostructures in this thesis are based around graphene sandwiches between layers of hexagonal boron nitride (hBN), which greatly increases the quality of the graphene [32].

This section covers the procedures. Exact recipes will be given in Appendix A.

2.1.1 Exfoliation of two-dimensional materials

The procedure starts with bulk crystals of hexagonal boron nitride and graphite and a substrate (usually a SiO₂-capped Si wafer). By pressing the tape against the crystal, a piece of the crystal is removed. By successively applying scotch tape to this fragment, the crystal can be thinned down to a single atomic layer. It can then be deposited on the wafer for further processing.

A typical image of exfoliated flakes is visible in Fig. 23. Flakes can be inspected and selected for desired thickness, flatness and size. On the left, a large graphene flake is visible, surrounded by larger pieces of graphite. With a bit of experience, monolayer graphene can be distinguished from multiple layers by inspection. Later, the quantum Hall plateaus in electrical transport (e.g. Fig. 54) are another verification of the layer number. On the right of Fig. 23, hBN flakes can be seen. Again, with some experience, the colour of the flakes can be used to pick those with the desired thickness.

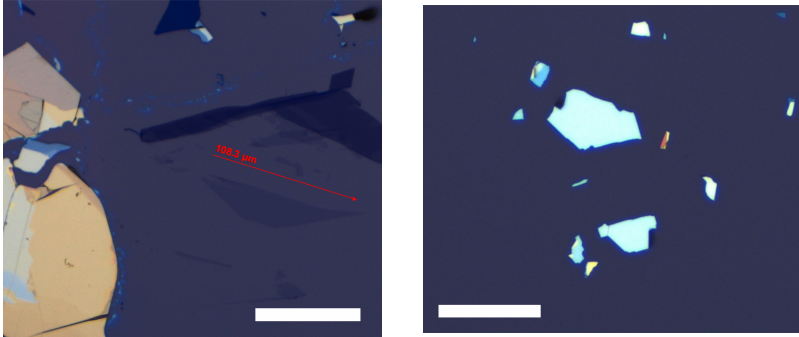


Figure 23: Graphene (left) and hBN (right) flakes after exfoliation, as deposited on Si/SiO₂ substrates. The scale bar is 80 μm .

2.1.2 Van der Waals heterostructures

At this stage, the assembly of a van der Waals heterostructure can begin. Depending on the desired structure, multiple flakes of two-dimensional materials can be stacked on top of each other. The procedure takes place in a stacking tool, shown in Fig. 24. It allows temperature control of the substrates, combined with positional control in x , y and z directions and visual feedback via a microscope.

We start with a droplet of polymer on a glass slide. Using the stacking tool, the flake to be picked up can be approached by the polymer drop, brought into contact and lifted off the Si/SiO₂ substrate. The flake, in this case hBN, now lies on the polymer drop. This step is performed at high temperature to obtain the desired stickiness.

Switching to another flake (e.g. graphene), this step can be repeated. This flake can be picked up with the hBN flake already on the polymer drop. When picking up more than one flake, special care must be taken to approach slowly, and without raising the polymer drop until all flakes are picked up. This would create wrinkles, cracks and bubbles in the stack, reducing the quality of the end product.

With all desired flakes on top of each other, lying on the polymer drop, this stack can now be deposited. A Si/SiO₂ substrate with markers is placed in the stacking tool. This will be the final resting place for the stack. The markers aid with alignment during lithography. The substrate is heated up further, so that the polymer will become malleable

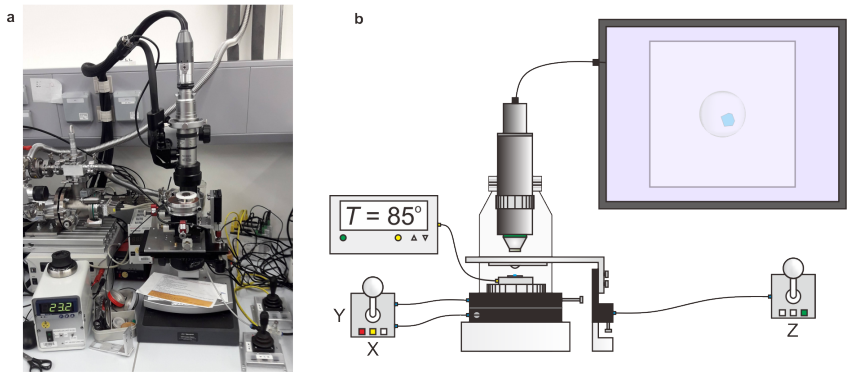


Figure 24: The stacking tool to fabricate van der Waals heterostructures. (a) Picture of the device. (b) Schematic of the stacking tool. The central horizontal arm holds a glass slide with a droplet of sticky polymer. The Si/SiO₂ substrate with flakes is just below, and can be manipulated in every direction (x , y and z -direction controllers). Its temperature can also be controlled with a heater. The microscope on top shows the alignment of the polymer bubble and the flake to be picked up (screen in the upper right). Figure courtesy of Youngwook Kim.

as it crosses the glass transition temperature when it is brought into contact with the hot substrate. The stack now rests on the substrate with markers, in a bubble of polymer, which can be washed away.

This substrate with stack is now annealed to remove the last impurities. High-temperature annealing can also make the layers of the stack align themselves to minimize their energy. This can form a Moiré superlattice [55], which has been treated in section 1.5.

At this point, the stack looks like the one in Fig. 25. It can be patterned into the desired shape (square, Hall bar, Tesla valve) by lithography. This technique involves coating the substrate in a thin layer of a photosensitive polymer, the so-called resist. After exposure (either to light of the correct wavelength or high-energy electrons), the links between the polymer chains are broken and the polymer becomes locally soluble. In this work, electron beam lithography is chosen, in which an electron beam selectively modifies the resist with remarkable accuracy (20 nm details are possible). After exposure, the chosen areas are dissolved. The exposed areas can be etched away and the remaining resist removed.

2.1.3 Final steps

The next step is fabricating electrical contacts. The areas are defined with electron beam lithography again, and the hBN is etched away so the graphene is exposed. Next, the sample is placed in the evaporation chamber, where a thin layer of chrome and a thin layer of gold are thermally deposited on top. We remove the unwanted metal by dissolving the remaining resist, and the contacts are ready. The stack now looks like Fig. 26.

Finally, the contacted stack is cleaned with contact mode atomic force microscopy (AFM). The AFM tip is carefully brought into contact with the stack, and sweeps over the surface. This is thought to reduce the nanometer-scale corrugations in the stack, increasing the quality [67, 68]. A picture of this is shown in Fig. 27.

At this stage, the patterned, contacted stack is ready to be measured.

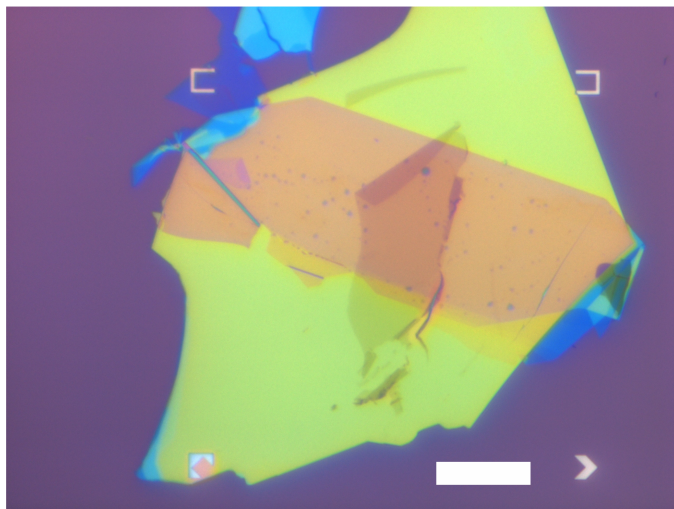


Figure 25: A typical van der Waals stack after the stacking procedure is complete. Two hBN flakes are visible in orange and yellow. The grey area in the center is a layer of graphite. A graphene monolayer is usually not visible inside the stack. The scale bar is 20 μm .

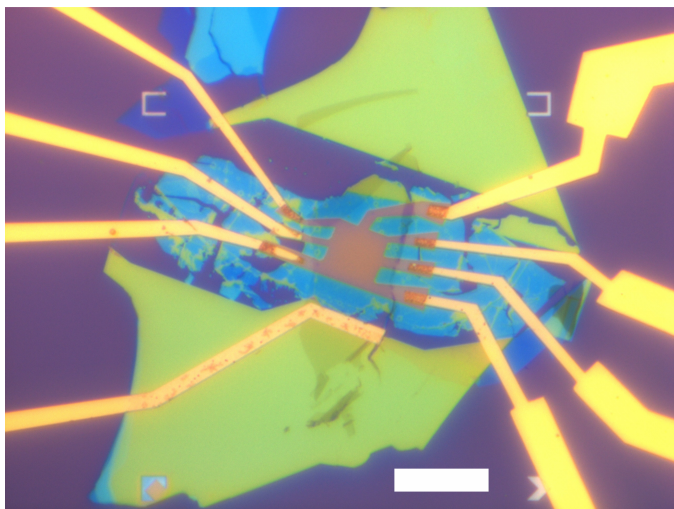


Figure 26: The stack of Fig. 25, now patterned into a square with electrical contacts (gold). The scale bar is $20 \mu\text{m}$.

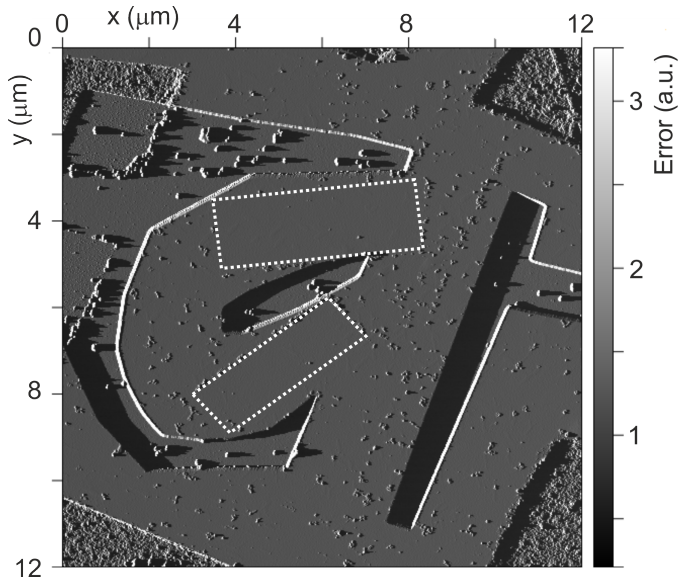


Figure 27: An AFM scan of the device in Fig. 26. The residues of multiple lithography steps are visible as specks on the flat surface. Two rectangular areas (on the Tesla valve “branch”, marked with white dots) have already been cleaned with contact mode AFM. This was repeated until the whole device was clean.

2.2 Highly-doped intercalated graphene

The highly doped graphene at the Van Hove singularity is fabricated in a completely different manner. The growth and ARPES were performed by Stefan Link at the Surface Analysis group of the Max Planck Institute, headed by Ulrich Starke. It is fully described in Refs. [69, 64]. Below, this process is described in brief, followed by a description of the ARPES results, the contacting and the measurement process.

2.2.1 Doping graphene to the VHS

The preparation process starts with 6H-SiC(0001), a polymorph of SiC which can be thought of containing alternating layers of silicon and carbon. The topmost layers of Si atoms can be selectively sublimated by annealing. This leaves a layer of loosely bound and disordered carbon atoms behind. This is shown in Fig. 28a, where a graphitic layer (green) is loosely connected to the SiC host crystal, with many dangling bonds (DBs).

Afterwards, the atoms to be intercalated are deposited and the sample is annealed again. The intercalants diffuse underneath the graphitic layer and passivate the SiC dangling bonds. The graphitic layer is arranged into a quasi-free standing graphene monolayer. Fig. 28b shows this situation.

Of note is that these steps require careful optimization to obtain a monolayer of graphene that is fully intercalated. In contrast to a self-terminating process (such as the growth of graphene on copper substrates), the reaction does not terminate when a monolayer is reached. This makes it possible to evaporate too much silicon, leave too much carbon or deposit too much or too little of the intercalant species, reducing the quality of the graphene.

This intercalation method can grow extremely large (several cm^2) and homogeneous graphene layers [70, 71]. The choice of intercalant atomic species offers great flexibility, too. Several atomic species have been used successfully [69], and this is still an active field of research.

For this research, the intercalant of choice was gadolinium (Gd), which was found to strongly dope the graphene. Through careful optimization, the Starke group obtained high-quality highly doped graphene, the transport properties of which were examined in this thesis.

2.2.2 Characterization of intercalated graphene

After fabrication, the intercalated graphene is characterized by angle-resolved photoemission spectroscopy (ARPES). An overview of ARPES is given in section 2.3. The main results, the energy dispersion taken at approximately 130 K, are shown in Fig. 29. In panel a, the dispersion along the KMK' line shows the filled states at $E = E_F$, at the M point. This is proof the VHS has been reached. Furthermore, panel b shows the familiar linear dispersion of monolayer graphene. The large electron doping has shifted the Dirac point downwards by 1.6 eV.

Fig. 29c displays the Fermi surface of intercalated graphene. Again, the states at M are filled. The triangularly warped pockets around K and K' are touching at the M points. The Fermi surface no longer consists of separate pockets, but of a single large pocket around Γ .

The surprising flatness of the bands, and a self-consistent band structure calculation at these high densities is presented in Ref. [64].

2.2.3 Contacting and manipulation of intercalated graphene

The intercalated graphene, resting on the SiC wafer, is now ready for measurements. One experimental drawback is the sensitivity to air of the material. The gadolinium intercalant will readily oxidize in ambient conditions, removing all electron doping. To successfully probe the physics of graphene at the VHS, the samples must therefore be brought into the dilution fridge without oxygen contamination. This process, from growth chamber to dilution fridge and back, is presented in Fig. 30.

- The preparation of the Gd-intercalated graphene takes place in a growth chamber in ultrahigh vacuum (UHV). The high doping is confirmed by ARPES measurements (section 2.2.2).
- The sample is moved from the growth chamber into a portable vacuum suitcase. This “suitcase” is a small vacuum chamber that can be detached and brought to a glove box, a chamber with argon atmosphere in which samples can be manually contacted.
- Inside the glove box, the sample is attached to a sample carrier and electrical contacts are made. Thin indium wires are pressed into the edges of the SiC substrate.

- The contacted sample is loaded into the sample rod of the dilution fridge. By adding a gate valve, the sample rod will remain filled with argon until it is connected to the dilution fridge.
- The sample rod, attached to the dilution fridge, is pumped to vacuum. Afterwards, the intercalated graphene sample is loaded inside, cooling it down to millikelvin temperatures in a helium atmosphere.
- At this point, the electrical characteristics of intercalated graphene are measured.
- With the measurements complete, the sample is taken out of the fridge and back into the sample rod.
- The sample rod is connected to the glove box, where the sample is taken out and the contacts removed.
- The intercalated graphene sample is inserted in the vacuum suitcase again, which remains filled with argon.
- The vacuum suitcase is connected to the ARPES chamber and pumped down to UHV.
- At this stage, the sample is analysed again, confirming the large carrier density is still present and no oxygen contamination has taken place.

2.3 ARPES

Finally, we consider a characterization method that allows the direct measurement of the energy dispersion of a material, angle-resolved photoemission spectroscopy (ARPES).

ARPES is based on the photoelectric effect, in which electrons are expelled from a material by incident photons. In this process, energy is preserved, so that [72]

$$h\nu = E_B + \Phi + E_{kin}, \quad (68)$$

where $h\nu$ is the photon energy, E_B is the binding energy of the electron (the energy needed to bring it to the Fermi level), Φ is the work function of the material (the energy to bring an electron from the Fermi level to

the vacuum level) and E_{kin} is the kinetic energy of the electron in free space.

Fig. 31 depicts the basics of ARPES. In panel a, an electron in the sample is expelled by a photon (red) with energy $h\nu$. It now travels through vacuum with energy E_{kin} , obeying Eq. 68 and enters the electron analyser. This tool “sorts” the electrons by guiding them through a magnetic field. Electrons with different energies will hit different spots on the detector, as their radius of curvature depends on E_{kin} .

Fig. 31b shows how the binding energy E_B of an electron in the sample is mapped onto the kinetic energy E_{kin} of the emitted electron in vacuum by a photon. If this is repeated many times, the entire density of states of the sample (yellow) can be measured (blue) by the distribution of kinetic energies of the electrons.

More information can be obtained by considering conservation of momentum. This is shown in the lower panel of Fig. 31a. During photoemission, momentum is only conserved in directions parallel with the plane of the sample:

$$k_{\parallel}^i = k_{\parallel}^f \quad (69)$$

$$k_{\perp}^i \neq k_{\perp}^f, \quad (70)$$

where i and f are the initial and final states of the electron. Note that Eq. 69 ignores the momentum of the incident photon [73]. With detailed information about the emission angles θ and ϕ and assuming the free electron dispersion $E = \frac{\hbar^2 k^2}{2m_0}$, the full band dispersion of the sample can be measured. An example of a band structure measured by ARPES is shown in Fig. 29.

ARPES is a very versatile tool to determine band structures, but suffers from a few limitations, which are listed below.

- The need for a photoemitted electron means only the filled bands can be measured.
- The sample must be conductive, as grounding the sample is necessary to prevent charging.
- ARPES is limited to zero external magnetic field, since the emitted electrons must travel through the detector in a straight line.

- Finally, most of the emitted electrons will come from the topmost layers of the sample. This surface sensitivity favours freshly prepared or cleaved two-dimensional materials, such as graphene or cuprate superconductors.

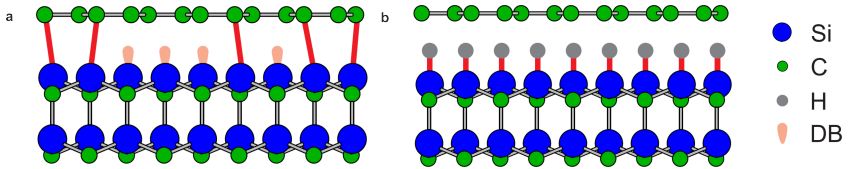


Figure 28: Growth and intercalation of highly doped graphene from SiC. (a) After annealing, Si atoms are selectively removed from the top layers, leaving loosely bound graphitic layers. (b) Depositing an atomic species (here, hydrogen) and subsequent annealing leads to passivation of the SiC host crystal and the formation of a graphene layer. DB stands for dangling bonds. Adapted from [64].

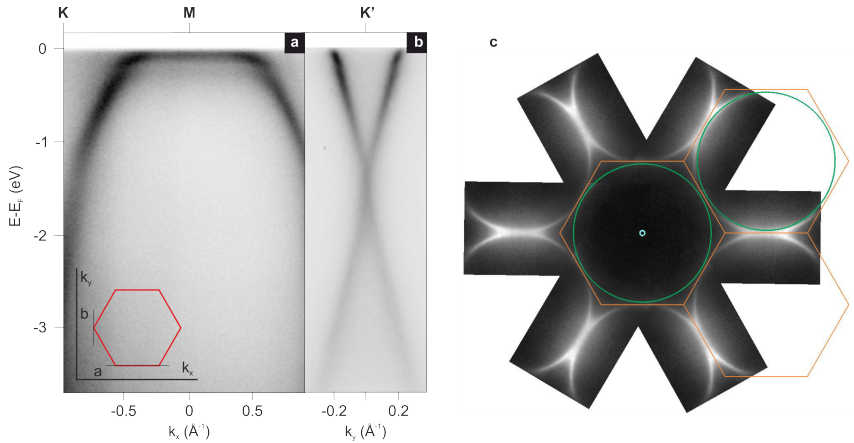


Figure 29: ARPES of intercalated graphene. (a,b) Measured $E(k)$ along two different directions. (c) Fermi surface ($E = E_F$). The Brillouin zone is indicated in orange, the circular Fermi surface in green. This figure is obtained by arranging copies of a single measurement in a hexagon. Inset: locations of the cuts a and b in the Brillouin zone. Modified from Refs. [69, 64].

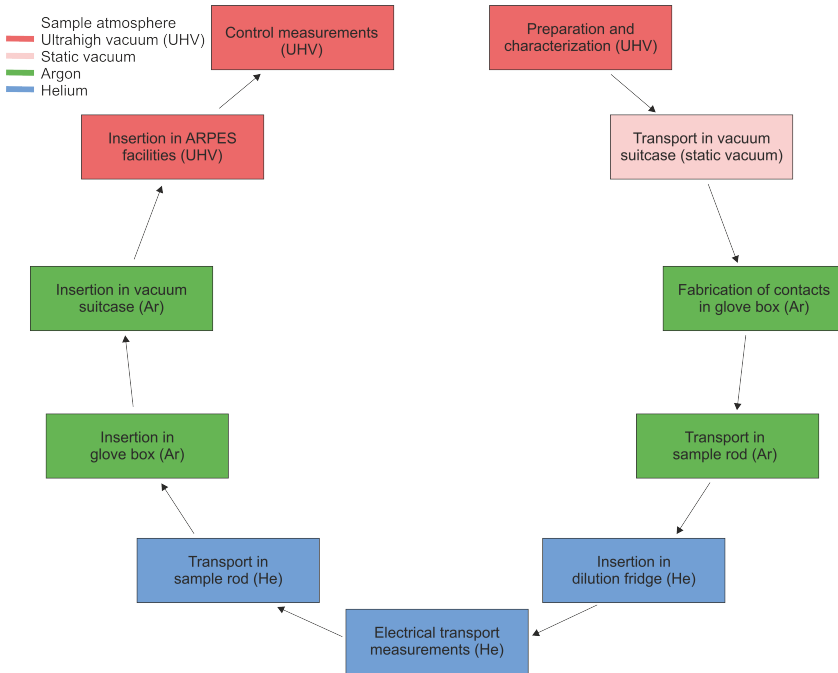


Figure 30: The process flow for handling and contacting Gd-intercalated graphene, which is sensitive to oxygen. The colours refer to the atmosphere the sample is in at every step. Adapted from [69].

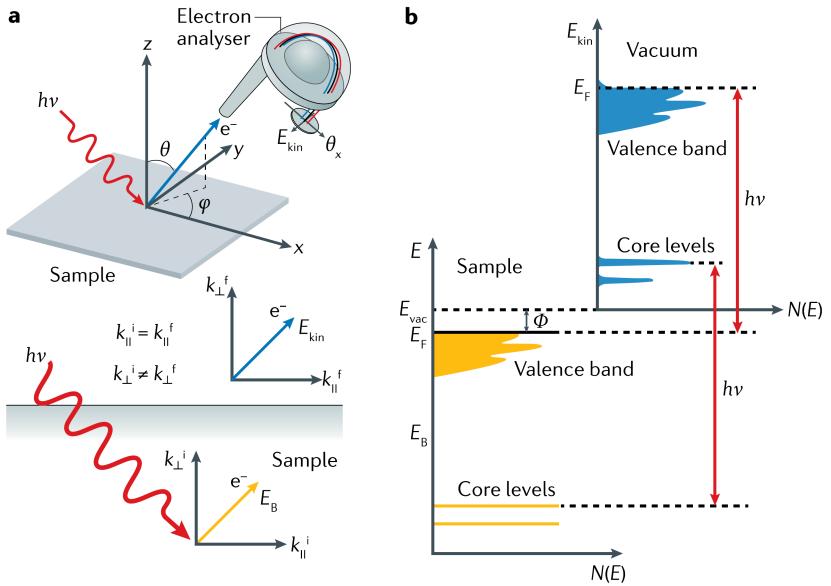


Figure 31: Overview of ARPES. (a) A photon hits the sample with enough energy to expel an electron. The direction (angles θ and ϕ) and energy of the electron are determined in the hemispherical analyser. In the lower panel, the conservation laws are depicted, as described in the text. (b) Energy conservation in the photoemission process, formulated in Eq. 68. This shows how the DOS of the material (yellow) is translated into a measured DOS (blue). From Ref. [73].

3 Magnetotransport at the Van Hove singularity

We are now ready for the first experimental chapter, which concerns graphene at the VHS. The preparation was described in section 2.2.1. Before we can interpret the results, we must first discuss a different material class, the cuprate superconducting compounds, in order to draw parallels with highly-doped graphene.

3.1 Pseudogap in cuprate superconductors

The discovery of superconductivity at 35 K in $\text{LaBa}_2\text{Cu}_3\text{O}_7$ (LBCO) by Bednorz and Müller [74] caused great excitement in the field. Previous research had focused on simple, stoichiometric compounds such as Nb_3Sn and NbTi , stalling at a largest critical temperature (T_c) of 23 K. The discovery of LBCO in 1986 showed the great potential of complex, non-stoichiometric compounds, and a gold rush in the new field of *cuprate superconductors* followed. In the following years, many more members of this class were discovered, each with the same characteristics: high T_c and the presence of CuO_2 planes. The CuO_2 planes are believed to be the location of the superconductivity, and are separated by insulating layers that function as a charge reservoir.

Some cuprates are more suitable for certain experimental methods [75, 76]:

- $\text{La}_{2-x}\text{Sr}_x\text{CuO}_2$ (LSCO). Large crystals (larger than 1 cm) can be grown, making it suitable for neutron diffraction experiments, which probe the magnetic structure. It is unsuitable for STM, since this crystal does not cleave with a clean CuO_2 plane.
- $\text{YBa}_2\text{Cu}_3\text{O}_{7-x}$ (YBCO). A class with a very high T_c (93 K when optimally doped), it has been used commercially for magnetic field sensing in high- T_c SQUIDs. Crystals can be made with very high purity, making it suitable for studies of quantum oscillations [77]. However, the presence of a second Cu-O plane makes STM and ARPES difficult.
- $\text{Bi}_2\text{Sr}_2\text{CaCu}_2\text{O}_{8+x}$ (BSCCO). Members of this class can be cleaved easily along the CuO_2 plane, making it the cuprate of choice for surface-sensitive techniques such as STM and ARPES. The highest

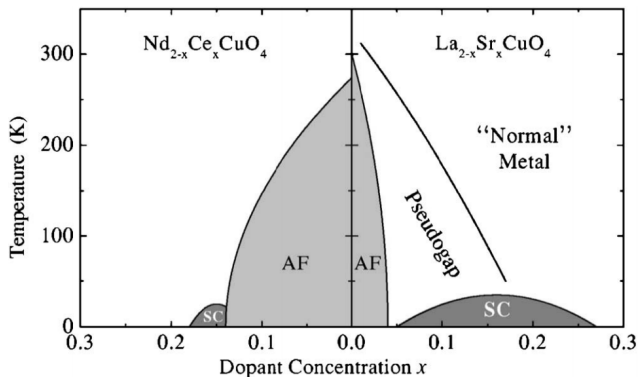


Figure 32: Typical phase diagram of the cuprate material class. The doping concentration x of the material determines the concentration of holes or electrons. A remarkable variety of electronic phases (AF, antiferromagnet and SC, superconductor) emerges away from stoichiometric doping ($x = 0$). From Ref. [78].

T_c at ambient pressure in any material (135 K) has been measured on a member of this class of cuprates. This material has been used in superconducting wires.

All of these compounds have a parameter x , the doping level. When undoped, $x = 0$, the cuprates are stoichiometric compounds, and behave as insulators. Only when excess carriers are introduced, be it electrons or holes, through atom substitution or oxygen deficiencies, do these materials show an abundance of electronic phases, illustrated in Fig. 32.

In this figure, a typical phase diagram of a cuprate superconductor is shown. The doping level from the composition of the material x determines the concentration of electrons or holes. Around zero doping ($x = 0$), the cuprates are antiferromagnetic (AF) insulators. When free carriers are introduced, this phase quickly vanishes and the material becomes conductive. At high enough doping, the typical superconducting domes are reached. “Optimal doping” refers to the doping at which T_c is maximal. At even higher doping, the system behaves as a normal Fermi liquid. Fig. 32 also indicates the appearance of a pseudogap in the underdoped cuprates. The specifics of this high-temperature phase will be

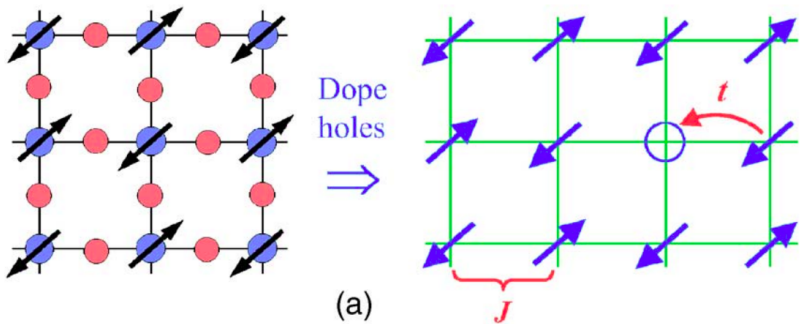


Figure 33: Sketch of the electronic configuration in a single CuO layer in a cuprate. The arrows denote the spin of the electrons. In the left panel, every Cu atom is occupied and AF order with exchange energy J is the lowest energy configuration. In the right panel, one electron is missing, creating a hole that can hop with amplitude t . From Ref. [78].

explained later.

An intuitive argument for the breakdown of antiferromagnetism and the richness of the cuprates is shown in Fig. 33. This figure shows a single Cu-O plane. If every copper atom (blue circles) is occupied with a single electron (left panel), the lowest energy configuration is antiferromagnetic. There are no mobile charge carriers. This corresponds to the situation around $x = 0$ in Fig. 32.

The right panel of Fig. 33 shows the same Cu-O plane, but with a single electron removed. The resulting hole is mobile, and can hop through the plane with hopping amplitude t . This is the kinetic energy by which the energy of the system would be lowered. However, after hopping, the hole is no longer in an antiferromagnetic environment. It is surrounded by three spins in the same direction, creating an energy cost [79] of $\frac{3}{2}J$. This already shows how easily itinerant charge carriers destroy the AF background.

The physics of the cuprates is captured [78] in this conflict between the kinetic energy t and the exchange energy J . When $xt \gg J$, the kinetic energy is dominant and the system is a Fermi liquid with a weak residual AF order. When $xt < J$, the situation is less clear as the system wishes to preserve antiferromagnetism and to maximize the kinetic energy of the

charge carriers. A doping level of roughly $x = J/t \approx \frac{1}{3}$ is the starting point of a normal metallic state. The interesting physics of the cuprates only emerges below this doping concentration (Fig. 32).

3.1.1 d -wave gap and pseudogap

The Fermi surface of a generic overdoped cuprate superconductor in the normal phase is shown in the bottom right of Fig. 34. The theoretical single-band calculation (yellow line) is confirmed by ARPES measurements. Note that the large hole-like Fermi surface is close to a Van Hove singularity [80], which has been linked to some of the strongly correlated phenomena in these materials [81, 82, 83, 84].

At lower temperature, the material enters the pseudogap regime, where a portion of the Fermi surface is gapped out. This is visible in the top right panel of Fig. 34 as the black areas near $(0, \pi)$ and $(\pi, 0)$. Remarkably, only disconnected arcs are observed. This is in complete disagreement with the Fermi surface of conventional metals, which always follows a closed loop. It is possible these arcs are simply the fronts of electronlike Fermi pockets [85], but the search for and the existence of the “backside of the pocket” is a matter of intense debate [86].

At even lower temperature, the material becomes superconducting. The superconducting gap (Δ_{SC}) and pseudogap (Δ_{PG}) are shown in the left panel of Fig. 34. The typical d -wave nodal-antinodal pattern is visible. Here lies the biggest difference with s -wave BCS superconductors, in which the superconducting gap has a constant value and does not depend on the wavevector.

The interpretation of the pseudogap and its link with the superconducting dome have been contentious since the earliest reports [87]. The similarity between Δ_{SC} and Δ_{PG} has led some [88] to interpret the pseudogap as the preforming of incoherent superconducting Cooper pairs. An overview of the recent work in the field is given in Ref. [86].

3.1.2 Transport signatures in the pseudogapped cuprates

The spontaneous gapping of a part of the Fermi surface is not only visible in ARPES, it is also visible in studies of the electronic transport in cuprates. This will be discussed in this section.

The loss of DOS at the Fermi energy when entering the pseudogap directly entails a drop in conductivity [89, 90, 91, 92], as the number of

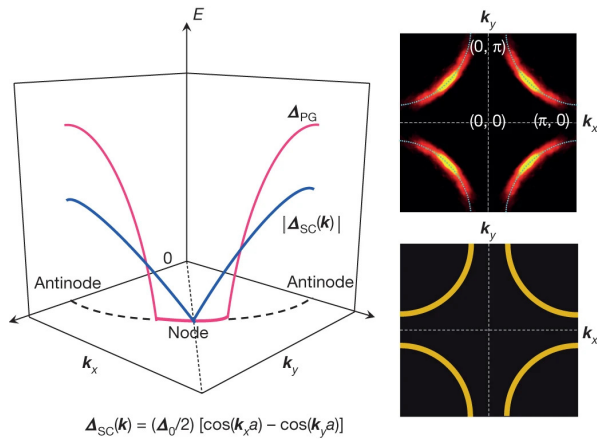


Figure 34: Band structure properties and gaps of the superconducting cuprates. Left panel: energy gaps in the pseudogap (Δ_{PG}) and superconducting phases (Δ_{SC}). Their dependence on the wave vector (k_x, k_y) is a hallmark of d -wave superconductors. Right panel: the measured Fermi surface in the pseudogap regime (top) consists of discrete Fermi arcs. It matches the predictions of the normal regime band structure (bottom), except for the antinodal areas at $(0, \pm\pi)$ and $(\pm\pi, 0)$, which are gapped out. Figure taken from Ref. [86].

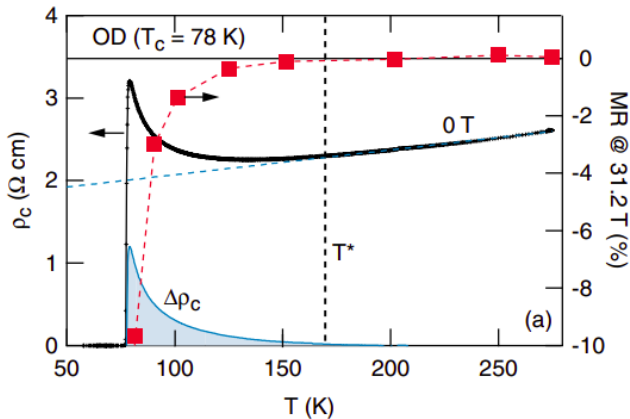


Figure 35: Insulating behaviour in overdoped BSCCO. When lowering the temperature, the resistivity (black line) first decreases, but then increases at the pseudogap temperature T^* . At the same temperature, negative magnetoresistance (red squares) appears. From Ref. [89].

charge carriers at the Fermi energy decreases. This is visible as insulating behaviour at low T , seen in Fig. 35. The resistivity (black line) only increases below a characteristic temperature, which we identify as the pseudogap temperature T^* . Here, the pseudogap starts opening and the DOS at the Fermi level decreases, which is directly visible in a measurement of the resistivity.

This figure shows the effect of an applied magnetic field as well. The red squares denote the change in resistance (in percent) when the sample is brought in a field of 31.2 T. Above T^* , there is little change. In the pseudogap regime, there is a pronounced decrease, which gets stronger as the temperature is lowered further. Below 78 K, the sample is superconducting and no longer has resistance. This appearance of negative magnetoresistance is widespread in the pseudogapped cuprates [93, 89, 91] and has been interpreted as the destruction of the pseudogap by the magnetic field. As the field increases, the DOS returns to that of the normal state and the conductivity increases. This is analogous to the destruction of the superconductive state by a magnetic field.

Another characteristic of the pseudogapped cuprates is the variation

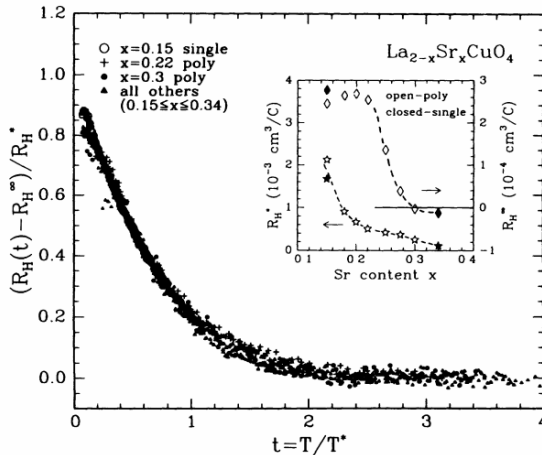


Figure 36: Hall effect in pseudogapped LSCO. Many Hall curves have been recorded, and collapse on a universal line when rescaled as described in the text. In general, above the pseudogap temperature ($T/T^* > 1$), the Hall coefficient R_H is small and temperature independent. Below T^* , R_H is large and strongly temperature dependent. The inset shows the scaling parameters used. From Ref. [94].

of the Hall effect. In simple metals, the Hall effect usually does not depend on temperature (see section 1.2.1). In more complex materials such as the cuprates, a temperature dependence has been observed [94, 95, 96].

Generally, the Hall coefficient in the normal metal is small and temperature independent, as is expected from a normal metal with a large carrier density. This changes when the material is cooled down below T^* . The Hall coefficient now increases in magnitude and is strongly temperature dependent. A typical case is presented in Fig. 36. Many different $R_H(T)$ traces, measured across many compositions and doping levels, have been collapsed onto the same universal curve $f(T/T^*)$. The Hall coefficient was rescaled as

$$R_H \left(\frac{T}{T^*} \right) = R_H^\infty + R_H^* \cdot f \left(\frac{T}{T^*} \right) \quad (71)$$

where R_H^∞ is the Hall coefficient at high temperature and R_H^* is a scaling factor.

Recently, the change in Hall coefficient was linked [90, 97, 92] to a change in Fermi surface topology. The presence of a charge-density wave (CDW) [92] or other competing phases obscures the identification of the mechanism, but a theoretical study demonstrates [98] a link between the Van Hove singularity and the pseudogap. They argue that, for a square lattice, a pseudogap can only open at (at most) the doping level at which the Lifshitz transition occurs. Their material of study, BSCCO, demonstrates this behaviour: the pseudogap only opens at the exact doping level the Lifshitz transition is crossed and the Fermi surface is holelike.

A numerical study [99] confirms this view. This work analyzes the sign reversal of the Hall effect in TaS₂ and NbS₂ below a certain temperature. These materials combine the appearance of a pseudogap with a Lifshitz transition.

3.2 Results

This section concerns the magnetotransport results shown in Fig. 37. The interpretation of these results, and their connection to the pseudogap in cuprates will be discussed in section 3.3. The Gd-intercalated graphene samples were transferred into a He-4 or dilution refrigerator without oxygen contamination, where they were cooled down to 20 mK. After the measurements, the samples were brought back to the ARPES chamber, where the doping level was confirmed to be unchanged.

The resistivity versus temperature of intercalated graphene is shown in Fig. 37a. Despite its high carrier density, graphene at the VHS behaves as an insulator, becoming more resistive at low temperature. The inset shows the same data on a $\log \rho$ versus $1/T$ scale, creating an Arrhenius plot. The activation energy Δ can be extracted from

$$\log \rho \propto \frac{\Delta}{T}. \quad (72)$$

Two activation energies $\Delta_1 = 200$ K at high temperature and $\Delta_2 = 3$ K at low temperature can be found.

Panel 37b shows the Hall coefficient R_H as a function of temperature, and gives some information about the charge carrier density. At high temperature, the Hall coefficient is small and positive. It does not depend

on temperature. Below a characteristic temperature $T^* \approx 110$ K, indicated by the arrow, this changes into a large, negative and temperature-dependent Hall coefficient. The black lines are guides for the eye.

Panels c, d and e concern magnetoresistance. Unusually for graphene, the resistance *decreases* when a magnetic field is applied, visible in panel c. This negative magnetoresistance is stronger at lower temperatures, and disappears at large enough temperature.

A polynomial relation between resistance and magnetic field, $R \propto B^n$, holds at large fields, shown in the log-log plot by the straight lines. The exponent n gives an indication how strong the negative magnetoresistance is. Panel e shows $n(T)$. The large, negative exponent at low temperature shows the strong negative magnetoresistance. Above a temperature $T^* \approx 110$ K, n approaches zero and the magnetoresistance vanishes.

3.3 Discussion

The characteristic temperature $T^* \approx 110$ K appears in two experiments. We summarize:

- When considering the Hall coefficient, T^* is the temperature that divides the small, positive, temperature independent Hall coefficient at high temperature with the regime at low T , where R_H is large, negative and strongly temperature dependent (Fig. 37b).
- Below T^* , negative magnetoresistance is present (Fig. 37e).

The combination of these measurements at the same temperature scale leads us to assert that below T^* a *pseudogap* opens in graphene at the VHS, combined with a Lifshitz transition.

The temperature-induced Lifshitz transition is apparent from Fig. 37b, where the Hall coefficient switches sign at T^* . This can be understood as a rearrangement of the Fermi surface. Above T^* , the Fermi surface is a large pocket around Γ with holelike carriers, visible in Fig. 29 and consistent with a small, positive and temperature-independent Hall coefficient. When the temperature is lowered below T^* , the Fermi surface rearranges into small pockets around K, K' with electronlike carriers, resulting in a large and negative Hall coefficient. This Fermi surface transformation is sketched in Fig. 38

The lower panel of Fig. 39 compares the behaviour of Hall coefficients. For both cuprates and graphene, the pseudogap temperature T^* separates

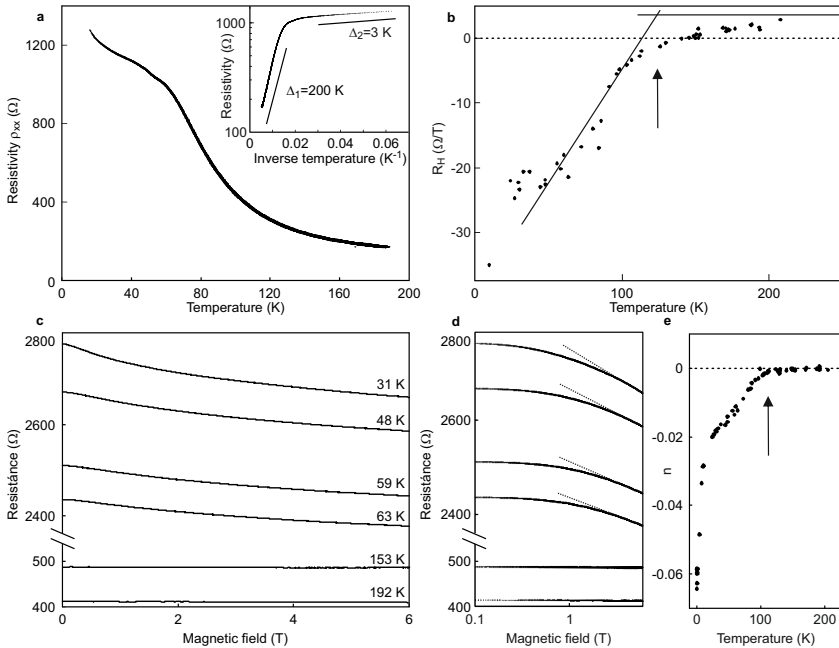


Figure 37: Magnetotransport in graphene at the VHS. (a) Resistivity versus temperature shows the insulating behaviour. Inset: Arrhenius plot shows the activation energies Δ_1 and Δ_2 . (b) Hall coefficient R_H versus temperature. It evolves from small and positive at high temperature to large and negative at low temperature. (c) Resistance versus magnetic field at selected temperatures. Note the negative magnetoresistance. Magnetic field points out of the plane. (d) Data of (c), but on a log-log scale, showing the polynomial fit at high field. (e) Field exponent n versus temperature, described in the text.

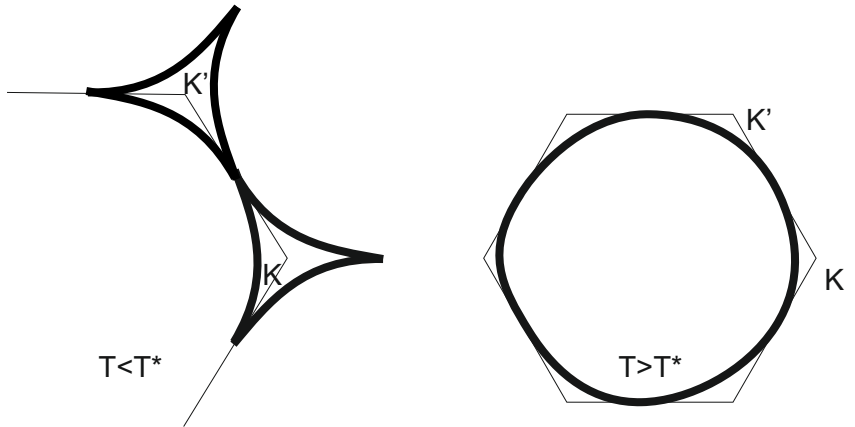


Figure 38: Sketch of the Fermi surface transformation. Left: a Fermi surface consisting of pockets around K and K' with electronlike carriers. Right: a large Fermi surface around Γ with holelike carriers. This transformation is believed to occur at T^* in highly doped graphene.

the temperature-independent regime at high T with the temperature-dependent behaviour at low T . A universal rescaled $R_H(T)$ curve has been observed in cuprates [94], described by Eq. 71. When rescaling the data of Fig. 37b (black dots, with parameters $R_H^\infty = 4\Omega/T$ and $R_H^* = -40\Omega/T$), there is a great similarity with the curve of the pseudogapped cuprates (green line).

The insulating behaviour of Fig. 37a can be understood to reflect the evolution of a pseudogap: as the DOS around the chemical potential is depleted, the conductivity decreases [89]. The activation energies $\Delta_{1,2}$ must then be an indication of the width of the pseudogap.

The pseudogap is also responsible for the negative magnetoresistance seen in Fig. 37c. An external magnetic field destroys the pseudogap, restoring the conductivity of the ungapped state [93, 89, 91]. The same polynomial dependence $\rho \propto B^n$ (Fig. 37d) is present in the pseudogapped cuprates [89], leading to the same analysis as in Fig. 37e with a transition between $n < 0$ and $n = 0$.

The similarity is even more striking when comparing directly with magnetotransport data of pseudogapped cuprates, shown in the top panel of Fig. 39. The negative MR of Fig. 37c is compared with data [89] from

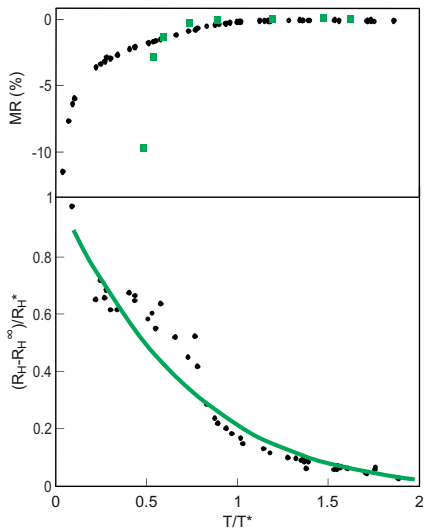


Figure 39: Comparison of magnetotransport data with selected cuprates. Top: negative magnetoresistance (expressed in %) appears below T^* for both intercalated graphene (black dots) and overdoped BSCCO [89] (green squares) with $T_c = 78$ K and $T^* = 110$ K. MR calculated at 3 T for graphene, at 31.2 T for BSCCO. Bottom: the Hall coefficient for graphene at the VHS (black dots), rescaled according to Eq. 71. The universal behaviour for cuprates [94] is shown in green.

BSCCO. For both materials, there is no magnetoresistance at high temperatures. Below the pseudogap temperature T^* , negative magnetoresistance appears, and quickly increases in magnitude. BSCCO becomes superconducting at 78 K and no longer displays magnetoresistance. Note that the negative MR in graphene is stronger than in BSCCO: MR was calculated at 3 T for graphene, compared with 31.2 T for BSCCO. Furthermore, the polynomial dependence $\rho \propto B^n$ has been seen in pseudogapped cuprates as well [89].

Negative magnetoresistance is generally a rare occurrence in metals. The resistivity of conventional metals scales quadratically with magnetic field. Other than the destruction of a pseudogap, as mentioned above, weak localization is a possible mechanism. In this effect, the phase coherence length of the charge carrier is of the same order of magnitude as

the scatters in the crystal. In this case, loops between several scatterers can interfere constructively [100], “localizing” the carrier and increasing the resistance at $B = 0$.

An out-of-plane magnetic field adds a phase to the trajectory of the charge carriers and quickly destroys the effect. The dependence of the conductivity change on out-of-plane magnetic field B is given by [101]:

$$\Delta\sigma(B) = \sigma(B) - \sigma(0) = \frac{e^2}{\pi h} \cdot \left(\ln \frac{B}{B_\phi} + \psi \left(\frac{1}{2} + \frac{B_\phi}{B} \right) \right), \quad (73)$$

where $B_\phi = \frac{\hbar}{4e l_\phi^2}$, l_ϕ is the phase coherence length and ψ is the digamma function. In more complicated systems with multiple scattering lengths (intra- and inter-valley scattering, trigonal warping, spin-orbit coupling), Eq. 73 must be expanded [102].

However, the weak localization scenario is unlikely in graphene at the VHS. In Fig. 40, the negative MR can be seen to not change much as the magnetic field is rotated into the plane. Weak localization only depends on the perpendicular component of the magnetic field [103], and can be excluded as a cause.

To further exclude weak localization, the right panel of Fig. 40 shows a fit to Eq. 73 (black line). It yields a parameter $B_\phi = 2 \cdot 10^{-11} \text{T}$, which corresponds to a phase coherence length $l_\phi = 7.2 \text{ nm}$. This is clearly unphysical. For reference, a typical weak localization feature is a few tens of mT wide, with a phase coherence length on the order of 100 nm [103].

Another candidate is the Altshuler-Aronov contribution to the DOS [104]. This effect describes the depletion of the DOS at the Fermi energy by electron-electron interactions. In magnetotransport, however, this results in a peculiar quadratic negative MR [105, 106], which is not observed in this study.

A temperature-induced Lifshitz transition has recently been observed [107, 108, 109] in WTe_2 and ZrTe_5 . These semimetals have electron and hole pockets close to the Fermi energy, separated by small (less than 10 meV) gaps. The bands around E_F are found to shift downwards when the temperature is lowered. The materials evolve from a p -type metal, to a small-gap semiconductor, to an n -type metal. At the same time, the Hall effect and thermopower change signs [107]. The mechanism for this shift is still unknown. A similar scenario is hard to imagine for graphene

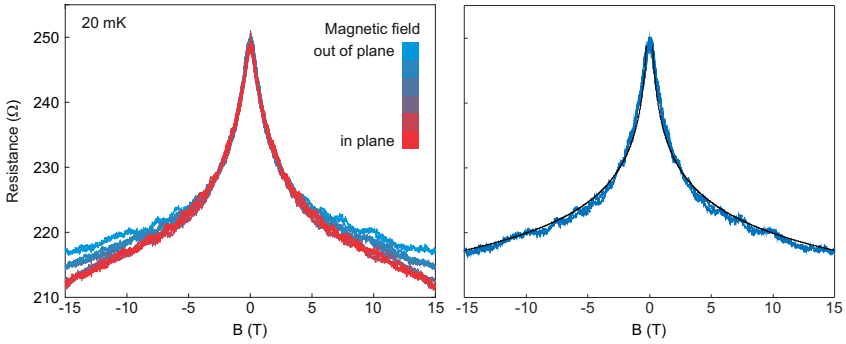


Figure 40: Magnetoresistance of graphene at the VHS at 20 mK, at multiple orientations of the magnetic field.

at the VHS: the bands would have to shift to a very large extent to reproduce the change in Hall coefficient seen in Fig. 37b. Furthermore, a maximum in resistivity [107] accompanying the transition in ZrTe_5 is not observed.

3.4 Outlook

The pseudogap and Lifshitz transition model describes the behaviour around T^* well. However, there are more features at lower temperature that merit closer attention.

For example, a second activation energy Δ_2 is visible in Fig. 37a below approximately 50 K. Another unexpected feature occurs in Fig. 37e, where n suddenly becomes smaller below 20 K. This might point to a “fully-formed” pseudogap that no longer evolves with decreasing temperature.

More direct probes would be very useful to study graphene at the VHS further. The most obvious choice would be ARPES at low temperatures, which could map out the low temperature Fermi surface, and measure the evolution of the DOS directly. The pseudogap temperature T^* , seen in multiple transport experiments, should have a direct counterpart in ARPES measurements.

Finally, we consider the role of the Gd intercalant. Gadolinium is strongly magnetic [110], with a spin $S = 7/2$. Is it possible an underlying superconducting state at the VHS is destroyed by the local magnetic moments of the intercalant? One avenue would be to try to achieve a similarly high carrier density with a nonmagnetic dopant. The ground state of graphene at the VHS might then be uncovered.

4 Viscous rectification in a graphene Tesla valve

The second experimental chapter concerns electron hydrodynamics in a graphene Tesla valve. First, we will discuss the Tesla valve geometry and its operation. Afterwards, some transistor models will be developed that will aid the interpretation of the results in section 4.3.

4.1 Principles of operation

Nikola Tesla patented in 1920 a model for a one-way valve without moving parts [111]. The device is an attempt to overcome the shortcomings of the one-way valves of his time.

As a rule the valve is a delicate contrivance, very liable to wear and get out of order and thereby imperil ponderous, complex and costly mechanism and, moreover, it fails to meet the requirements when the impulses are extremely sudden or rapid in succession and the fluid is highly heated or corrosive. [111]

Instead of a movable obstruction, the “Tesla valve”, shown in Fig. 41, relies on the properties of the fluid itself to rectify the flow. When flowing from left to right in Tesla’s diagram, the flow is split up in two channels. One of the channels is redirected and will hit the other under an angle. At this point, the two streams hit each other with opposite velocities and some energy will be lost.

In the case the fluid is injected from the other side, this does not happen. The fluid, going from right to left, will mostly stay in the main channel and flow without obstacles. Even if there is a part of the stream going in the loop, it will hit the main flow at a shallow angle and not much energy will be dissipated.

The fluid will only undergo extra dissipation in one direction, making the device a leaky one-way valve. Especially in pulsed flow, the ratio between flow directions can be high, as the mechanism for rectification works instantly, compared with the slow reaction of movable shutters in a regular one-way valve.

The mechanism is indicated in Fig. 42. This simulation was performed for a system with a small Reynolds number, allowing the fluid motion to be modelled by the Stokes equation [112, 37]. The low Reynolds

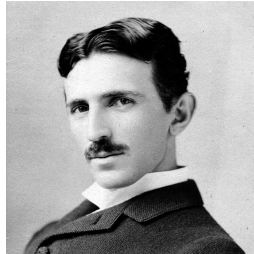
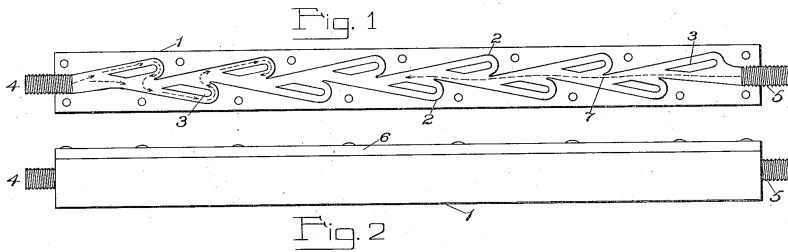


Figure 41: The Tesla valve as conceived in 1920 [111]. The path a fluid follows through the device is very different for both directions (shown with arrows). The direction-dependent flow resistance makes the Tesla valve a one-way valve without moving parts.

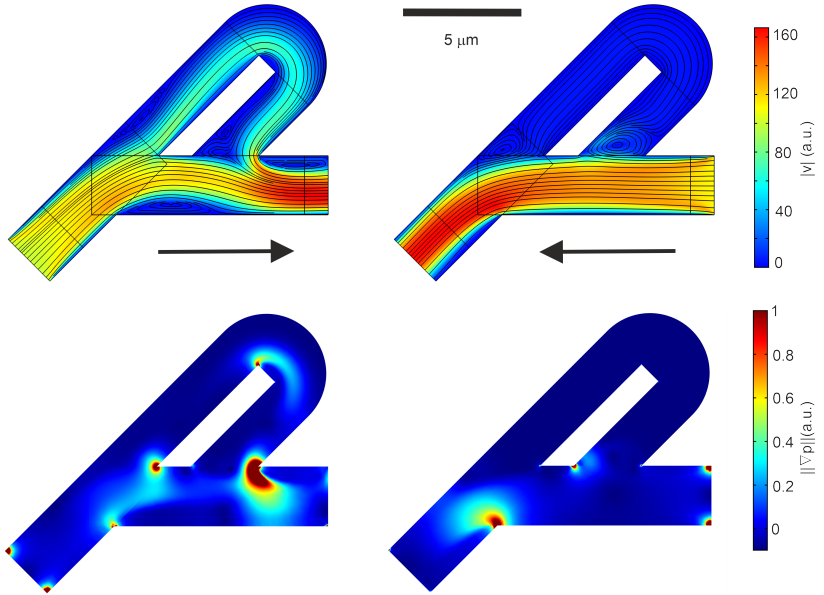


Figure 42: Flow velocity and pressure loss profiles for a Tesla valve. The top panels show the magnitude of the velocity of the fluid, going through the valve in the direction indicated by the arrow. Streamlines are shown as solid black lines. The bottom two panels show the corresponding loss of pressure. The scale bar indicates the size of the valve. COMSOL simulation parameters were $\eta = 1\mu Pa \cdot s$, $\rho = 1kg/m^3$ and $v_{av} = 100m/s$.

number limit is valid for viscous electron flow [112, 36, 113] where the fluid is very viscous and the device size small.

The top left panel shows the velocity field when the fluid goes through the valve in the “difficult” direction. The fluid that goes through the loop and hits the main flow is clearly visible. Streamlines are added as solid black lines. Note that the recombination of flows pushes the streamlines of the main flow downwards, towards the wall. The streamlines that went through the loop are also compressed when the flow is suddenly redirected as it hits the main flow.

It is this compression of streamlines that will cause enhanced dissipation in this flow direction. In a viscous fluid, more momentum is

leaked to the environment as the velocity increases (Eq. 61). This is visible in the bottom left panel of Fig. 42), where the change in pressure $\nabla P = \frac{\partial P}{\partial x} + \frac{\partial P}{\partial y}$ is shown. Apart from sharp corners, most of the pressure loss happens in the region of streamline rearrangement, visible as the red area.

In the easy direction of flow, shown in the top right panel, very little current flows through the loop, causing no pressure loss (bottom right panel). This is the asymmetry that drives the Tesla valve.

The whirlpools in the top panels are caused by fluid flowing past an opening, in close analogy to the whirlpools in [37]. The whirlpools dissipate energy, but the low velocity of the fluid in that area makes this dissipation negligible (bottom panels).

Earlier studies of mechanical Tesla valves corroborate the mechanism as “*viscous dissipation surrounding laminar jets that have flow-direction-dependent locations and orientations*” [114]. In the case of higher Reynolds number flows, the full Navier-Stokes must be applied, which makes the solution and interpretation far more complicated [114].

In the rest of this chapter, we will present a Tesla valve that works with *electrons*. As seen in section 1.3, it is possible for electrons to behave like a hydrodynamical fluid. Experimentally, this means the phenomena we associate with hydrodynamics can now be seen in electron fluids. Realizing a Tesla valve for electrons is a new way to measure the viscosity of electron fluids.

4.2 Transistors

In this section we will derive relations between the current, bias and gate voltage for a transistor. This will be very useful when interpreting Tesla valve results.

4.2.1 Transistor equation

We consider a two-terminal transistor. Current flows from the source at electrochemical potential V_S to the drain, which is grounded ($V_D = 0$). This channel is capacitively coupled to a backgate, which allows to control the carrier density in the channel by applying a voltage between the gate and drain. The *local* carrier density at a point x along the channel is then

$$n(x) = C \cdot (V_G - V(x)) \quad (74)$$

where $C = \frac{\epsilon\epsilon_0}{t}$ is capacitance of a backgate of thickness t with dielectric constant ϵ . This is the local corollary of Eq. 66. At a nonzero source-drain bias, this means the carrier density is not constant along the channel. We can determine the current through the transistor by starting from the current continuity equation, stating that the current I through any segment of the channel is constant.

$$I = W \cdot (-e)n(x) \cdot v(x) \quad (75)$$

$$I = W \cdot (-e)C(V_G - V(x)) \cdot \mu E \quad (76)$$

$$I = -WeC(V_G - V(x))\mu \frac{dV}{dx} \quad (77)$$

This expression can be integrated from the source to the drain.

$$\int_S^D Idx = \int_S^D -WeC\mu(V_G - V)dV \quad (78)$$

$$I \cdot L = -WeC\mu \int_S^D V_G dV - \int_S^D V dV \quad (79)$$

$$\frac{IL}{Ce\mu W} = -V_G \Big|_{V(S)=V_S}^{V(D)=0} + \frac{V^2}{2} \Big|_{V(S)=V_S}^{V(D)=0} \quad (80)$$

$$\frac{IL}{Ce\mu W} = V_G \cdot V_S - \frac{V_S^2}{2} \quad (81)$$

When $V_S \ll V_G$, the current depends linearly on the bias voltage. If V_S becomes comparable to V_G , the carrier density in the channel is greatly changed by the bias voltage and $I_{DS}(V_{DS})$ is no longer linear. To quantify this nonlinearity, we will use the diodicity D , the ratio between the resistances in both current directions (Eq. 125). Denoting the case where the current flows from source to drain as “forwards” (f), and in the other direction, “backwards” (b):

$$D = \frac{V_f/I_f}{V_b/I_b} \quad (82)$$

$$= \frac{V_S(V_G - V_S/2)}{I} \cdot \frac{-I}{-V_S(V_G + V_S/2)} \quad (83)$$

$$= \frac{V_G - V_S/2}{V_G + V_S/2} \quad (84)$$

$$D = 1 - \frac{V_S/2}{V_G + V_S/2}. \quad (85)$$

In general, at constant V_S , the scaling relation $D - 1 \propto 1/V_G$ will mostly hold in the following models. Recalling the description of electrostatic gating in Eq. 66, this can also be described as $D - 1 \propto 1/n$. Note that there is no explicit temperature dependence. The $1/n$ -dependence and absence of temperature dependence are hallmarks of diodicity caused by bias-induced carrier depletion.

4.2.2 Graphene transistor with electron-hole puddles

When considering the effect of electron-hole puddles [52, 51], the effect of a backgate is given by Eq. 65:

$$n^2(x) = n_0^2 + C^2 \cdot (V_G - V_0 - V(x))^2. \quad (86)$$

The gate voltage V_G does not change the carrier density n close to the charge neutrality point, where the carrier density is at least n_0 . Proceeding with the current continuity equation 76, we obtain:

$$I = W \cdot (-e)n(x) \cdot v(x) \quad (87)$$

$$I = -W \cdot \sqrt{n_0^2 + C^2(V_G - V_0 - V(x))^2} \cdot e\mu \frac{dV}{dx}. \quad (88)$$

Integrating this expression from source to drain yields:

$$\int_S^D I \cdot dx = -We\mu \int_S^D \sqrt{n_0^2 + C^2(V_G - V_0 - V(x))^2} \cdot dV \quad (89)$$

$$I \cdot L = -We\mu \int_S^D \sqrt{n_0^2 + C^2(V_G - V_0 - V(x))^2} \cdot dV \quad (90)$$

$$\frac{IL}{CWe\mu} = - \int_S^D \sqrt{(V_G - V_0 - V(x))^2 + \frac{n_0^2}{C^2}} \cdot dV. \quad (91)$$

Substituting $X = V(x) - V_G + V_0$, $Y^2 = \frac{n_0^2}{C^2}$ and therefore $dX = dV$:

$$\frac{IL}{CWe\mu} = - \int_S^D \sqrt{X^2 + Y^2} \cdot dX \quad (92)$$

$$= -\frac{1}{2}X\sqrt{X^2 + Y^2} - \frac{Y^2}{2} \log\left(\sqrt{X^2 + Y^2} + X\right) \Big|_S^D \quad (93)$$

$$= -\frac{V(x) - V_G + V_0}{2} \sqrt{(V(x) - V_G + V_0)^2 + \frac{n_0^2}{C^2}} \Big|_{V(S)=V_S}^{V(D)=0} \quad (94)$$

$$- \frac{n_0^2}{2C^2} \log\left(\sqrt{(V(x) - V_G + V_0)^2 + \frac{n_0^2}{C^2}} + V(x) - V_G + V_0\right) \Big|_{V(S)=V_S}^{V(D)=0}. \quad (95)$$

So that finally we obtain:

$$\begin{aligned}
\frac{IL}{CWe\mu} &= \frac{V_G - V_0}{2} \sqrt{(-V_G + V_0)^2 + \frac{n_0^2}{C^2}} \\
&\quad - \frac{n_0^2}{2C^2} \log \left(\sqrt{(-V_G + V_0)^2 + \frac{n_0^2}{C^2}} - V_G + V_0 \right) \\
&\quad + \frac{V_S - V_G + V_0}{2} \sqrt{(V_S - V_G + V_0)^2 + \frac{n_0^2}{C^2}} \\
&\quad + \frac{n_0^2}{2C^2} \log \left(\sqrt{(V_S - V_G + V_0)^2 + \frac{n_0^2}{C^2}} + V_S - V_G + V_0 \right).
\end{aligned} \tag{96}$$

Note that Eq. 96 reduces to the usual transistor equation when $n_0 = 0$ and the regular gating relation $n = C \cdot V_G$ is recovered:

$$\begin{aligned}
\frac{IL}{CWe\mu} &= \frac{(V_G - V_0)^2}{2} - \frac{(V_S - V_G + V_0)^2}{2} \\
&= \frac{1}{2} ((V_G - V_0)^2 - V_S^2 - (V_G - V_0)^2 + 2V_S(V_G - V_0)) \\
&= V_S(V_G - V_0) - \frac{V_S^2}{2}.
\end{aligned}$$

Eq. 96 models the full behaviour of a graphene transistor at any bias voltage. An example is given in Fig. 43a. At small V_S , the complete channel is filled with n-type charge carriers and current increases linearly. At $V_S \approx V_G$, here at 1 V, the channel is depleted at the drain. There is a highly resistive region of the channel with electron-hole puddles that cause the current to saturate. This is the last area the conventional formula (Eq. 81) can describe. When the bias is increased further, and $V_S > V_G$, holes will accumulate at the drain and there is a p-n junction in the channel. Current through the channel can increase again. Note that graphene has no bandgap and carriers will radiationlessly recombine at the p-n junction. Similar curves have been obtained in [51].

The diodicity in the impurity model is shown in Fig. 43b. It is more rounded than the naive two-terminal model, and describes diodicity down to $n = 0$, where the two-terminal model fails. Note that the diodicity predicted by the impurity model is always lower than the naive prediction, since the impurity density n_0 is a “minimal” carrier density that cannot

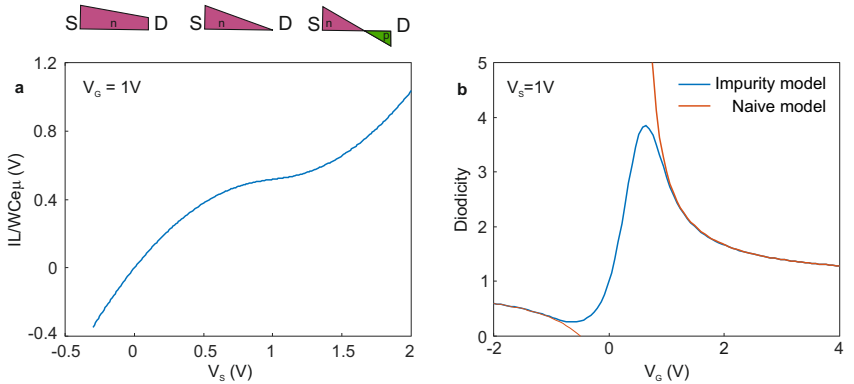


Figure 43: (a) An example of a current-voltage characteristic for a graphene transistor with electron-hole puddles, according to Eq. 97. $V_G = 1V$ and $n_0/C = 0.1V$. Three regions are indicated by the schematic and discussed in the main text. (b) Diodicity for the two-terminal (Eq. 81) and impurity (Eq. 97) model.

be depleted further. Every area of the transistor then has a minimal conductivity set by n_0 .

4.2.3 Transistor with four terminals

Consider a transistor with two internal contacts, 1 and 2, between the source S and drain D , depicted in Fig. 44. This situation is different from the regular transistor model, since the gating potential between the channel (1 to 2) and the backgate is reduced by the potential drop between contact 2 and the drain.

A full derivation of $V_1 - V_2$ goes as follows. In order to obtain an analytical result, we assume $n = C \cdot V$, ignoring the effect of electron-hole puddles described in the previous section. In general, the current between two points a and b is



Figure 44: Sketch of a transistor with four terminals. The internal contacts 1 and 2 lie between the source S and drain D . All share the same gate G .

$$I = W \cdot (-e)n(x) \cdot v(x) \quad (97)$$

$$I = -W \cdot C(V_G - V(x)) \cdot e\mu \frac{dV}{dx} \quad (98)$$

$$\frac{I}{WCe\mu} dx = -(V_G - V(x)) \cdot dV \quad (99)$$

$$\frac{I}{WCe\mu} \int_a^b dx = - \int_a^b V_G dV + \int_a^b V dV \quad (100)$$

$$\frac{IL_{ab}}{WCe\mu} = -V_G \cdot V \Big|_a^b + \frac{V^2}{2} \Big|_a^b \quad (101)$$

$$\frac{IL_{ab}}{WCe\mu} = -V_G(V_b - V_a) + \left(\frac{V_b^2}{2} - \frac{V_a^2}{2} \right). \quad (102)$$

This general relation reduces to the transistor equation if $L_{ab} = L_{SD}$, $V_a = V_S$ and $V_b = 0$. For the four-terminal case, we obtain

$$I_{12} = -Ce\mu \left(\frac{W}{L} \right)_{12} \left(V_G(V_2 - V_1) - \left(\frac{V_2^2}{2} - \frac{V_1^2}{2} \right) \right) \quad (103)$$

$$I_{2d} = -Ce\mu \left(\frac{W}{L} \right)_{2d} \left(V_G(V_d - V_2) - \left(\frac{V_d^2}{2} - \frac{V_2^2}{2} \right) \right). \quad (104)$$

Given $I = I_{12} = I_{2d}$, $V_d = 0$, we wish to find $V_1 - V_2$ in terms of I . We adopt the notation $C_{12} = Ce\mu \left(\frac{W}{L} \right)_{12}$ and $C_{2d} = Ce\mu \left(\frac{W}{L} \right)_{2d}$. Eq. 104 becomes:

$$-I = -C_{2d}V_GV_2 + C_{2d}\frac{V_2^2}{2} \quad (105)$$

$$0 = \frac{C_{2d}}{2}V_2^2 - C_{2d}V_G \cdot V_2 + I \quad (106)$$

$$V_2 = \frac{C_{2d}V_G \pm \sqrt{V_G^2C_{2d}^2 - 2IC_{2d}}}{C_{2d}}. \quad (107)$$

We take the solution with negative sign so $V_2 = 0$ when $I = 0$ and $V_G > 0$:

$$V_2 = V_G - \sqrt{V_G^2 - \frac{2I}{C_{2d}}}. \quad (108)$$

Similarly, Eq. 103 becomes:

$$-I = C_{12} \left(V_G(V_2 - V_1) - \frac{V_2^2}{2} + \frac{V_1^2}{2} \right) \quad (109)$$

$$-2I = 2C_{12}V_GV_2 - 2C_{12}V_GV_1 - C_{12}V_2^2 + C_{12}V_1^2 \quad (110)$$

$$0 = C_{12} \cdot V_1^2 + (-2C_{12}V_G) \cdot V_1 + (2C_{12}V_GV_2 + 2I - C_{12}V_2^2) \quad (111)$$

$$V_1 = \frac{2C_{12}V_G \pm \sqrt{D}}{2C_{12}} \text{ with } D = 4C_{12}^2V_G^2 - 8C_{12}^2V_GV_2 - 8C_{12}I + 4C_{12}^2V_2^2. \quad (112)$$

Again, we take the solution with negative sign so $V_1 = V_2$ when $I = 0$.

$$V_1 = V_G - \sqrt{V_G^2 - 2V_2V_G - \frac{2I}{C_{12}} + V_2^2} \quad (113)$$

$$V_1 = V_G - \sqrt{(V_G - V_2)^2 - \frac{2I}{C_{12}}} \quad (114)$$

We rewrite Eq. 108 as $(V_G - V_2)^2 = V_G^2 - \frac{2I}{C_{2d}}$ and substitute it in Eq. 114.

$$V_1 = V_G - \sqrt{V_G^2 - \frac{2I}{C_{2d}} - \frac{2I}{C_{12}}} \quad (115)$$

Finally, we can combine Eqs. 108 and 115 to obtain an expression for $\Delta V = V_1 - V_2$ as a function of I .

$$\Delta V = \sqrt{V_G^2 - \frac{2I}{C_{2d}}} - \sqrt{V_G^2 - \frac{2I}{C_{2d}} - \frac{2I}{C_{12}}} \quad (116)$$

This equation shows how the applied gate voltage V_G is reduced by a term $\frac{2I}{C_{2d}}$ when there is an extra channel between contact 2 and the drain. It reduces to the regular expression (Eq. 108) when the extra channel is zero. We can introduce a *shape factor*

$$\square_{2d} = \frac{(W/L)_{12}}{(W/L)_{2d}}. \quad (117)$$

It is a purely geometric constant that expresses how many more squares there are between contacts 2 and the drain than between contact 1 and 2. This is especially convenient since we are working with a two-dimensional material and resistivity is expressed per square. Therefore

$$C_{12} = \square_{2d} \cdot C_{2d} \quad (118)$$

and we rewrite Eq. 116 as

$$\Delta V = \sqrt{V_G^2 - \square_{2d} \frac{2I}{C_{12}}} - \sqrt{V_G^2 - (\square_{2d} + 1) \frac{2I}{C_{12}}}. \quad (119)$$

This equation reduces to the ideal two-terminal case (Eq. 108) when $\square_{2d} = 0$, the case where the second voltage probe is the drain. It can be immediately adapted into a calculation of the diodicity at a given current:

$$D = - \frac{\Delta V(I)}{\Delta V(-I)}. \quad (120)$$

An example of Eq. 116 is given in Fig. 45. In red, the current-voltage characteristic for a regular, two-terminal transistor according to Eq. 81 is shown. In red, the $I(V)$ sweep for a transistor with an extra piece of channel between contact 2 and the drain. Note there is a change in current, and the $I(V)$ characteristic is more curved. Hence the diodicity is larger.

4.3 Results

Two sets of results will be presented in this section. First, a Tesla valve out of monolayer graphene, named Device 1. The rectification observed in this device, present at particular carrier densities and temperatures,

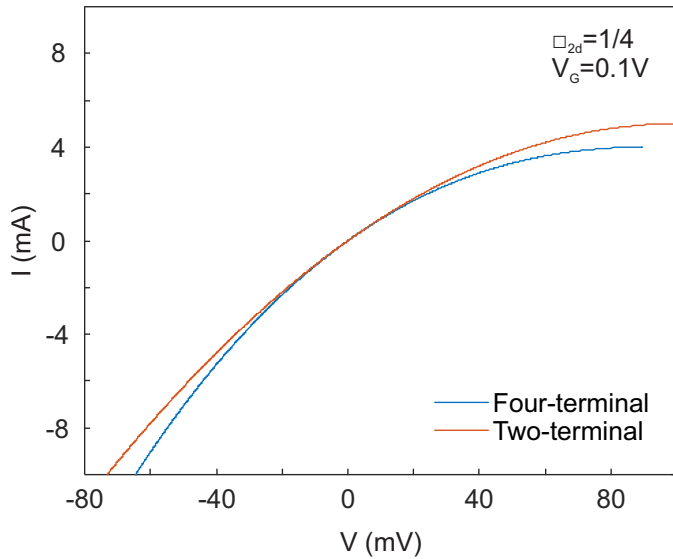


Figure 45: Current-voltage sweeps for transistors with two contacts (red, Eq. 81) and four contacts (blue, Eq. 119). For these sweeps, $V_G = 0.1V$ and $\square_{2d} = 1/4$, meaning there are four times as many squares between contacts 1 and 2 as between contact 2 and the drain. The voltage drop between contact 2 and the drain cause a shift in the effective gating voltage between contact 1 and 2. This results in a decrease in current at positive bias, and an increase in current for negative bias.

will be discussed. Afterwards, we will discuss a Tesla valve made out of monolayer graphene with a Moiré superlattice, created by the hBN encapsulation, named Device 2. These results exhibit additional features due to the superlattice, and will elucidate observations in the Device 1.

4.3.1 An electronic viscous diode

Device 1 is presented in Fig. 46. The complete van der Waals stack, directly after completion, is shown in panel a. It rests on a SiO_2 substrate, visible in purple. Directly on top of the substrate, the first layer is a graphite flake (grey flake in the vertical direction). On top of this, there is a large hBN flake (yellow). The layer of graphene (invisible) is encapsulated below another hBN flake (orange, horizontal direction). Full details on van der Waals stacks and lithography are provided in section 2.1.

Panel c shows the etched stack. A square has been patterned and contacts are made to the graphene and graphite backgate. An AFM scan of this square is shown in panel b, together with the height profile along the white line in panel d. The surface is very flat and free of contamination. The scale bars indicate the square is around $12 \mu\text{m}$ by $12 \mu\text{m}$.

Afterwards, this sample is patterned in a Tesla valve shape, shown in panel e. The square has been etched into the largest possible valve. The contacts on all sides of the square are now contacts at both sides of the valve. The AFM scan of the valve (panel f) shows the device is still flat, with a few impurities on the surface. In the image, contact AFM cleaning of the surface is partially complete, with impurity-free rectangles visible. Before the electrical measurements, the complete device was finished in this manner. The schematic of the applied bias and voltmeter shows the configuration of the electrical measurement: current is passed through the valve, and the voltage drop across is measured in the usual four-terminal setup. The graphite backgate (not shown) allows the control over the carrier density in the device.

Characterization With the device complete, we can characterize its basic properties and verify the processing did not destroy the high quality of the encapsulated graphene.

The encapsulated graphene is now capacitively connected to both the graphite gate and the silicon backgate. Note that the latter gate,

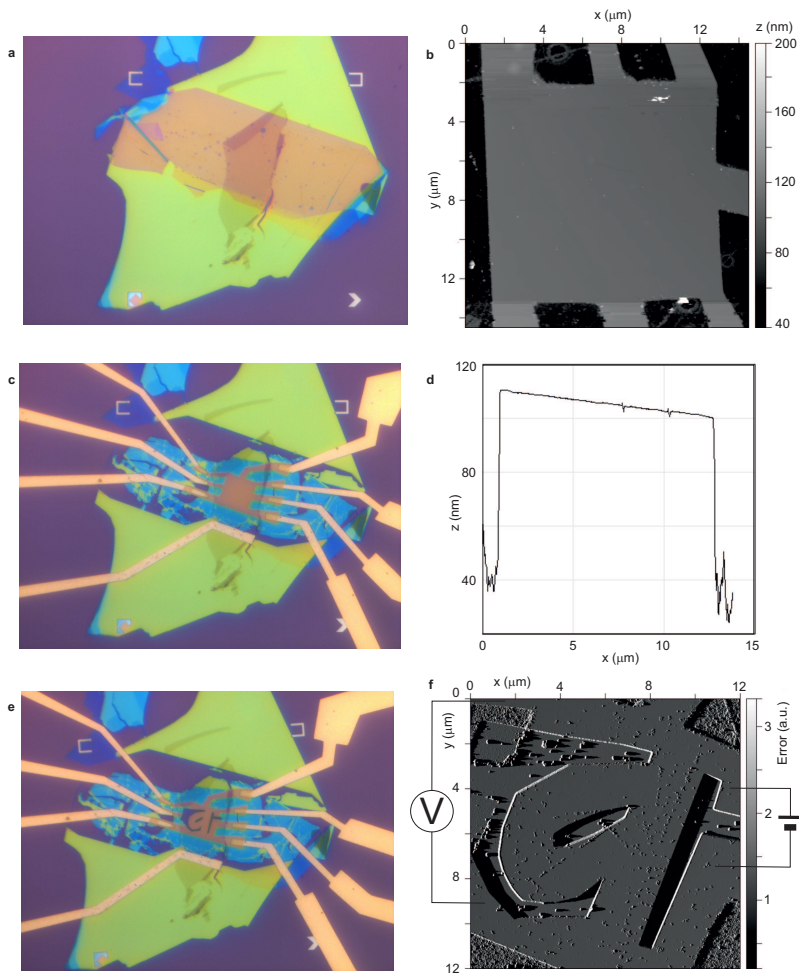


Figure 46: Device 1. (a) The van der Waals stack the device is made of. (b) The AFM scan of (c) a square etched out of the stack. Cr/Au contacts are visible at the edges. (d) The height profile of the line in panel b, showing the flatness of the square. (e) The Tesla valve etched out of the square in panel c. (f) An AFM scan of the Tesla valve, showing the cleaning process in progress (contamination-free rectangles in the scan). The measurement setup is shown.

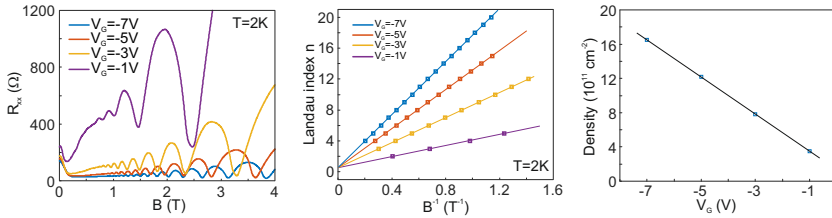


Figure 47: Determination of the carrier density through an analysis of Shubnikov-de Haas (SdH) oscillations. Left panel: longitudinal resistance of the valve versus perpendicular magnetic field at multiple gate voltages. The SdH oscillations are clearly visible at higher field. The middle panel shows the Landau index of an oscillation versus the inverse of the magnetic field at which it occurs. As indicated in the main text, this allows to extract the carrier density as a function of gate voltage in the right panel.

the silicon gate across the 300 nm of SiO₂ on which the sample rests, is kept at $V_S = -60V$ throughout all measurements. The parts of the graphene that are not gated by the graphite gate are therefore at a large carrier density. From Fig. 46e, we can see that these are mostly the parts connected to the metallic contacts. This ensures the contacts to the graphene are of good quality, with negligible contact resistance (10 Ω or less).

The graphite backgate allows to control the carrier density of the part of the encapsulated graphene we are interested in: the Tesla valve pattern. An analysis of the Shubnikov-de Haas (SdH) oscillations is shown in Fig. 47 and will allow us to extract the carrier density as a function of gate voltage.

The left panel of Fig. 47 shows the longitudinal resistance of the Tesla valve versus magnetic field. As the magnetic field increases, the oscillations are more visible.

We recall from section 1.2.11 that for monolayer graphene with n_{LL} Landau levels filled

$$n = 4(n_{LL} - \beta) \frac{eB_i}{h} \quad (121)$$

where n is the carrier density, β is the Berry phase and B_i is the magnetic field at which n_{LL} Landau levels are filled. The factor of 4

accounts for both spin and valley degeneracy. Then,

$$n_{LL} = \frac{nh}{4e} \cdot \frac{1}{B_i} + \beta. \quad (122)$$

The minima in longitudinal resistance are extracted from the left panel of Fig. 47 and assigned a Landau index. The Landau index of every minimum is plotted versus the inverse of the corresponding magnetic field in the middle panel (squares). The solid lines are the least-squares fits through these points, extended to infinite field ($B^{-1} = 0$). For each set of data, the intercept at infinite field is 0.54 ± 0.01 . This is a direct measurement of the Berry phase of monolayer graphene, and lies close to the theoretical prediction of 0.5. The slope of this line is $\frac{nh}{4e}$ (Eq. 122).

The rightmost panel of Fig. 47 shows the calculated carrier density versus gate voltage (blue squares). The induced charge depends linearly on the bias (solid line), as expected from a capacitor. The slope, the efficiency at which charge is induced, is a property of the medium between the graphene and graphite backgate, hexagonal boron nitride.

Recalling Eqs. 66 and 67, and with a specific permittivity of hBN $\epsilon_{hBN} = 3 - 4$ [57]:

$$C = \frac{d(en)}{dV} = 618 \frac{\mu F}{m^2}, \quad (123)$$

$$C = \frac{\epsilon\epsilon_0}{t}. \quad (124)$$

We can extract a dielectric thickness $t = \frac{\epsilon\epsilon_0}{C} = 76 - 102$ nm, which matches the real backgate thickness of approximately 80 nm. The total stack thickness measured by AFM (Fig. 46) is approximately 110 nm.

Inhomogeneity density At low carrier concentrations, the existence of electron - hole puddles (section 1.4) precludes reaching zero carrier density [47] and forms a lower limit to carrier density n_0 . As the charge neutrality point is approached, the resistivity of graphene will not grow arbitrarily high, but will approach a limit set by n_0 .

Fig. 48 shows the resistance of the Tesla valve at 300K versus gate voltage. The same data are shown on a log-log scale in the right panel as conductivity versus carrier density. Results for the electron and hole sides of the Dirac peak essentially overlap. The solid lines indicate the carrier density at which the conductivity saturates at small carrier densities.

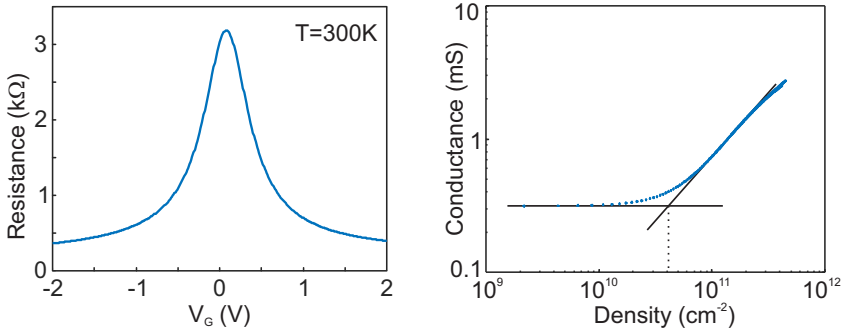


Figure 48: Left panel: four-terminal resistance versus gate voltage of the Tesla valve. Right panel: four-terminal conductivity versus carrier density on a logarithmic scale. This allows the extraction of the charge inhomogeneity: $n_0 \approx 4 \cdot 10^{10} cm^{-2}$.

This estimates the charge inhomogeneity $n_0 \approx 4 \cdot 10^{10} cm^{-2}$, matching other high-quality hBN-encapsulated graphene samples [32, 3].

Rectification in Device 1 After confirming the quality of the Tesla valve, we can now proceed to measuring the presence of any diodic behaviour. In reference to the past treatments of the Tesla valve for engineering fluids, we choose as figure of merit the *diodicity*

$$D = \frac{R_f}{R_b} = \frac{(V/I)_f}{(V/I)_b} \quad (125)$$

where the subscripts f and b refer to the forwards and backwards direction of the current. The diodicity is the ratio between forwards and backwards resistances. When $D = 1$, there is no rectification and the device is an Ohmic resistor. Deviations away from 1 signify rectifying behaviour. A discussion of the quality of Eq. 125 is given below, in section 4.4.1.

The results shown below are measured with constant current. For Device 1, $I_f = -I_b = 6.30 \mu A$. This choice stems from using a fixed-current setup. As an example, consider the I-V sweep in Fig. 49. For a given V_G and T , the values (V_f, I_f) and (V_b, I_b) are selected. If no measurement took place at exactly I_f , values are interpolated from neighbouring measurements. Forwards resistance $R_f = V_f/I_f = 297 \Omega$ and

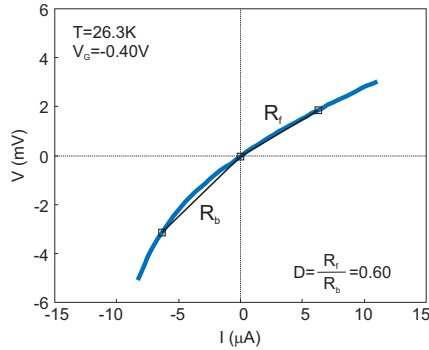


Figure 49: Example of a diodicity calculation. The plot shows voltage versus current for Device 1 at $V_G = -0.40\text{V}$ and $T = 26.3\text{K}$. The black line indicates how diodicity is calculated for this sweep: $R_f = 297\Omega$ and $R_b = 492\Omega$, therefore $D = \frac{R_f}{R_b} = 0.60$.

backwards resistance $R_b = V_b/I_b = 492\Omega$ are calculated, and therefore $D = R_f/R_b = 0.60$.

The viscous map A full characterization of the Tesla valve then involves mapping out diodicity for the (n, T) parameter space. For Device 1, density was varied between $n = -12.2 \cdot 10^{11} \text{cm}^{-2}$ and $n = 9.5 \cdot 10^{11} \text{cm}^{-2}$ ($V_G = -5\text{V}$ to $V_G = 5\text{V}$), and temperatures between 2 and 300K. In total, 2550 I-V characteristics were recorded.

The results are shown in Fig. 50. The top panel shows the full scale of the results. Most of the measurements show a diodicity of approximately unity, shown as the large orange areas. Around the CNP, however, there is a large excursion from $D = 1$, visible as the blue and red vertical bands.

The bottom panel shows the same results with a different colour scale. Small deviations from $D = 1$ are now visible, at the cost of saturating the rectification around the CNP. Now more details are visible, such as an area with $D > 1$, visible in green around 50 K and large hole densities.

We will discuss the different areas separately. First we will concentrate on the area around the CNP, where the diodicity is the largest. In this regime, the bias voltage is comparable in magnitude to the gate voltage and will influence the charge carrier density in graphene. This effect has been discussed and modelled in section 4.2. The result is plotted in Fig.

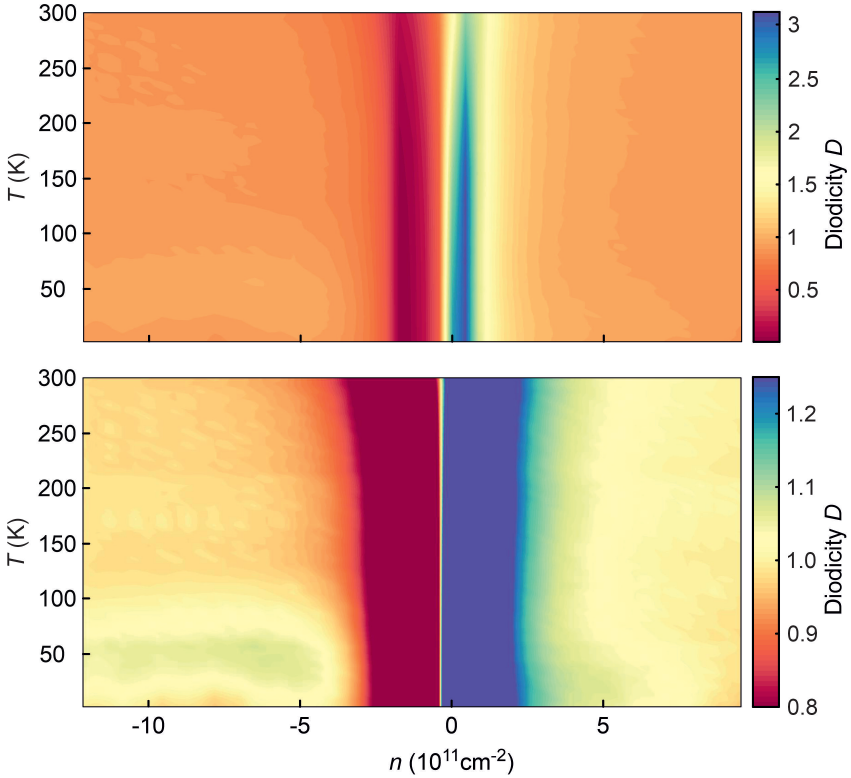


Figure 50: Diodicity versus temperature and carrier density for Device 1. The upper panel has a colour scale that spans the full extent of measured diodicity values. The lower panel shows the same results with a reduced span of the colour scale. Strong rectification occurs at low carrier density, as seen in the dark blue and red vertical bands. The large values at small n are now saturated, and smaller deviations from $D = 1$ are visible at higher n . Diodicity was calculated at $I_f = -I_b = 6.30\mu A$.

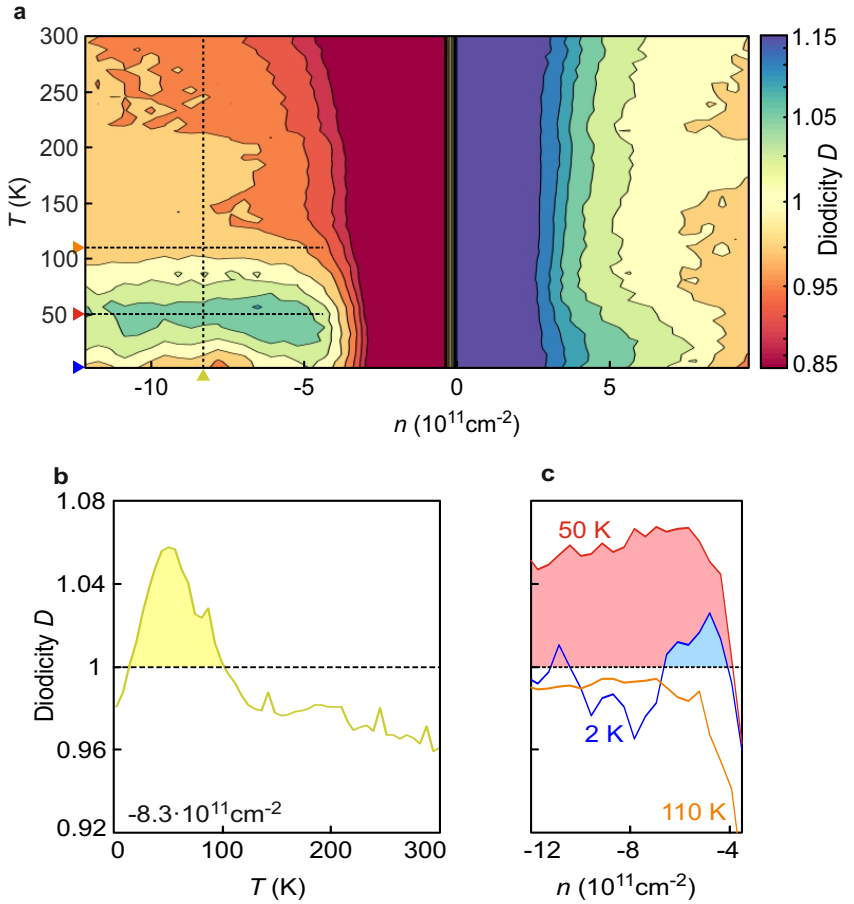


Figure 51: (a) Replotting the data of Fig. 50 as saturated colours shows the different areas of D more clearly. Panels (b) and (c) show cuts at constant density and temperature. The excess diodicity, attributed to viscous effects, is indicated by the shaded colours.

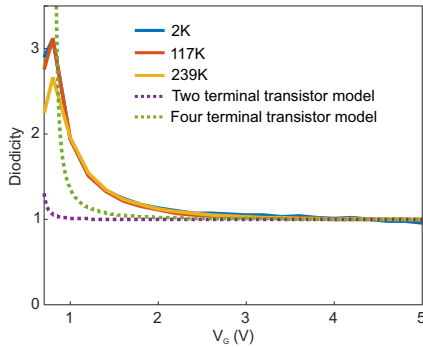


Figure 52: Bias-induced diodicity around the CNP in Device 1. The solid lines show the measured diodicity at different temperatures. The dashed lines are the two transistor-like models developed in section 4.2, Eqs. 81 and 119 for two-terminal and four-terminal transistors.

52. The solid lines show the diodicities measured in Fig. 50.

The purple dashed line shows the diodicity calculated for $I_f = 6.3\mu A$ according to Eq. 81. The green dashed line is the prediction for a four-terminal transistor (Eq. 119) with $\square_{2d} = 10$. This parameter represents the resistance between the second voltage probe and the drain, and is estimated from Fig. 46. This element of the four-terminal transistor will cause a large voltage drop close to the CNP, and therefore the gating potential will be changed. The increase in diodicity is visible as the purple line, and matches the measurements more closely.

The transistor model is successful in explaining the $D \sim 1/n$ dependence, and also clarifies why there is virtually no temperature dependence in the observations. The discrepancy in predicted magnitude, however, has no clear explanation and will be discussed further below, in section 4.3.2.

Let us now turn to the area away from the CNP, at high carrier density. For convenience, the data of Fig. 50 are shown as contours, in Fig. 51a. The bias-induced diodicity is visible as the strips around zero density. On the left side of the diagram, where the carriers are hole-like, there is an area around 50 K where the diodicity is larger than expected, visible in green. For these temperatures and carrier densities, the charge carriers behave as a viscous fluid and the Tesla valve works as described above.

The area of viscous rectification is bounded at high and low temperatures by areas where the diodicity goes back to unity. At high temperatures, this is the diffusive regime, where normal Ohmic behaviour is recovered. At low temperature, the electrons travel ballistically and do not interact with each other. As ballistic paths are time-reversal symmetric, there is no rectification in this regime. The temperature behaviour of rectification is shown in panel b of Fig. 51. The shaded area indicates the temperature range where diodicity is larger than expected.

Viscous rectification is also destroyed when the carrier density is decreased below approximately $4 \cdot 10^{11} \text{ cm}^{-2}$, as shown in panel b. At low (2 K) and high (111.5 K) temperature, the diodicity is close to unity. Only at intermediate temperature (50.6 K) there is a noticeable rectification. This is also visible in panel c.

The *direction* of rectification matches the geometry (Fig. 46) of the device. For carriers with positive charge, the carriers move in the same direction as the charge current. In this case, the “difficult” direction with increased losses is the “forward” direction, leading to a diodicity larger than unity.

The observations of viscous rectification at intermediate temperature and higher carrier density match the predictions of Fig. 18 for monolayer graphene, and the $R_V(n, T)$ map in Fig. 20, which maps a similar parameter space for the negative nonlocal resistance [37].

There is a curious lack of rectification on the electron side ($n > 0$) in Fig. 51, even though viscous effects should be equally strong. There is a small area at the lowest temperature and highest density where the diodicity dips below unity, but it is not as prominent as on the hole side. This lack of symmetry will be discussed further below, in section 4.4.4.

4.3.2 Superlattice effects in rectification

Now we turn to Device 2. The lattice mismatch between the graphene and the hBN encapsulating it creates a Moiré superlattice, resulting in secondary Dirac peaks as described in section 1.5. As an additional check, the diodicity of the same sample was measured before patterning, as a square.

Device composition Some stages in the fabrication of Device 2 are shown in Fig. 53. Again, the stack has four layers: a bottom graphite backgate, a hBN separator layer, monolayer graphene and a top hBN

capping layer. All four are visible in panel a. After patterning and contacting the area with no bubbles in the stack, the device has a square shape (panel b). After the measurements on this square sample (section 4.3.2), the device was patterned into the Tesla valve geometry (panel c). Panel d shows the AFM measurement of the device in panel c. After all these processing steps, it is still in a good condition, visible in the height profile in panel e.

Characterization The quantum Hall effect was used to determine the carrier density in the graphene. Fig. 54a shows the results. At low temperature and constant high magnetic field, the graphite gate was swept and the transversal resistance recorded. The plateaus in Hall resistance at filling factors 2 and 6 are indicated, together with a poorly developed filling factor 10. This sequence is typical for monolayer graphene, which is both spin and valley degenerate (section 1.2.12). The corresponding carrier densities of these quantum Hall states are shown in panel b. Using the Eqs. 66 and 67 for a capacitive gate and the permittivity for hBN, a backgate thickness between 43 and 57 nm can be extracted. This matches the 50 nm seen in AFM.

The sharp peak of longitudinal resistance at zero average carrier density is charge neutrality point, visible in panel c. In the log-log plot in panel d, an impurity density of approximately $3 \cdot 10^{10} \text{cm}^{-2}$ is extracted at the point the conductance no longer decreases with decreasing carrier density.

Comparison with a square device Device 2 was first measured when patterned into a square (Fig. 53b). The diodicity of this device is shown in Fig. 55a. Again, there is a large excursion from $D = 1$ at low carrier densities, which is largely independent of temperature. No viscous rectification seems to be present in this device. This corresponds with our expectation for a symmetric shape, which should not have geometric rectification properties like the Tesla valve.

The large diodicity at low carrier density regime can be accounted for by the bias-induced carrier depletion model. The models developed in section 4.2 are visible in Fig. 55b. Especially the four-terminal model (with $\square_{2d} = 0.75$) matches the observations well. Even in a shape as simple as a square the potentials at the voltage probes are different from those at the source and drain.

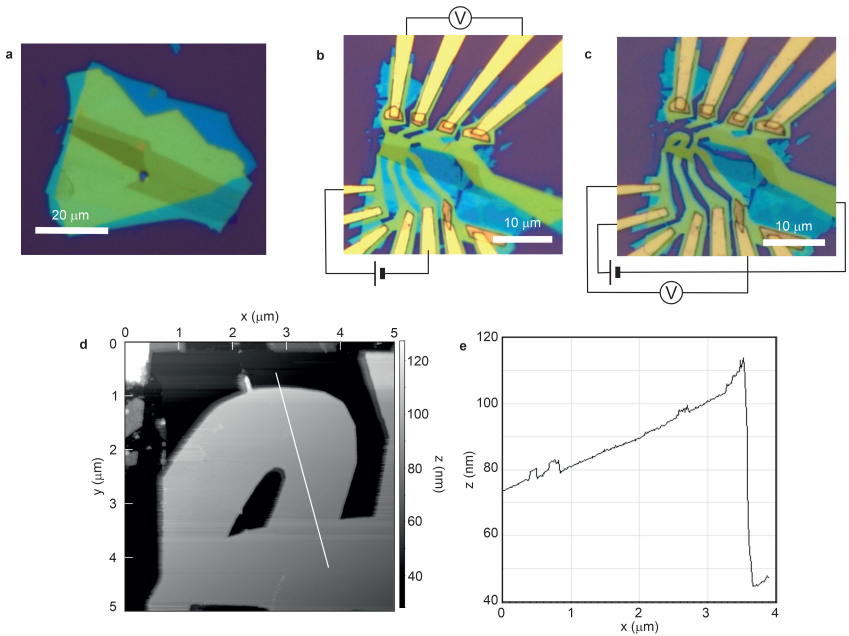


Figure 53: Fabrication of the second Tesla valve. (a) The stack as prepared. The black layer is the graphite backgate. The graphene monolayer is not visible. (b) The square device after the first patterning step, contacted with Cr/Au electrodes. (c) The Tesla valve geometry, made in the second patterning. (d) AFM image of the Tesla valve. (e) A height profile along the white line. The measurement layouts and scale bar sizes are indicated.

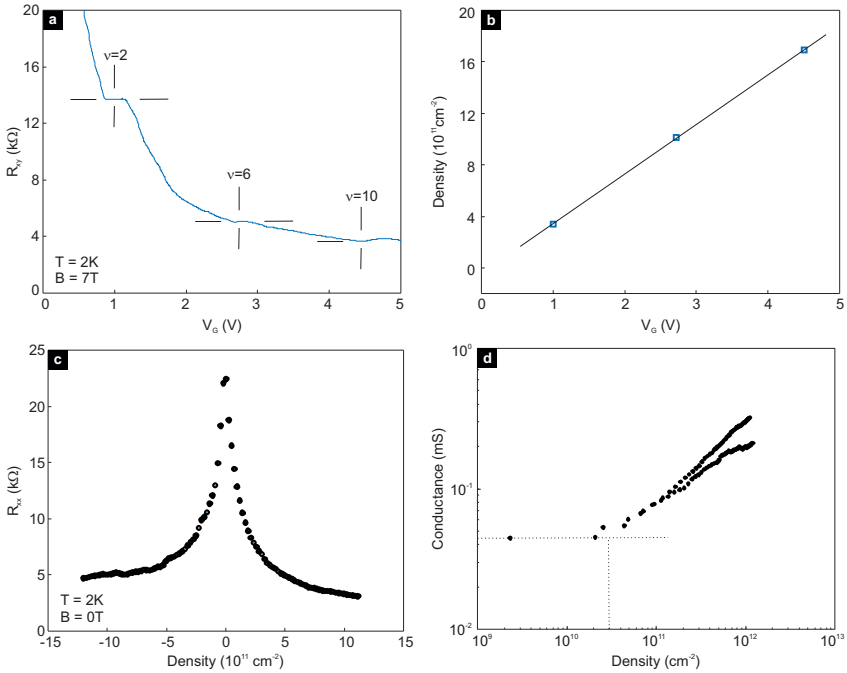


Figure 54: Characterization of Device 2. (a) Hall resistance at 7 T. Plateaus at filling factors 2 and 6 are visible. The quantum Hall plateau at filling factor 10 is poorly developed. (b) Carrier densities corresponding to the filling factors visible in a. (c) Sharp Dirac peak at the CNP. (d) Conductance and carrier density on a double logarithmic plot. The dotted lines indicate the inhomogeneity density n_0 .

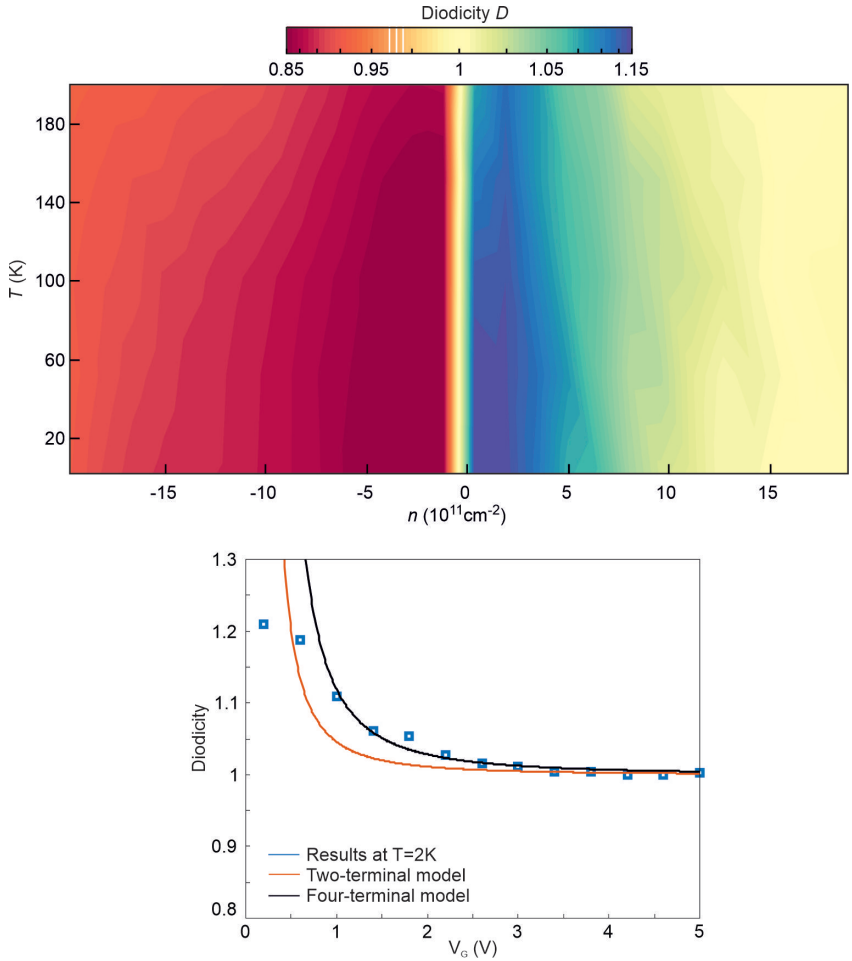


Figure 55: Diodicity of a square. The measurements show a monotonous behaviour away from the CNP. The bottom panel shows a cut at a constant temperature of 2 K. Predictions for diodicity in the two- and four-terminal transistor model are plotted in brown and black. A form factor $\square_{2d} = 0.75$ was used for the latter. The diodicity was measured at $I_f = -I_b = 8.30 \mu\text{A}$.

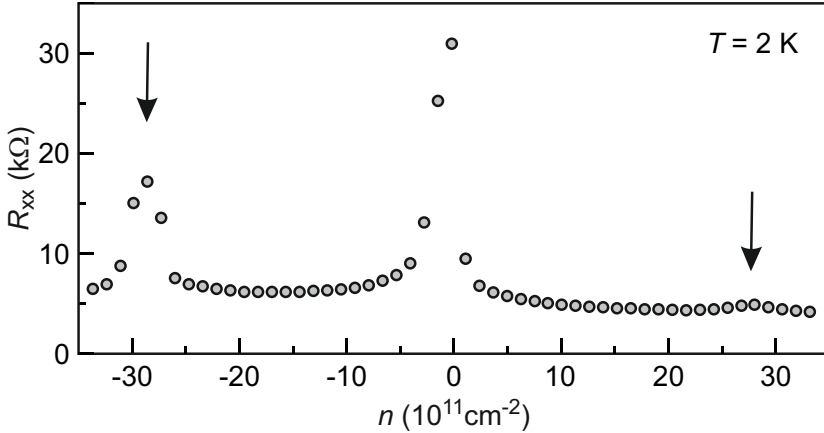


Figure 56: At large gate voltages, secondary Dirac peaks appear in R_{xx} . They indicate the presence of a superlattice.

The viscous map After the measurements on a square, Device 2 was patterned again. The final valve shape is shown in Fig. 53c.

Resistance measurements at large gate voltages ($|V_G| > 7V$) display secondary Dirac peaks. They are indicated by the arrows in Fig. 56. They appear at a carrier density $|n| \approx 2.8 \cdot 10^{12} \text{cm}^{-2}$, matching previous observations [55] of superlattices with twist angle below 1° . This carrier density – almost the smallest possible for a monolayer graphene Moiré superlattice – stems from the lattice mismatch between hBN and graphene, with zero twist angle between the lattices (section 1.5).

The full diodicity measurement of a Tesla valve with Moiré superlattice is shown in Fig. 57. 141 different gate voltages were probed at 100 different temperatures, resulting in 14100 I-V sweeps.

The largest diodicity values appear around the CNP, as expected. With a backgate that is even thinner than that of Device 2, the region in which the bias voltage is comparable with the gate voltage is even wider. This source of diodicity is well predicted by the four-terminal bias-induced carrier depletion model (Fig. 59). Note the large value of diodicity near the secondary CNP at $n \approx -29 \cdot 10^{11} \text{cm}^{-2}$. The carrier density becomes smaller again as the secondary Dirac point is approached, leading to another regime where the bias voltage creates an appreciable change in carrier density.

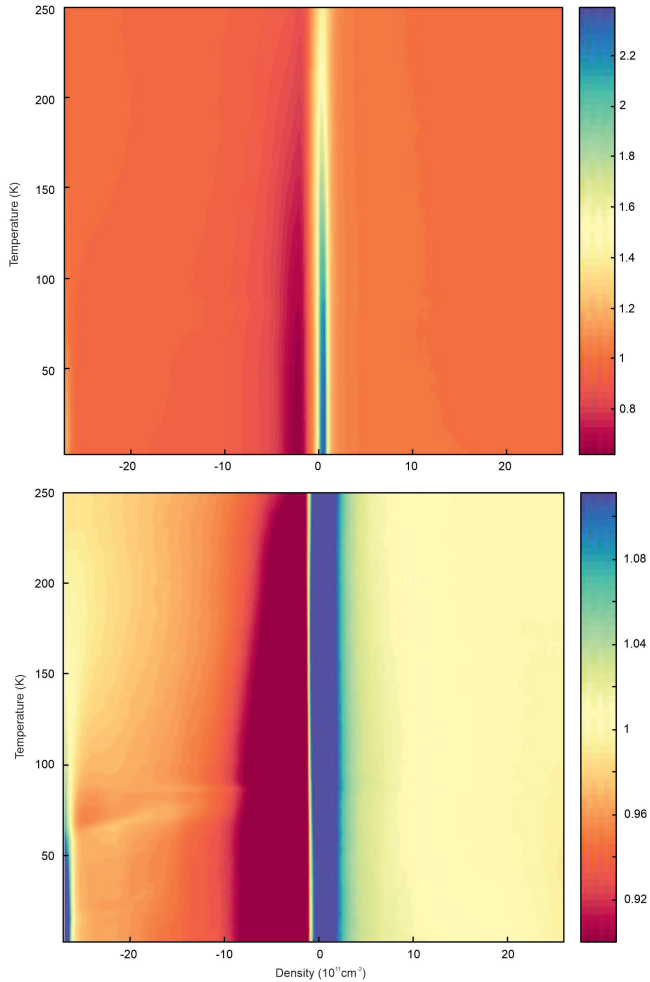


Figure 57: Diodicity of Device 2 versus carrier density and temperature. The top panel shows the data at the full scale of the results, the bottom at a reduced scale to show smaller deviations from $D = 1$. Note the nonmonotonic behaviour in the bottom left. $I_f = -I_b = 690 \text{ nA}$.

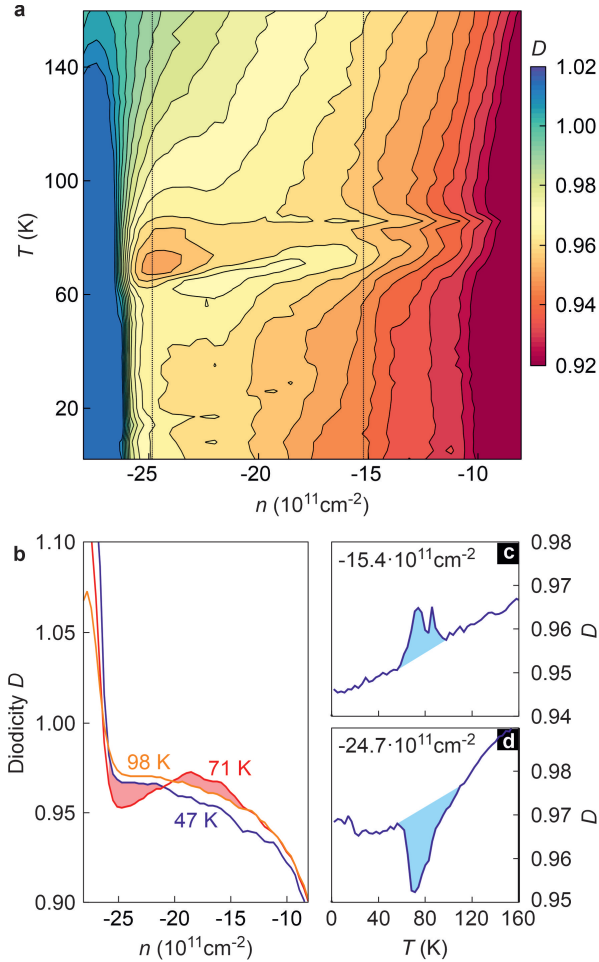


Figure 58: (a) $D(n, T)$ for a selected region of Fig. 57. (b) Cuts at constant temperature. (b, c) Cuts at constant carrier density. Shaded areas are viscous contributions to dioidicity.

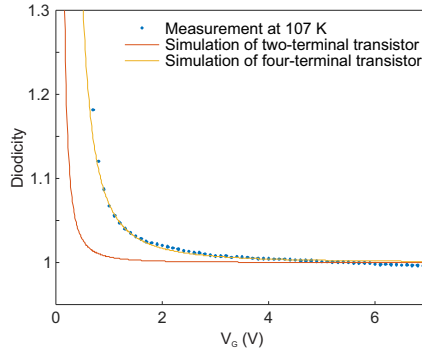


Figure 59: The model for bias-induced carrier depletion (red and yellow lines) matches the observations (blue dots) well. $\square_{2d} = 4.5$.

Fig. 58 shows the diodicity between the primary and secondary Dirac peak. It is the area with the nonmonotonous D in Fig. 57. On the left and right are the solid red and blue areas caused by bias-induced carrier depletion around the secondary and primary Dirac peaks. At most temperatures, diodicity smoothly evolves from $D > 1$ to $D < 1$.

However, this is not the case at temperatures between 50 K and 100 K. This is shown in panel b, where $D(n)$ is shown for several temperatures. The area indicated by the box is magnified in panel c. The red curve (71 K) does not evolve smoothly from one CNP to the next, as the measurements at higher (yellow line) and lower (blue line) temperature do. The excursions are indicated by the red shaded area.

We ascribe this behaviour to the viscous flow of electrons subjected to a Moiré superlattice potential. Traversing Fig. 58a from $n = 0$ to $n = -28 \cdot 10^{11} \text{ cm}^{-2}$ we encounter in turn:

- $D \ll 1$. At small gate voltages, the bias voltage across the device changes the carrier density in the device. Diodicity in this regime is well described by the model in section 4.2, as shown in Fig. 59. Diodicity approaches unity as $1/n$.
- Enhanced diodicity. At large enough carrier densities, the Tesla valve mechanism rectifies the current. The charge carriers are holes, so with the convention of “forward” as the “difficult” direction, diodicity is larger than unity. This effect only occurs in the viscous

regime (roughly at $50K < T < 100K$), as indicated by the shaded area in the cut at constant density (panel c).

- Reduced diodicity. After traversing the VHS created by the superlattice, the charge carriers now have negative charge. This means the particle flow is now opposite to the charge current direction and the particles traverse the “difficult” direction of the Tesla valve for the “backwards” current direction. Again, this effect only occurs if the carriers behave viscously, at the intermediate temperatures shown by the shaded area in panel d.
- $D \gg 1$. When approaching the secondary Dirac point, the number of charge carriers approaches zero again. The bias voltage becomes comparable to the gate voltage and again modifies the carrier density. The large signal around the primary Dirac point is replicated.

The scenario above explains the changes in diodicity in Fig. 58. A deviation from the ideal case occurs when the hole concentration is increased (panel b). Even at low and high temperature, where transport should be ballistic or diffusive, diodicity remains a few percent away from unity. This might point to some “built-in” asymmetric scattering mechanism, present at all carrier densities and temperatures. Viscous effects in the Tesla valve then show up as additional contributions, on top of the background (panel b, right).

The “viscous window” for this device is then approximately $50K < T < 100K$ and $-10 \cdot 10^{11} \text{cm}^{-2} < n < -24 \cdot 10^{11} \text{cm}^{-2}$. In contrast with Device 1, the limits for the carrier density are narrower because of the larger contribution from the bias-induced diodicity around the CNPs. It will blur out any small viscous correction to diodicity.

The Lifschitz transition between holes and electrons is visible as a sign change of the viscous contribution to diodicity. The sign change roughly happens at the correct density (Fig. 58, top) but the viscous windows of holes and secondary electrons have a very complicated shape. Scattering mechanisms, interaction strengths and viscous coefficients might change for different species of charge carriers. All of these factors affect a single number – the diodicity – which leads to an involved dependency on n and T .

In conclusion, Device 2, a Tesla valve in which the electrons experience a Moiré superlattice potential, probes the viscosity of both electrons and holes. By comparing the diodicity of an unpatterned square, material

defects can be excluded. The Tesla valve geometry itself introduces an extra rectification mechanism.

4.4 Discussion

4.4.1 Dioidicity

The figure of merit introduced in Eq. 125, the dioidicity, intends to quantify the rectifying behaviour of the Tesla valve. It is not, however, a unique choice. Rather than a ratio of resistances, it could have been defined as a ratio of differential resistances:

$$D = \frac{(dV/dI)_f}{(dV/dI)_b}. \quad (126)$$

Furthermore, the experiments described in this chapter have measured D at a certain, constant current. It is equally viable to measure at a different current, or to keep the voltage across the device constant and measure the current instead.

It is possible to calculate the dioidicity according to these alternative definitions. Fig. 60 shows alternative $D(n, T)$ plots from the data of the second Tesla valve. The original (Fig. 58) is in the top left, panel a. Panel b shows the dioidicity defined as in Eq. 126. Panel c is calculated at half the current, and panel d at a constant bias voltage.

Note that the behaviour of D is the same in all panels. The rectification due to viscous transport and channel depletion is visible. The biggest change is in the regime at low carrier density. For highly nonlinear $I(V)$ curves such as the one shown in Fig. 49, the value of D changes appreciably with the definition of dioidicity. The interpretation as bias-induced depletion of carriers (section 4.2) offers a more nuanced interpretation.

4.4.2 Measurement setup

The nonlinear behaviour at low carrier density, understood to arise from bias-induced carrier depletion, can be considered a measurement artefact. The setup used in this chapter (Fig. 46f) keeps the drain of the device grounded ($V = 0$) and applies both positive and negative bias voltages to the source. This convenient configuration comes at a cost of inducing a p-n junction in the device when the bias voltage becomes comparable to the gate voltage. This induces nonlinear behaviour (section 4.2), due to the resistance rise near the local CNP.

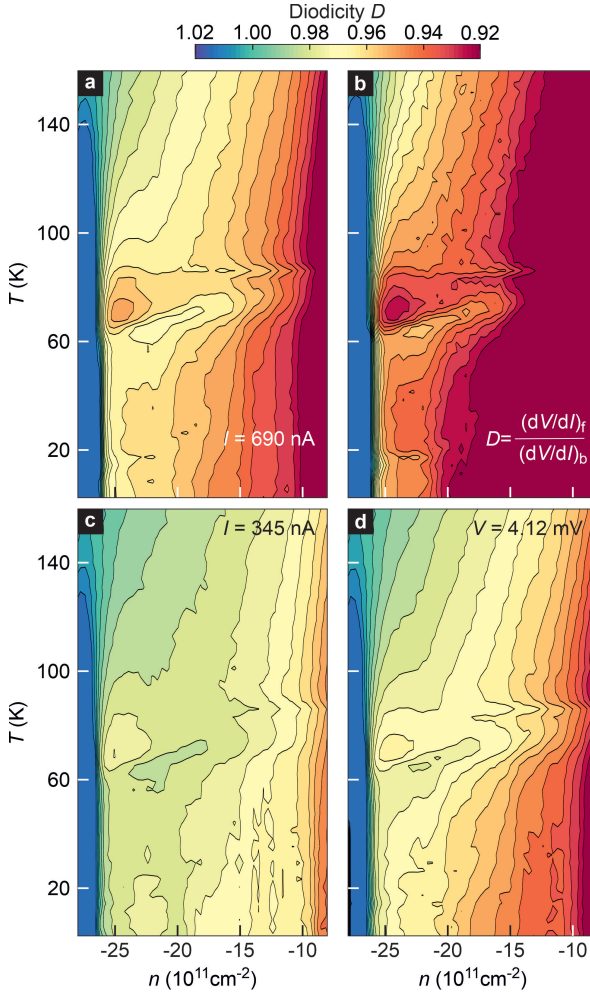


Figure 60: Plots for the second Tesla valve when defining diodicity in different ways. The alternative definitions are shown in the lower right corner of every panel. The qualitative behaviour of $D(n, T)$ is the same, regardless of definition. (a) Original, from Fig. 58 with $I_f = -I_b = 690$ nA. (b) Calculated with differential resistances, with $I_f = -I_b = 690$ nA and $I_{ac} = 40$ nA. (c) Calculated at half current, $I_f = -I_b = 345$ nA. (d) Calculated with constant voltage, $V_f = -V_b = 4.12$ mV.

A different setup could avoid the bias-induced depletion. Instead of applying a negative bias, it is also possible to exchange the roles of drain and source, in effect rotating the sample. The advantage of this configuration is that a positive bias can be applied in both measurement directions and a p-n junction is never induced.

A drawback is the two (n, T) sweeps required, now in both forward and backwards direction. It would be very difficult to measure at exactly the same values for n and T . Nonetheless, the ability to exclude the trivial rectification at low carrier density would be valuable in a Tesla valve in bilayer graphene, where the viscous regime is reached around the CNP (Fig. 18).

4.4.3 Particle flow

The Tesla valve geometry is one of the few transport experiments in condensed matter that can distinguish between electron-like and hole-like charge carriers. Other contenders are the Hall effect (section 1.2.1) and the Nernst effect [115], in which charge carriers are deflected by a magnetic field. These effects rely on the opposite charge of the carriers to differentiate between them, and require a magnetic field.

The Peltier and Seebeck effects [115] can also distinguish between electrons and holes. They describe the relation between a temperature gradient across a semiconductor in which a current flows. Because they only depend on the energy carried by the charge carrier, and not its spin, they are – to the author’s knowledge – the only transport experiments that can distinguish between electrons and holes at zero external magnetic field.

As seen in Device 2, the direction of rectification in the Tesla valve also depends on the nature of the charge carriers. The interference in the branches of the device is present or absent depending on the carrier flow direction, and not its spin.

4.4.4 Limits of operation

The viscous rectification in the two devices discussed in this chapter only occurs for a small area in (n, T) space. It is limited by ballistic transport (at low n and T) and diffuse transport (at high n and T), regimes where the electron fluid no longer conserves global momentum and the mechanism for rectification no longer works. Furthermore, the bias-induced

charge depletion (section 4.2) adds a large factor to D when the bias voltage is of a comparable magnitude to the gate voltage and obscures viscous phenomena at low carrier density.

Comparing both devices, this window in which viscous phenomena are present is quite different. For Device 1, the “hydrodynamic window” is approximately between 30K and 100K, and starts at a hole density of $5 \cdot 10^{11} \text{ cm}^{-2}$ (Fig. 47). The window for Device 2 (Fig. 57) is between approximately 50K and 100K and starts at a density of $10 \cdot 10^{11} \text{ cm}^{-2}$. The predictions in Fig. 18 were made for a lower impurity density, and the window is therefore larger. This shows how dependent the presence of viscous effects is on the absence of impurities.

More surprising is the near total lack of viscous rectification at the electron side of the $D(n, T)$ diagram. Only in Device 1, at the highest n , is there a small excursion from $D = 1$ at the highest density. In theory, both sides should be symmetric (Fig. 18). Other viscosity measurements also have some differences between electrons and holes (Fig. 20), but not to the extent seen in these devices.

There are numerous device-specific differences that can shift the window of hydrodynamic effects. Firstly, the different impurity density n_{imp} in these devices (Figs. 48 and 54d) can move the onset of viscous transport to higher temperatures or destroy it altogether.

Furthermore, the devices have a large difference in thickness of the dielectric (Figs. 46 and 53). The diodicity seen at low carrier density will emerge when bias voltage is comparable with gate voltage. A device with a larger bias, larger current and thinner hBN will show this effect first and obscure smaller viscous contributions.

The edge roughness of the devices, too, can play a role. The geometry, with two graphene ribbons intersecting, unfortunately has a large number of edges. The edges are sources of external momentum for the electron liquid and destroy emergent viscosity. Devices that were too small, with narrow graphene ribbons, did not show any viscous effects at all. The graphene ribbons in the Tesla valves presented in this chapter were large enough to overcome the disorder at the etched edges [18]. The precise impact of the edges and a minimal width of graphene ribbons, however, would require a microscopic analysis of device details and electron flow profiles.

4.4.5 Umklapp processes in Moiré superlattices

While Umklapp scattering is forbidden in monolayer graphene (Fig. 17), this no longer holds in graphene with a Moiré superlattice potential. The Brillouin Zone is now drastically shrunk, making the unit vectors $\mathbf{G}_{1,2}$ smaller and the condition in Eq. 62 can now be achieved [34]. This means Umklapp processes are allowed to destroy global momentum conservation.

The destruction of hydrodynamics in superlattices has never been studied theoretically. We note that the Umklapp scattering rate grows as T^2 [116], just as electron-electron scattering [25]. The precise strength of both scattering mechanisms then depends on the precise value of the coefficients. The results of Fig. 58 are the first observation of hydrodynamics in a graphene superlattice.

4.4.6 Maximizing diodicity

These considerations are also guidelines to get a larger viscous rectifying behaviour: lower impurity density, smoother edges and larger devices. The angle of incidence between the main and redirected channel (Figs. 46 and 53) must be as close to 180° as possible so that the momentum cancellation of the electron jets is maximized.

It might be tempting to chain multiple Tesla valves together. If we consider the devices to be lumped components, however, it is clear the *ratio* between forward and backward resistance remains the same – only the *difference* changes.

Nonetheless, an adaptation of the mechanical Tesla valve claims [117] a chain of Tesla valves will have a larger diodicity than a single valve. If the successive valves were spaced closely enough, the flow profile of the fluid after a single recombination would not recover to the usual Poiseuille profile before being split and recombined again. In some cases, this preparation of the flow profile would cause the second Tesla valve to impede flow more efficiently. Nonlinear effects such as vena contracta and wakes in the fluid could make the flow profile even more complex. In this case the lumped component model would fail and the diodicity would increase with larger number of Tesla valves. Understanding this multistage device would need a simulation of the full fluid flow. It would also be very device-specific.

4.4.7 Square versus valve

The comparison of the diodicity of a square versus that of the patterned valve is valuable in multiple regards. Any possible “built-in” sources of rectification, such as the contacts, pn junctions in the leads or asymmetric scatterers in the material can be observed before the substrate is patterned. The measurements (Fig. 55) show that the only source of rectification is the bias-induced depletion of carriers, which can be understood by the extended four-terminal transistor model (section 4.2).

Patterning the square in the valve geometry is then observed to add another contribution to diodicity at certain temperatures and carrier densities, which cannot stem from the material. This strengthens our claim that rectification here is caused by a viscous effect, made possible by the geometry.

4.5 Outlook

In application, the electronic Tesla valve is useless for rectification. A standard semiconductor diode offers far better stability, temperature range and rectification. Its value lies in demonstrating that electrons can flow viscously, in a manner exactly like classical viscous fluids. In contrast with other transport experiments [37, 41, 118] that probe this regime, it can confidently exclude ballistic effects [119] and isolate only those contributions caused by the geometry.

Now that hydrodynamic flow can be realized in electronic systems, it should be possible to adapt the wide variety of mechanical devices that exploit hydrodynamic and thermodynamic properties into electronic equivalents. Thermodynamic cycles, shockwaves, supersonic flow [120] and turbulence [121, 122] might be realized in electronic heaters, coolers, funnels, nozzles and pumps. A flexible, tunable, clean and eminently probable material such as graphene can bring these effects into reality.

5 Conclusion

The rise of graphene has been remarkable. Atomic layers of carbon, mechanically cleaved from graphite with tape and deposited on a substrate [45] have displayed a wealth of physical phenomena [123]. For example, the spacing of quantum Hall states reveals its nontrivial Berry phase [23]. The observation of Klein tunnelling [4] demonstrated that electrons in graphene obey the Dirac equation.

The combination of different two-dimensional materials in van der Waals stacks [66] has given graphene a new wind. A difference in lattice spacings between layers creates a Moiré superlattice, which yields a complex spectrum of quantum Hall states known as a Hofstadter’s butterfly [124], one of the very few recursive structures in physics. Famously, the combination of two layers of graphene at a precise “magic” angle rends them superconducting at low temperatures [125].

Graphene’s versatility is visible in a large number of chemical modifications: graphane [126], graphyne [127] and other allotropes and modifications [128] have been described. Lithium intercalation between graphene sheets [102] can be electrochemically controlled and reversed. Turning to applications, graphene has already been used as a desalination filter [129].

This work builds on this large volume of work to study two phenomena, driven by electronic correlations in graphene.

Graphene at the Van Hove singularity At very high carrier densities, the band structure of graphene features a Van Hove singularity: a saddle point, where the density of states and the effective mass are expected to diverge. Achieving this doping level is a difficult task, and relies on the growth and subsequent intercalation of a graphene layer from a SiC host [64]. After transfer in an inert atmosphere, magnetotransport at low temperature reveals a characteristic temperature T^* , below which negative magnetoresistance appears, together with a change in carrier type from p to n . This is compared with similar results in the pseudogapped cuprates, where the combination of these observations is linked to the opening of a partial gap in the density of states, a pseudogap.

An electron viscometer In high-quality graphene devices, it is possible to have electron-electron scattering be the dominant scattering mechanism. Electron momentum is then conserved globally and the electronic system behaves as a hydrodynamic liquid. Several experiments

have demonstrated small corrections to the electron conductivity, but no device that relies on hydrodynamics has been created. Here we present such an electron viscometer in the form of a graphene Tesla valve. This geometry will rectify the flow of charge current, but only if the charge carriers flow in the viscous regime. The observed rectification matches the predictions of a “viscous window” in which electron hydrodynamics is present. It shows the crossover to both ballistic and diffusive regimes, and also demonstrates the viscous flow of secondary Dirac electrons when the graphene is exposed to a Moiré superlattice.

6 Zusammenfassung

Die Physik der kondensierten Materie ist ein Teilgebiet der Physik, das sich mit dem Verhalten von Elektronen in Festkörpern beschäftigt. Es ist geprägt sowohl von sehr theoretischen Fragestellungen und Methoden, als auch von sehr alltagsrelevanten Anwendungen wie dem Transistor, der LED und dem Festkörperlaser.

Das Transportverhalten von Elektronen ist zentraler Gegenstand dieses Forschungsgebietes. Aufschluss dazu gibt das Messen elektrischer Spannungen in Materialien, durch die ein elektrischer Strom fließt, insbesondere bei extrem tiefen Temperaturen und in hohen Magnetfeldern. Auf diese Weise wurden z.B. Supraleitung und der Quanten-Hall-Effekt entdeckt. Das Verständnis solcher Effekte erhöht unser Wissen über die Wechselwirkung und das Phasenverhalten von Elektronen.

Ein Material das zuletzt viel Aufmerksamkeit auf sich gezogen hat ist Graphen—eine Einzellege von Kohlenstoffatomen mit außergewöhnlichen elektrischen und mechanischen Eigenschaften. Überraschenderweise lässt sich hochwertiges Graphen ganz einfach mittels Klebstreifen gewinnen [45]. Diese Entdeckung verhalf A. Geim und K. Novoselov 2010 zum Nobelpreis für Physik. Graphen hat sich mittlerweile als extrem vielseitiges Material zur Erforschung neuer elektronischer Phänomene erwiesen [123] und ist aus der modernen Physik der kondensierten Materie nicht mehr wegzudenken. Beispielsweise decken die Abstände der Quanten-Hall-Zustände deren nicht triviale Berry-Phasen auf [23]. Die Beobachtung des Klein-Tunnels [4] demonstriert, dass Elektronen in Graphen die Dirac-Gleichung erfüllen.

Die Kombination verschiedener zweidimensionaler Materialien in van der Waals Stapeln [66] hat Graphen neuen Aufwind gegeben. Ein Unterschied in den Abständen der Gitterebenen erschafft ein Moiré-Supergitter, welches ein komplexes Spektrum an Quanten-Hall-Zuständen hervorbringt, bekannt als ein Hofstadter-Schmetterling [124], eine der sehr wenigen rekursiven Strukturen in der Physik. Berühmtermaßen gibt es bei der Kombination von zwei Graphenlagen einen bestimmten “magischen” Winkel, welcher zu Supraleitung bei niedrigen Temperaturen führt [125].

Graphens Vielfalt wird sichtbar anhand einer großen Anzahl chemischer Modifikationen: Graphan [126], Graphyn [127] und andere Allotrope und Modifikationen [128] wurden bereits beschrieben. Lithium-Interkalation zwischen Graphenschichten [102] kann elektrochemisch kontrolliert und auch umgekehrt werden. Auf der Anwendungsseite wurde

Graphen bereits als Entsalzungsfilter erfolgreich eingesetzt [129].

Diese Arbeit baut auf dieser großen Zahl an Vorarbeiten auf, um zwei Phänomene zu untersuchen, die durch elektronische Korrelationen in Graphen getrieben werden. Zunächst werden die elektronischen Eigenschaften von Graphen vorgestellt.

Elektronentransport in Graphen Der Schlüssel zu den elektronischen Eigenschaften von Graphen liegt in der Bandstruktur der Elektronen [1] (Fig. 61). Im linken Teil der Abbildung sind die Bänder niedriger Energie dargestellt. Bei der Fermienergie, in Umgebung der Punkte K and K' , ist die Bandstruktur linear (sichtbar in der eingesetzten Grafik). Das unterscheidet Graphen sehr stark von den üblicherweise parabolischen Banddispersionen gängiger Materialien. Darüber hinaus erreicht die Fermigeschwindigkeit $v_F \approx 1 \cdot 10^6$ m/s $\approx c/300$, mit c der Geschwindigkeit von Licht in Vakuum.

Wird das Fermienergielevel erhöht, d.h. weg von den sogenannten Dirac-Punkten bewegt, so erfährt die Fermifläche (genaugenommen eine Fermilinie) eine Verkrümmung mit trigonaler Symmetrie - sog. *trigonal warping*. Es entstehen Elektronentaschen, die sich mit zunehmender Erhöhung des Fermienergielevels dehnen, um sich schließlich am M -Punkt zu treffen. An diesem Punkt ist damit eine Van Hove-Singularität der Zustandsdichte der Elektronen erreicht. Die Zustandsdichte divergiert hier ins Unendliche, was sich in der Bandstruktur als Sattelpunkt erkennen lässt (dargestellt im rechten Teil der Abb. 61). Hier bildet die Fermifläche eine lochartige Tasche um Γ anstelle elektronenartiger Taschen um K and K' .

Divergenzen sowohl der Zustandsdichte als auch der effektiven Masse der Elektronen schaffen zusammen mit einer Fermifläche, die nahezu Nesting zeigt, eine Bedingung, unter der die Wechselwirkungen zwischen Elektronen signifikant erhöht sind [6]. Eine Reihe theoretischer Arbeiten haben deswegen die Eigenschaften von Graphen bei der Van Hove-Singularität untersucht. Vorhergesagt wurden unter anderem Spindichtewellen [7], d -Wellen-Supraleitung [8], spontane Quanten-Hall-Zustände [9], $d + id$ -Wellen-Supraleitung [5, 10, 11] sowie Chern-Isolation [10]. Die experimentelle Untersuchung der Physik von Graphen bei der Van Hove-Singularität wird im ersten Teil dieser Dissertation behandelt.

Magnetotransport an der Van-Hove-Singularität Die Herstellung der Graphen Proben mit hoher Interkalation wurde durch Stefan Link

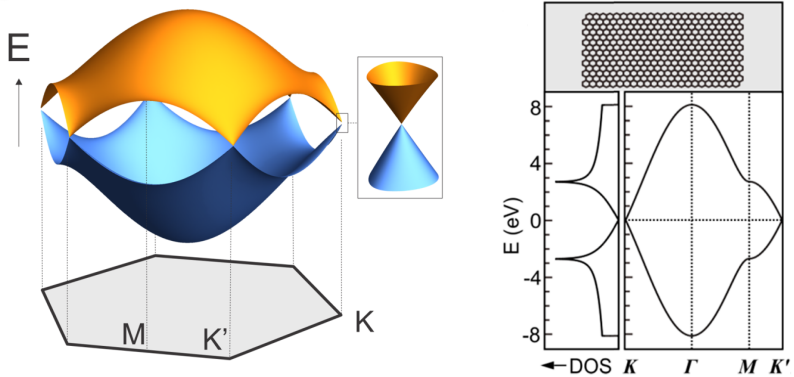


Abbildung 61: Die Bandstruktur von Einzellagen-Graphen. Die Brillouinzone ist hexagonal (grau, links unten) mit Eckpunkten K und K' . Leitungs- und Valenzband überlappen an diesen Punkten (vergrößert in der eingesetzten Abbildung). Die Zustandsdichte (rechts) ist linear um $E = 0$ und divergiert (Van Hove-Singularität) wenn das Ferminiveau bei M liegt. Angepasst von Ref. [3].

aus der Arbeitsgruppe Grenzflächenanalytik des Max Planck Instituts für Festkörperforschung unter Leitung von Ulrich Starke durchgeführt.

Der Herstellungsprozess beginnt mit 6H-SiC(0001), einem SiC Polymorph, welchen man sich aus abwechselnden Schichten aus Silizium und Kohlenstoff aufgebaut vorstellen kann. Die oberste Lage Si Atome kann durch starkes Aufheizen des Ausgangsmaterials gezielt sublimiert werden. Zurück bleibt eine Lage aus schwach gebundenen und ungeordneten Kohlenstoffatomen. Im weiteren Prozess wird das Material, welches interkaliert werden soll, aufgebracht und die Probe erneut erhitzt. Die Atome des aufgetragenen Materials diffundieren durch die graphit-ähnliche oberste Schicht und passivieren die teilweise freien Bindungen der SiC Schicht unterhalb der graphit-ähnlichen obersten Schicht. Diese wird dadurch zu einer quasi-freistehenden Graphen Monolage [69, 64].

Die mit Gd interkalierten Graphen Proben wurden anschließend ohne Kontamination mit der Raumluft, also mit Sauerstoff, in einen He-4 bzw. Mischungskryostat eingebracht und anschließend auf 20 mK abgekühlt. Nach diesen Messungen wurden die Proben wieder auf gleichem Weg (ohne Sauerstoffkontamination) zurück in die ARPES-Kammer ge-

bracht und erneut Messungen durchgeführt, wodurch die Stabilität der Dotierung gezeigt werden konnte.

Die Temperaturabhängigkeit des spezifischen Widerstands von interkaliertem Graphen wird in Fig. 62a gezeigt. Trotz der hohen Ladungsträgerdichte verhält sich Graphen an der Van-Hove-Singularität wie ein Isolator, der Widerstand steigt mit abnehmender Temperatur an. Im inneren Kasten wird der gleiche Datensatz in doppel-logarithmischer Darstellung über die $1/T$ gezeigt (Arrheniusgraph). Hieraus lassen sich zwei Aktivierungsenergie ableiten, $\Delta_1 = 200$ K im hohen Temperaturbereich und $\Delta_2 = 3$ K im niedrigen Temperaturbereich.

Abbildung 62b zeigt die Temperaturabhängigkeit des Hallkoeffizienten R_H und gibt Aufschluss über die Ladungsträgerdichte. Bei hoher Temperatur ist der Hallkoeffizient klein und positiv und hängt nicht von der Temperatur ab. Unterhalb der charakteristischen Temperatur $T^* \approx 110$ K, markiert durch den Pfeil, wechselt der Hallkoeffizient das Vorzeichen und nimmt schnell mit abnehmender Temperatur zu. Die beiden schwarzen Hilfslinien verdeutlichen den Verlauf.

In den Schaubildern c, d und e wird der Magnetowiderstand behandelt. Ungewöhnlicherweise für Graphen nimmt der Widerstand ab wenn ein Magnetfeld angelegt wird (siehe Abbildung c). Dieser negative Magnetowiderstand ist größer bei niedrigeren Temperaturen und verschwindet schließlich bei höheren Temperaturen.

Die polynomische Abhängigkeit zwischen Widerstand und Magnetfeld, $R \propto B^n$, bleibt auch bei stärkeren Feldern bestehen, wie in der doppel-logarithmischen Darstellung durch die geraden gestrichelten Linien gezeigt wird. Der Exponent n ist dabei ein Maß wie groß der negative Magnetowiderstand ist. Abbildung e zeigt $n(T)$. Der große, negative Exponent bei niedriger Temperatur verdeutlicht den großen negativen Magnetowiderstand. Oberhalb der Temperatur $T^* \approx 110$ K, nähert sich n rasch Null an und der Magnetowiderstand verschwindet.

Die charakteristische Temperatur $T^* \approx 110$ K taucht sowohl beim Hall-Widerstand als auch beim negativen Magnetowiderstand auf. Dies lässt sich, unserer Ansicht nach, dadurch erklären, dass es unterhalb von T^* zur Entstehung einer *Pseudo-Bandlücke* in Graphen an der Van-Hove-Singularität kommt, in Kombination mit einem Lifshitz Übergang.

Der temperaturabhängige Lifshitz Übergang wird in Abbildung 62b offensichtlich, wo der Hallkoeffizient das Vorzeichen bei T^* wechselt. Dies lässt sich durch eine Neuordnung der Fermi-Fläche erklären. Oberhalb von T^* entspricht die Fermi-Fläche einer großen Sphäre um Γ mit Löcher-

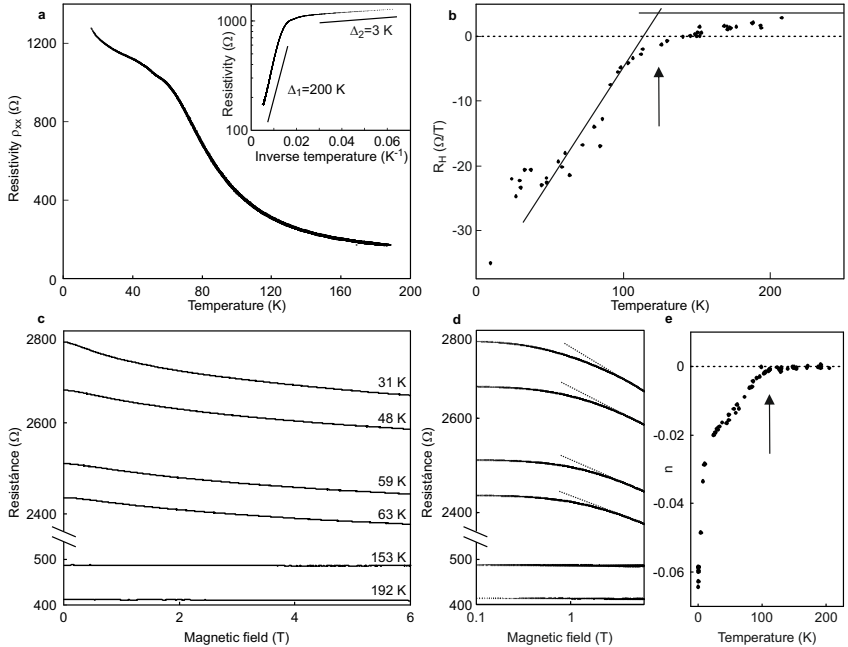


Abbildung 62: Magnetotransport Graphen bei der Van Hove-Singularität. (a) Der elektrische Widerstand in Abhängigkeit der Temperatur zeigt isolierendes Verhalten. Bildeinsatz: Arrheniusplot zeigt die Aktivierungsenergien Δ_1 und Δ_2 . (b) Der Hallkoeffizient R_H nimmt kleine, positive Werte bei tiefen und große, negative Werte bei hohen Temperaturen an. (c) Elektrischer Widerstand als Funktion des Magnetfelds bei verschiedenen Temperaturen. Man beachte den negativen Magnetowiderstand. Das Magnetfeld ist senkrecht zur Graphenebene. (d) Daten wie in (c) in doppellogarithmischer Darstellung mit polynomialem Fit im Hochfeld-Bereich. (e) Exponent n als Funktion der Temperatur, wie im Text beschrieben.

ähnlichen Ladungsträgern, was konsistent mit dem kleinen, positiven und temperaturunabhängigen Hallkoeffizient ist. Unterhalb von T^* geht die Fermi-Fläche in kleine Taschen um K, K' mit Elektronen-ähnlichen Ladungsträgern über, was zu einem großen und negativen Hallkoeffizient führt.

Ähnliche charakteristische Veränderungen in R_H , gepaart mit einem negativen Magnetowiderstand, zeigen sich auch in Cupraten mit Pseudo-Bandlücke. In beiden Fällen, für Cuprate und für Graphen, definiert die charakteristische Temperatur für die Pseudo-Bandlücke T^* den Übergang zwischen dem temperaturunabhängigen Bereich bei hoher Temperatur und dem temperaturabhängigen Verlauf bei niedrigen Temperaturen. Ein universeller, normierter Verlauf von $R_H(T)$ wurde in Cupraten gefunden [94], welcher auch gut die Daten in Graphen beschreibt.

Die Pseudo-Bandlücke ist auch die Ursache für den negativen Magnetowiderstand in Abbildung 62c. Ein angelegtes Magnetfeld hebt die Pseudo-Bandlücke auf und stellt damit die Leitfähigkeit des Zustands ohne Bandlücke wieder her [93, 89, 91]. Die gleiche polynomische Abhängigkeit $\rho \propto B^n$ (Abbildung 62d) wurde auch in Cupraten mit Pseudo-Bandlücke gefunden [89], was zur gleichen Analyse wie in Abbildung 62e mit einem Übergang zwischen $n < 0$ und $n = 0$ führt.

Elektronenhydrodynamik in Graphen Der zweite Teil dieser Dissertation behandelt die Entstehung von hydrodynamischen Effekten in Elektronenflüssigkeiten. Die Hydrodynamik beschreibt ein Fluid (wie z.B. Wasser oder Luft), auf Basis der Massen-, Impuls- und Energieerhaltung innerhalb des Fluids. Diese Größen sind immer bei der Strömung eines konventionellen Fluids erhalten, aber beinahe nie im Fall einer Elektronenflüssigkeit in einem Festkörper. Hierbei werden die Elektronen zu häufig an Störstellen oder Phononen gestreut, wodurch ein steter Impulsaustausch mit der Umgebung stattfindet, was hydrodynamisches Verhalten unterbindet. Die Elektron-Elektron-Wechselwirkung müsste der vorherrschende Streumechanismus sein, um den Gesamtimpuls zu erhalten und damit Elektronen-Hydrodynamik zu ermöglichen.

Jüngste Studien legen nahe, dass Graphen ein perfektes Modellsystem für Elektronen-Hydrodynamik darstellt, also der Beschreibung des Elektronentransports mit Hilfe der Hydrodynamik. Graphen hat viele Vorteile, um die Erhaltung des Gesamtimpulses für Elektronen zu erreichen:

- Die Elektron-Elektron-Wechselwirkung in hochreinem Graphen ist außergewöhnlich groß [30, 31], wird verstärkt durch fehlende Abschirmungseffekt nahe des Neutralitätspunkts, und nimmt schnell mit höherer Temperatur zu $\tau_{ee}^{-1} \propto T^2$.
- Die Einkapselung zwischen hBN ermöglicht die Herstellung von hochreinen und atomar-flachen Proben [32], was die Störstellendichte und die Streuung an Unebenheiten verringert.
- Die Kopplung zwischen Ladungsträgern und Phononen ist bei niedrigen Ladungsträgerdichten minimal. Betrachtet man die Fermi-Fläche für geringe Dichten (Abb. 61), ergeben sich nur wenige Möglichkeiten für Elektron-Phonon-Streuung. Die Formsteifigkeit des Gitters begrenzt die Streurrate mit Phononen [25], welche nur entsprechend $\tau_{e-ph}^{-1} \propto T$ zu nimmt.
- Umklapp-Prozesse sind in einlagigem Graphen nicht erlaubt.

Nun können wir den Parameterbereich berechnen, für welchen hydrodynamische Effekte besonders stark in Graphen sein sollten. In der Publikation [35] wird das “hydrodynamische Fenster” von einlagigem und zweilagigem Graphen bestimmt. Das Verhältnis zwischen der Elektron-Elektron-Streurate, welche den Gesamtimpuls erhält, und der größten konkurrierenden Streurrate, welchen den Gesamtimpuls nicht erhält, wird für beide Materialien als Funktion von Ladungsträgerdichte und Temperatur in einer Abbildung dargestellt. Für einlagiges Graphen gibt es einen Bereich bei mittlerer Temperatur und Dichte, in welchem Elektron-Elektron-Wechselwirkung vorherrscht. Der Bereich wird durch Störstellenstreuung bei niedriger Dichte und Temperatur begrenzt. Bei hoher Dichte und Temperatur, wird das hydrodynamische Verhalten schließlich durch Phononenstreuung zerstört.

Jüngste Forschungsarbeiten haben sich auf Elektronen-Viskosität als klares Indiz für Elektronen-Hydrodynamik konzentriert. Eine Vielzahl von Experimenten wurde durchgeführt, um viskose Effekte in Graphen zu finden. Nachdem sie in theoretischen Arbeiten hervorgesagt wurden [36], wurden Wirbelströmungen in Elektronenflüssigkeiten experimentell in Graphen nachgewiesen [37]. Ein anderer Nachweis für hydrodynamischen Fluss gelang durch die Untersuchung des elektronischen Transports durch Verengungen der Probengeometrie. Dabei wurde eine bessere Leitfähigkeit als im Fall von ballistischen Transport gemessen, was sich durch einen viskosen Elektronenfluss erklären lässt.

Die obigen Experimente erfassen nur relativ geringe Veränderungen der Leitfähigkeit. Daher wird weiter nach einem absolut eindeutigen Beweis für Elektronen-Hydrodynamik gesucht [44]. In dieser Arbeit wird eine neue Probengeometrie vorgestellt, welche einem Elektron-Viskosimeter entspricht, dessen Funktion alleinig von der Viskosität der Elektronen abhängt.

Viskose Rektifizierung in einem Graphen Tesla Ventil Die Beobachtung viskoser Effekte in Graphen beruht auf einer bestimmten Probengeometrie, einem Tesla Ventil. Diese Geometrie, abgebildet in Fig. 63b, funktioniert wie ein Ein-Weg Ventil ohne bewegliche Teile. Das Funktionsprinzip beruht auf den Eigenschaften der Flüssigkeit, ihren Fluß eigenständig zu rektifizieren. Der Fluß wird in zwei Kanäle aufgespalten wenn die Flüssigkeit von oben nach unten fließt. Einer der beiden Kanäle wird umgeleitet und trifft wieder auf den anderen Kanal unter einem bestimmten Winkel. Dort treffen die beiden Kanäle mit gegensätzlichen Geschwindigkeiten aufeinander und verlieren dadurch einen Teil der Energie.

In dem Fall, dass die Flüssigkeit von der anderen Seite eingeleitet wird, tritt dieser Effekt nicht auf. Die Flüssigkeit, die von unten nach oben fließt, bleibt hauptsächlich in dem Hauptkanal und fließt damit ohne Hindernisse. Auch wenn ein Teil des Stromes in die Schleife hineinfließt, wird er den Hauptstrom unter einem flachen Winkel treffen und wird deshalb nicht viel Energie verlieren.

Diese Probengeometrie, die in Graphen realisiert wurde, könnte dann auch die viskose Natur eines Elektronensystems erforschen. Nur in dem Fall, dass der Impuls global erhalten bleibt, wird der Elektronenfluß Energie verlieren. Die Diodizität D , welche das Verhältnis zwischen den Widerständen in den beiden Fließrichtungen beschreibt, wird als unsere Gütezahl verwendet und zeigt somit an, in welcher Region die Elektronen viskos fließen.

Die Herstellung und Strukturierung von hochqualitativem Graphen erfolgt innerhalb eines van der Waals Stapels, in welchem Graphen zwischen zwei hBN Schichten eingebettet ist. Diese dünnen Schichten eines isolierenden Materials sorgen dafür, dass Graphen geglättet und vom Substrat abgeschirmt wird. Dieser gesamte Stapel wird anschließend auf einer leitfähigen Schicht aus Graphit platziert, wodurch es möglich wird, die Ladungsträgerdichte zu verändern.

Im Zuge der Messung wird D bei einem konstanten Stromfluß für un-

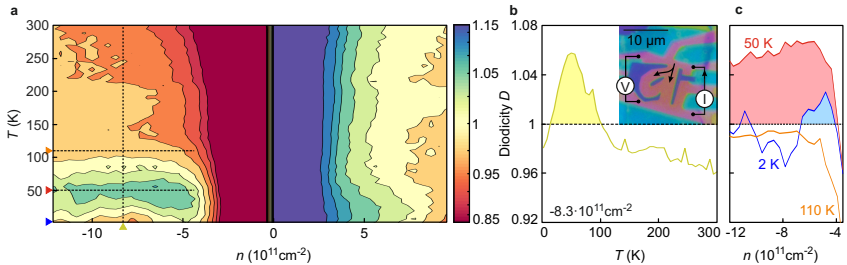


Abbildung 63: Diodizität eines Graphen Tesla Ventils als Funktion von Ladungsträgerdichte und Temperatur. (a) Abweichungen von $D = 1$ sind sichtbar sowohl in der Nähe des CNP als bei mittleren Temperaturen. (b,c) Die überschüssige Diodizität, welche einen viskosen Fluß indiziert, ist in den beiden Schnitten mit konstanter Temperatur und konstanter Dichte sichtbar. Das eingebettete Bild zeigt die Probe selbst sowie den Fluß in die "harte" Richtung.

verschiedene Ladungsträgerdichten und Temperaturen gemessen. Das Ergebnis dieser Messung ist in Fig. 63a abgebildet. In weiten Teilen der Messung beträgt die Diodizität ungefähr Eins, dargestellt durch die großen orangenen Flächen. In der Umgebung des CNP gibt es jedoch eine starke Abweichung von $D = 1$, dargestellt durch die blauen und roten vertikalen Bänder.

Dies wird dadurch verursacht dass die Quellen-Senken Spannung innerhalb der Probe lokal das Gating Potential verändert und deshalb einen Dichtegradienten innerhalb der Probe erzeugt. Dieser Effekt ähnelt dem Funktionsprinzip eines Feldeffekttransistors und kann anhand eines modifizierten Transistormodell sehr gut vorhergesagt werden.

Wesentlich interessanter ist die Fläche, bei der bei mittleren Temperaturen $D > 1$ ist, visualisiert durch die grün gefärbte Fläche in Fig. 63a. Bei diesen Temperaturen und Ladungsträgerdichten verhalten sich die Ladungsträger wie eine viskose Flüssigkeit und das Tesla Ventil funktioniert wie oben beschrieben.

Die Fläche der viskosen Rektifizierung wird bei niedrigen und hohen Temperaturen durch Flächen abgegrenzt, bei welchen die Diodizität auf Eins zurückgeht. Bei hohen Temperaturen ist dies das diffusive Regime, bei dem das normale ohmsche Verhalten wiederhergestellt wird. Bei niedrigen Temperaturen bewegen sich die Elektronen ballistisch und deshalb

gibt es keine Interaktion zwischen ihnen. Da die ballistischen Pfade zeitumkehrsymmetrisch sind, gibt es in diesem Regime keine Rektifizierung. Das Temperaturverhalten der Rektifizierung wird in Abbildung b gezeigt. Die schattierte Fläche indiziert den Temperaturbereich, in dem die Diodizität größer als erwartet ist.

Die viskose Rektifizierung wird auch zerstört, wenn die Ladungsträgerdichte auf Werte unterhalb von ungefähr $4 \cdot 10^{11} \text{ cm}^{-2}$ abgesenkt wird, dargestellt in Abbildung b. Bei niedrigen (2 K) und hohen (111.5 K) Temperaturen ist die Diodizität annähernd Eins. Nur bei mittleren Temperaturen (50.6 K) gibt es eine auffällige Rektifizierung, wie gezeigt in Abbildung c.

Die *Richtung* der Rektifizierung stimmt mit der Geometrie der Probe überein (Einschub in Abbildung b). Ladungsträger mit positiver Ladung bewegen sich in die selbe Richtung wie der Stromfluß. In diesem Fall ist die "schwierige" Richtung mit erhöhten Verlusten die "Vorwärts" Richtung, welche zu einer Diodizität größer als Eins führt.

Kurioserweise gibt es einen Mangel an Rektifizierung auf der Seite der Elektronen. Theoretisch sollte diese Seite identisch sein, in der Praxis haben aber die meisten Graphen Proben eine niedrigere Beweglichkeit für negative Ladungsträger. Unterschiede in der lokalen Störstellendichte könnte ebenfalls das "viskose Fenster" verschieben.

Dieses Experiment wurde mit einer Graphenlage wiederholt, die einem Moiré Supergitter ausgesetzt ist. Dieses Supergitter, gebildet mit einer benachbarten hBN Lage, erzeugt ein Superpotential über das gesamte Graphen. Im Gegenzug wird die Brillouin Zone verkleinert und die Bänder werden gefaltet. Die resultierende Bandstruktur sieht so aus wie diejenige von regulärem Graphen, jedoch mit einer drastisch reduzierten Energieskala. In diesem Fall kann die Van Hove Singularität dann durch kapazitives Gating erreicht werden.

Innerhalb der zweiten Probe können wir die Effekte des Supergitters in der $D(n, T)$ Karte beobachten. Wenn die Probe sich von dem ersten Ladungsträger-Neutralitätspunkt entfernt, wird zuerst die Diodizität erhöht, da die Ladungsträger sich ähnlich wie Löcher verhalten. Wenn dann die VHS durchquert wird, kippt die Diodizität schlagartig um und verringert sich zu einem Wert unterhalb des Untergrunds, was indiziert dass die Loch-ähnlichen Ladungsträger in die entgegengesetzte Richtung fließen. Dies ist wiederum nur bei mittleren Temperaturen beobachtbar. Bei höheren und niedrigeren Temperaturen besitzen das diffusive und das ballistische Fließregime diese Eigenschaft nicht. Das Tesla Ventil in

Graphen mit einem Moiré Supergitter kann somit den viskosen Fluß von Elektronen und von Löchern untersuchen.

7 Samenvatting

Grafeen heeft een opmerkelijk succes gekend. Deze atomaire lagen koolstof, mechanisch gekleefd uit grafiet met plakband en gedeponeerd op een substraat [45], hebben een waaier aan fenomenen getoond. Bijvoorbeeld, de stappen tussen de kwantum-Halltoestanden onthullen de niet-triviale Berry-fase [23]. De observatie van Kleintunnelling [4] toonde aan dat de elektronen in grafeen de diracvergelijking volgen.

De combinatie met andere tweedimensionale materialen in een van der Waalsstapel heeft een nieuwe wind laten waaien in het grafeenonderzoek. Verschillen tussen de roosterafstanden van de lagen veroorzaken een moirépatroon, wat zichtbaar is in het complexe kwantum-Hallspectrum gekend als een “Hofstadter’s butterfly”. Dit is één van de zeer weinige fractale structuren in de fysica. Bekend ook is het verschijnen van supergeleiding wanneer twee grafeenlagen op een bepaalde “magische” hoek worden gecombineerd [125].

De veelzijdigheid van grafeen wordt duidelijk in het grote aantal chemische aanpassingen: grafaan [126], grafyn [127] en andere allotropen [128] zijn al beschreven. Lithiumatomen kunnen elektrochemisch tussen tweelagig grafeen worden gevoegd, gecontroleerd en weer verwijderd [102]. Gelet op toepassingen wordt grafeen al als een ontziltingsfilter gebruikt [129].

Deze thesis bouwt voort op deze resultaten en bestudeert twee fenomenen, veroorzaakt door elektronische correlaties in grafeen.

Grafeen bij de Van Hovesingulariteit Bij zeer hoge ladingsdichtheid heeft de bandstructuur van grafeen een Van Hovesingulariteit: een zadelpunt waar de toestandsdichtheid en de effectieve massa divergeren. Deze ladingsdichtheid bereiken is een moeilijke opgave, maar is mogelijk door het groeien en intercaleren van een laag grafeen uit een SiC-kristal [64]. Na de transfer in inerte atmosfeer blijkt uit het magnetotransport bij lage temperatuur dat onder een bepaalde temperatuur T^* zowel negatieve magnetoweerstand optreedt, samen met een verandering van het type ladingdrager (van p naar n). Dit resultaat wordt vergeleken met het gedrag van hogetemperatuursupergeleiders, waar de combinatie van deze twee fenomenen wordt toegeschreven aan het verschijnen van een minimum in de toestandsdichtheid, een “pseudogap”.

Een elektronische viscometer In grafeen van hoge kwaliteit kan elektron-elektron-verstrooiing het dominante verstrooiingsmechanisme zijn. In dat geval wordt de impuls van de elektronen globaal bewaard, en gedraagt het elektronische systeem zich als een hydrodynamische vloeistof. Verschillende experimenten hebben al kleine correcties in de geleiding aangetoond, maar er is nog geen toepassing die rust op elektronhydrodynamica. Hier stellen we een elektronische viscometer voor, een Teslaven-tiel uit grafeen. Deze opstelling rectificeert de elektrische stroom, maar enkel als de ladingsdragers als een viskeuze vloeistof stromen. De vast-gestelde rectificatie komt overeen met de voorspellingen van een “viskeus venster”, waar viskeuze effecten plaatsvinden. De overgang naar zowel ballistisch als diffuus transport wordt gemeten, samen met de viscositeit van secundaire Dirac-elektronen wanneer het grafeen een moirépatroon vormt.

Acknowledgements

Writing a thesis is a monumental task. It has been my great fortune of being surrounded by so many talented people who have aided me with this task, and whom I would like to thank:

- Jurgen Smet, in whose lab I had the opportunity and freedom to work on some of the most interesting topics in physics;
- professors Hans Peter Büchler and Martin Dressel, who formed the PhD committee;
- Ulrich Starke and his group members, Hrag Karakachian, Stefan Link and Philipp Rosenzweig, for their collaboration on highly doped graphene;
- Klaus von Klitzing, for his advice and encouragement to try out Friday afternoon experiments;
- all group members of past and present, Joseph Falson, Sven Fecher, Benedikt Frieß, Patrick Herlinger, Youngwook Kim, Matthias Kühne, Federico Paolucci, Daniela Tabrea, Fangdong Tang, Qixing Wang, Sheng Yang, Yijin Zhang and Dong Zhao, for the creative atmosphere in which science can thrive;
- in particular Sven Fecher, Benedikt Frieß, Patrick Herlinger and Matthias Kühne, who have translated the summary and Daniela Tabrea for her continued moral support;
- the group technicians of past and present, Gunther Euchner, Sanela Goeres and Steffen Wahl, for their support in realizing and running experiments;
- the NSL clean room team, for facilitating the creation of high quality graphene devices;
- Michael Eppard and Ruth Jenz, for their guidance through the administrative maze;
- my friends at home, Alex Geboers, Jasper Hilven, Tim Leurs, Madhushankar Bettadahalli “Madhu” Nandishaiah and Astrid Vanoppen, for their support and hospitality;

- and my family, Ria Geeroms, Filip Geurs, Maria Clara Geurs and Steven Coesemans, who encouraged me to pursue science, and to whom I sometimes do not show enough gratitude.

This research was performed in a turbulent time in history. I need only mention the American presidency, the Brexit and covid-19. Sometimes all you can do is science.

A Recipes for van der Waals heterostructure fabrication

The polymer drop is made from Elvacite 2552 (Lucite International), mixed with anisole in a 1:1 ratio. A droplet of this mixture is placed on a glass slide and baked at 160 °C for 4 minutes until the desired hardness is reached.

Exfoliation takes place with Scotch “Magic” tape on Si substrates with 300 nm SiO₂. These substrates were either used as-is or after a short plasma treatment in Ar/O₂ atmosphere before exfoliation, depending on the desired adhesion.

Picking up and positioning of the flakes happens in the stacking tool (Fig. 24) at 110 °C. Once the stack is complete, the target substrate is brought to 180 °C to release the stack from the polymer bubble.

The stack is cleaned in an annealing chamber (AO600 annealing oven, MBE Komponenten) at 500 °C for 10 minutes in forming gas (10:90 H₂/N₂ mixture).

Patterns are written with electron beam lithography (JEOL JBX 6300FS, 20 kV acceleration at variable current) in two layers of resist (PMMA 90k and 250k). Etching of exposed areas happens by reactive ion etching (Oxford Instruments PlasmaPro 100 Cobra) in O₂ atmosphere for graphene and Ar/SF₆ atmosphere for hBN. Removal of resist occurs in acetone, followed by an IPA rinse.

Electrical contacts are also defined by electron beam lithography (10 nA *high current* mode), followed by thermal evaporation of Cr (10 nm) and Au (50 nm). The sample is rotated during evaporation for better coverage of steps.

B Measurements with alternating current

Noise is a large problem in electrical measurements. A lot of effort has gone into minimizing the external noise from the environment, but the intrinsic noise of the sample and wiring itself cannot be avoided. It is very well possible the signal of interest is orders of magnitude smaller than the noise level. Using direct current (dc), it would be impossible to measure anything meaningful in this situation. Alternating current (ac) measurements are the solution.

Neither the sample nor the wires can change the frequency of the input signal. This is different from noise, which affects all frequencies. Therefore, if the input frequency ω_r is known, we know that at the output all other frequencies can be discarded. The signal can now be measured accurately, and with essentially zero noise. A lock-in amplifier can perform this operation.

B.1 Principles of lock-in measurements

The lock-in amplifier receives a signal from the sample $V_{sig} \sin(\omega_r t + \theta_{sig})$ and a reference signal from the signal generator $V_{ref} \sin(\omega_r + \theta_{ref})$.

The amplifier simply multiplies these two signals:

$$\begin{aligned} V_{out} &= V_{sig} \sin(\omega_r t + \theta_{sig}) \cdot V_{ref} \sin(\omega_r + \theta_{ref}) \\ &= \frac{1}{2} V_{sig} V_{ref} \cos(0 \cdot t + \theta_{sig} - \theta_{ref}) \\ &\quad - \frac{1}{2} V_{sig} V_{ref} \cos(2\omega_r t + \theta_{sig} + \theta_{ref}). \end{aligned}$$

This is the sum of a dc signal and an ac signal at double the frequency. After a low-pass filter, the dc component remains:

$$V_{out} = \frac{1}{2} V_{sig} V_{ref} \cos(\theta_{sig} - \theta_{ref}). \quad (127)$$

To eliminate the cosine, modern lock-in amplifiers also use the shifted reference $V_{ref} \sin(\omega_r t + \theta_{ref} + 90^\circ)$ to generate a shifted output

$$V_{out,shift} = V_{out} = \frac{1}{2} V_{sig} V_{ref} \sin(\theta_{sig} - \theta_{ref}). \quad (128)$$

From these two voltages, the signal voltage can be calculated and presented as a vector with two components:

$$X = V_{sig} \cos \theta$$

$$Y = V_{sig} \sin \theta.$$

X is called the in-phase component, Y the out-of-phase or quadrature component. For resistive measurements, the reference phase is usually adjusted to match the signal phase ($\theta = 0$), since no phase shifts are expected to occur. A nonzero Y can indicate capacitive or inductive behaviour.

References

- [1] A. H. Castro Neto, F. Guinea, N. M R Peres, K. S. Novoselov, and Andre K. Geim. The electronic properties of graphene. *Reviews of Modern Physics*, 81(1):109–162, 2009.
- [2] Neil Ashcroft and David Mermin. *Solid State Physics*. Holt, Rinehart and Winston, 1976.
- [3] Youngwook Kim, Patrick Herlinger, Pilkyung Moon, Mikito Koshino, Takashi Taniguchi, Kenji Watanabe, and Jurgen H. Smet. Charge Inversion and Topological Phase Transition at a Twist Angle Induced van Hove Singularity of Bilayer Graphene. *Nano Letters*, 16(8):5053–5059, 2016.
- [4] Mikhail I. Katsnelson, K. S. Novoselov, and Andre K. Geim. Chiral tunnelling and the Klein paradox in graphene. *Nature Physics*, 2(9):620–625, 2006.
- [5] Rahul Nandkishore, Leonid S. Levitov, and Andrey V. Chubukov. Chiral superconductivity from repulsive interactions in doped graphene. *Nature Physics*, 8(2):158–163, 2012.
- [6] I E Dzyaloshinskii. Superconducting transitions due to Van Hove singularities in the electron spectrum. *Sov. Phys. JETP*, 66(4):848–854, 1988.
- [7] D. Makogon, R. van Gelderen, R. Roldán, and C. Morais Smith. Spin-density-wave instability in graphene doped near the van Hove singularity. *Physical Review B*, 84(12):125404, 2011.
- [8] J. González. Kohn-Luttinger superconductivity in graphene. *Physical Review B*, 78(20):205431, 2008.
- [9] Tao Li. Spontaneous quantum Hall effect in quarter-doped Hubbard model on honeycomb lattice and its possible realization in doped graphene system. *Europhysics Letters*, 97(3):37001, 2012.
- [10] Wan-Sheng Wang, Yuan-Yuan Xiang, Qiang-Hua Wang, Fa Wang, Fan Yang, and Dung-Hai Lee. Functional renormalization group and variational Monte Carlo studies of the electronic instabilities in graphene near 1/4 doping. *Physical Review B*, 85(3):035414, 2012.

- [11] Maximilian L. Kiesel, Christian Platt, Werner Hanke, Dmitry A. Abanin, and Ronny Thomale. Competing many-body instabilities and unconventional superconductivity in graphene. *Physical Review B*, 86(2):020507, 2012.
- [12] Annica M. Black-Schaffer and Carsten Honerkamp. Chiral d -wave superconductivity in doped graphene. *Journal of Physics: Condensed Matter*, 26(42):423201, 2014.
- [13] Benedikt Frieß. *Spin and Charge Ordering in the Quantum Hall Regime*. Springer Theses. Springer International Publishing, 2016.
- [14] David Tong. *Lectures on the Quantum Hall Effect*. Lecture notes, <http://www.damtp.cam.ac.uk/user/tong/qhe.html>, 2016.
- [15] Zyun F. Ezawa. *Quantum Hall effects*. World Scientific, 2013.
- [16] Klaus v. Klitzing, G. Dorda, and M. Pepper. New Method for High-Accuracy Determination of the Fine-Structure Constant Based on Quantized Hall Resistance. *Physical Review Letters*, 45(6):494–497, 1980.
- [17] Klaus von Klitzing. Essay: Quantum Hall Effect and the New International System of Units. *Physical Review Letters*, 122(20):200001, 2019.
- [18] Dorri Halbertal, Moshe Ben Shalom, Aviram Uri, Kousik Bagani, Alexander Y. Meltzer, Ido Marcus, Yuri Myasoedov, John Birkbeck, Leonid S. Levitov, Andre K. Geim, and Eli Zeldov. Imaging resonant dissipation from individual atomic defects in graphene. *Science*, 358(6368):1303–1306, 2017.
- [19] D. B. Chklovskii, B. I. Shklovskii, and L. I. Glazman. Electrostatics of edge channels. *Physical Review B*, 46(7):4026–4034, 1992.
- [20] Erik Ahlswede. *Potential- und Stromverteilung beim bestimmt mittels Rasterkraftmikroskopie*. PhD thesis, University of Stuttgart, 2002.
- [21] Y. Y. Wei, J. Weis, Klaus v. Klitzing, and K. Eberl. Edge Strips in the Quantum Hall Regime Imaged by a Single-Electron Transistor. *Physical Review Letters*, 81(8):1674–1677, 1998.

- [22] K. S. Novoselov, Andre K. Geim, S. V. Morozov, D Jiang, Mikhail I. Katsnelson, I V Grigorieva, S V Dubonos, and A A Firsov. Two-dimensional gas of massless Dirac fermions in graphene. *Nature*, 438(7065):197–200, 2005.
- [23] Yuanbo Zhang, Yan-Wen Tan, Horst L Stormer, and Philip Kim. Experimental observation of the quantum Hall effect and Berry’s phase in graphene. *Nature*, 438(7065):201–204, 2005.
- [24] Nicholas Read. Topological phases and quasiparticle braiding. *Physics Today*, 65(7):38–43, 2012.
- [25] Marco Polini and Andre K. Geim. Viscous electron fluids. *Physics Today*, 73(6):28–34, 2020.
- [26] P. L. Taylor. The Inelastic Scattering of Electrons at Impurities in Metals. *Proceedings of the Physical Society*, 80(3):755–758, 1962.
- [27] L.W. Molenkamp and M.J.M. de Jong. Observation of Knudsen and Gurzhi transport regimes in a two-dimensional wire. *Solid-State Electronics*, 37(4-6):551–553, 1994.
- [28] R.N. Gurzhi. Minimum of Resistance in Impurity Free Conductors. *Sov. Phys. JETP*, 17(2):521, 1963.
- [29] R.N. Gurzhi. Hydrodynamic effects in solids at low temperature. *Uspekhi Fizicheskikh Nauk*, 94(4):689–718, 1968.
- [30] Lars Fritz, Jörg Schmalian, Markus Müller, and Subir Sachdev. Quantum critical transport in clean graphene. *Physical Review B*, 78(8):085416, 2008.
- [31] Alexander B. Kashuba. Conductivity of defectless graphene. *Physical Review B*, 78(8):085415, 2008.
- [32] Cory R. Dean, Andrea F. Young, Inanc Meric, C. Lee, L. Wang, S. Sorgenfrei, K. Watanabe, Takashi Taniguchi, Philip Kim, Kenneth L. Shepard, and J. Hone. Boron nitride substrates for high-quality graphene electronics. *Nature Nanotechnology*, 5(10):722–726, 2010.
- [33] A. A. Maznev and O. B. Wright. Demystifying Umklapp vs normal scattering in lattice thermal conductivity. *American Journal of Physics*, 82(11):1062–1066, 2014.

- [34] J. R. Wallbank, R. Krishna Kumar, M. Holwill, Z. Wang, G. H. Auton, J. Birkbeck, A. Mishchenko, L. A. Ponomarenko, K. Watanabe, T. Taniguchi, K. S. Novoselov, I. L. Aleiner, A. K. Geim, and V. I. Fal'ko. Excess resistivity in graphene superlattices caused by umklapp electron–electron scattering. *Nature Physics*, 15(1):32–36, 2019.
- [35] Derek Y. H. Ho, Indra Yudhistira, Nilotpal Chakraborty, and Shafique Adam. Theoretical determination of hydrodynamic window in monolayer and bilayer graphene from scattering rates. *Physical Review B*, 97(12):121404, 2018.
- [36] Leonid Levitov and Gregory Falkovich. Electron viscosity, current vortices and negative nonlocal resistance in graphene. *Nature Physics*, 12(7):672–676, 2016.
- [37] D. A. Bandurin, I. Torre, R. K. Kumar, M. Ben Shalom, A. Tomadin, A. Principi, G. H. Auton, E. Khestanova, K. S. Novoselov, I. V. Grigorieva, L. A. Ponomarenko, A. K. Geim, and Marco Polini. Negative local resistance caused by viscous electron backflow in graphene. *Science*, 351(6277):1055–1058, 2016.
- [38] Gregory Falkovich and Leonid Levitov. Linking Spatial Distributions of Potential and Current in Viscous Electronics. *Physical Review Letters*, 119(6):066601, 2017.
- [39] Francesco M. D. Pellegrino, Iacopo Torre, Andre K. Geim, and Marco Polini. Electron hydrodynamics dilemma: Whirlpools or no whirlpools. *Physical Review B*, 94(15):155414, 2016.
- [40] Youngwoo Nam, Dong-Keun Ki, David Soler-Delgado, and Alberto F. Morpurgo. Electron–hole collision limited transport in charge-neutral bilayer graphene. *Nature Physics*, 13(12):1207–1214, 2017.
- [41] R. Krishna Kumar, Denis A. Bandurin, Francesco M. D. Pellegrino, Y. Cao, A. Principi, H. Guo, G. H. Auton, M. Ben Shalom, L. A. Ponomarenko, G. Falkovich, K. Watanabe, Takashi Taniguchi, I. V. Grigorieva, Leonid S. Levitov, Marco Polini, and A. K. Geim. Superballistic flow of viscous electron fluid through graphene constrictions. *Nature Physics*, 13(12):1182–1185, 2017.

- [42] Henk Van Houten and C. W. J. Beenakker. Quantum point contacts. *Physics Today*, 49(7):22–27, 1996.
- [43] Haoyu Guo, Ekin Ilseven, Gregory Falkovich, and Leonid S. Levitov. Higher-than-ballistic conduction of viscous electron flows. *Proceedings of the National Academy of Sciences*, 114(12):3068–3073, 2017.
- [44] Andrew Lucas and Kin Chung Fong. Hydrodynamics of electrons in graphene. *Journal of Physics: Condensed Matter*, 30(5):053001, 2018.
- [45] K. S. Novoselov, Andre K. Geim, S. V. Morozov, Jiang D., Y. Zhang, S. V. Dubonos, Irina V. Grigorieva, and A A Firsov. Electric Field Effect in Atomically Thin Carbon Films. *Science*, 306(5696):666–669, 2004.
- [46] Sungjae Cho and Michael S. Fuhrer. Charge transport and inhomogeneity near the minimum conductivity point in graphene. *Physical Review B*, 77(8):081402, 2008.
- [47] J. Martin, N. Akerman, G. Ulbricht, T. Lohmann, J. H. Smet, K. von Klitzing, and A. Yacoby. Observation of electron–hole puddles in graphene using a scanning single-electron transistor. *Nature Physics*, 4(2):144–148, 2008.
- [48] Yuanbo Zhang, Victor W. Brar, Caglar Girit, Alex Zettl, and Michael F. Crommie. Origin of spatial charge inhomogeneity in graphene. *Nature Physics*, 5(10):722–726, 2009.
- [49] Marco Gibertini, Andrea Tomadin, Francisco Guinea, Mikhail I. Katsnelson, and Marco Polini. Electron-hole puddles in the absence of charged impurities. *Physical Review B*, 85(20):201405, may 2012.
- [50] Jiamin Xue, Javier Sanchez-Yamagishi, Danny Bulmash, Philippe Jacquod, Aparna Deshpande, K. Watanabe, T. Taniguchi, Pablo Jarillo-Herrero, and Brian J. LeRoy. Scanning tunnelling microscopy and spectroscopy of ultra-flat graphene on hexagonal boron nitride. *Nature Materials*, 10(4):282–285, 2011.
- [51] Inanc Meric, Melinda Y. Han, Andrea F. Young, Barbaros Ozyilmaz, Philip Kim, and Kenneth L. Shepard. Current saturation in

- zero-bandgap, top-gated graphene field-effect transistors. *Nature Nanotechnology*, 3(11):654–659, 2008.
- [52] Hsin-Ying Chiu, Vasili Perebeinos, Yu-Ming Lin, and Phaedon Avouris. Controllable p-n Junction Formation in Monolayer Graphene Using Electrostatic Substrate Engineering. *Nano Letters*, 10(11):4634–4639, 2010.
- [53] Nuno J.G. Couto, Davide Costanzo, Stephan Engels, Dong-Keun Ki, Kenji Watanabe, Takashi Taniguchi, Christoph Stampfer, Francisco Guinea, and Alberto F. Morpurgo. Random Strain Fluctuations as Dominant Disorder Source for High-Quality On-Substrate Graphene Devices. *Physical Review X*, 4(4):041019, 2014.
- [54] Matthew Yankowitz, Jiamin Xue, Daniel Cormode, Javier D. Sanchez-Yamagishi, K. Watanabe, T. Taniguchi, Pablo Jarillo-Herrero, Philippe Jacquod, and Brian J. LeRoy. Emergence of superlattice Dirac points in graphene on hexagonal boron nitride. *Nature Physics*, 8(5):382–386, 2012.
- [55] L. A. Ponomarenko, R. V. Gorbachev, G. L. Yu, D. C. Elias, R. Jalil, A. A. Patel, A. Mishchenko, A. S. Mayorov, C. R. Woods, J. R. Wallbank, M. Mucha-Kruczynski, B. A. Piot, M. Potemski, I. V. Grigorieva, K. S. Novoselov, F. Guinea, V. I. Fal’ko, and Andre K. Geim. Cloning of Dirac fermions in graphene superlattices. *Nature*, 497(7451):594–597, 2013.
- [56] S. M. Sze and K. K. Ng. *Physics of Semiconductor Devices*. John Wiley & Sons, third edition, 2006.
- [57] Andrea F. Young, Cory R. Dean, Inanc Meric, S. Sorgenfrei, H. Ren, K. Watanabe, Takashi Taniguchi, J. Hone, K. L. Shepard, and Philip Kim. Electronic compressibility of layer-polarized bilayer graphene. *Physical Review B*, 85(23):235458, 2012.
- [58] S. L. Tomarken, Y. Cao, A. Demir, K. Watanabe, Takashi Taniguchi, P. Jarillo-Herrero, and R. C. Ashoori. Electronic Compressibility of Magic-Angle Graphene Superlattices. *Physical Review Letters*, 123(4):046601, 2019.
- [59] Serge Luryi. Quantum capacitance devices. *Applied Physics Letters*, 52(6):501–503, 1988.

- [60] Jessica L McChesney, Aaron Bostwick, Taisuke Ohta, Thomas Seyller, Karsten Horn, J. González, and Eli Rotenberg. Extended van Hove Singularity and Superconducting Instability in Doped Graphene. *Physical Review Letters*, 104(13):136803, 2010.
- [61] Takuya Fujimoto and Kunio Awaga. Electric-double-layer field-effect transistors with ionic liquids. *Physical Chemistry Chemical Physics*, 15(23):8983, 2013.
- [62] Dmitri K. Efetov and Philip Kim. Controlling Electron-Phonon Interactions in Graphene at Ultrahigh Carrier Densities. *Physical Review Letters*, 105(25):256805, 2010.
- [63] Eri Uesugi, Hidenori Goto, Ritsuko Eguchi, Akihiko Fujiwara, and Yoshihiro Kubozono. Electric double-layer capacitance between an ionic liquid and few-layer graphene. *Scientific Reports*, 3(1):1595, 2013.
- [64] S. Link, S. Forti, A. Stöhr, K. Küster, M. Rösner, Daniel Hirschmeier, C. Chen, J. Avila, M. C. Asensio, A. A. Zakharov, T. O. Wehling, A. I. Lichtenstein, Mikhail I. Katsnelson, and U. Starke. Introducing strong correlation effects into graphene by gadolinium intercalation. *Physical Review B*, 100(12):121407, 2019.
- [65] K. S. Novoselov, D Jiang, F Schedin, T J Booth, V V Khotkevich, S. V. Morozov, and Andre K. Geim. Two-dimensional atomic crystals. *Proceedings of the National Academy of Sciences*, 102(30):10451–10453, 2005.
- [66] Pulickel Ajayan, Philip Kim, and Kaustav Banerjee. Two-dimensional van der Waals materials. *Physics Today*, 69(9):38–44, 2016.
- [67] Niclas Lindvall, Alexey Kalabukhov, and August Yurgens. Cleaning graphene using atomic force microscope. *Journal of Applied Physics*, 111(6):064904, 2012.
- [68] Youngwook Kim, Patrick Herlinger, Takashi Taniguchi, Kenji Watanabe, and Jurgen H. Smet. Reliable Postprocessing Improvement of van der Waals Heterostructures. *ACS Nano*, 13(12):14182–14190, 2019.

- [69] S. Link. *Intercalation of Graphene on SiC(0001): ultra-high doping levels and new 2D materials*. PhD thesis, University of Erlangen, 2017.
- [70] Claire Berger, Zhimin Song, Tianbo Li, Xuebin Li, Asmerom Y. Ogbazghi, Rui Feng, Zhenting Dai, Alexei N. Marchenkov, Edward H. Conrad, Phillip N. First, and Walt A. de Heer. Ultrathin Epitaxial Graphite: 2D Electron Gas Properties and a Route toward Graphene-based Nanoelectronics. *The Journal of Physical Chemistry B*, 108(52):19912–19916, 2004.
- [71] Konstantin V Emtsev, Aaron Bostwick, Karsten Horn, Johannes Jobst, Gary L Kellogg, Lothar Ley, Jessica L McChesney, Taisuke Ohta, Sergey a Reshanov, Jonas Röhrli, Eli Rotenberg, Andreas K Schmid, Daniel Waldmann, Heiko B. Weber, and Thomas Seyller. Towards wafer-size graphene layers by atmospheric pressure graphitization of silicon carbide. *Nature Materials*, 8(3):203–207, 2009.
- [72] B. Q. Lv, N. Xu, H. M. Weng, J. Z. Ma, P. Richard, X. C. Huang, L. X. Zhao, G. F. Chen, C. E. Matt, F. Bisti, V. N. Strocov, J. Mesot, Z. Fang, X. Dai, T. Qian, M. Shi, and H. Ding. Observation of Weyl nodes in TaAs. *Nature Physics*, 11(9):724–727, 2015.
- [73] Baiqing Lv, Tian Qian, and Hong Ding. Angle-resolved photoemission spectroscopy and its application to topological materials. *Nature Reviews Physics*, 1(10):609–626, 2019.
- [74] J. G. Bednorz and K. A. Müller. Possible high Tc superconductivity in the Ba-La-Cu-O system. *Z. Phys. B*, 64:189–193, 1986.
- [75] H. Eisaki, N. Kaneko, D. L. Feng, A. Damascelli, P. K. Mang, K. M. Shen, Z.-X. Shen, and M. Greven. Effect of chemical inhomogeneity in bismuth-based copper oxide superconductors. *Physical Review B*, 69(6):064512, 2004.
- [76] J Hoffman. Cuprate superconductors, web page at <http://hoffman.physics.harvard.edu/materials/Cuprates.php>, 2019.
- [77] David LeBoeuf, Nicolas Doiron-Leyraud, Julien Levallois, R. Daou, J.-B. Bonnemaïson, N. E. Hussey, L. Balicas, B. J. Ramshaw, Ruixing Liang, D. A. Bonn, W. N. Hardy, S. Adachi, Cyril Proust, and

- Louis Taillefer. Electron pockets in the Fermi surface of hole-doped high-Tc superconductors. *Nature*, 450(7169):533–536, 2007.
- [78] Patrick A. Lee, Naoto Nagaosa, and Xiao-Gang Wen. Doping a Mott insulator: Physics of high-temperature superconductivity. *Reviews of Modern Physics*, 78(1):17–85, 2006.
- [79] Stephen Blundell. *Magnetism in condensed matter*. Oxford University Press, Oxford, first edition, 2001.
- [80] A. Piriou, N. Jenkins, C. Berthod, I. Maggio-Aprile, and Ø. Fischer. First direct observation of the Van Hove singularity in the tunnelling spectra of cuprates. *Nature Communications*, 2(1):221, 2011.
- [81] R. S. Markiewicz. A survey of the Van Hove scenario for high- t_c superconductivity with special emphasis on pseudogaps and striped phases. *Journal of Physics and Chemistry of Solids*, 58(8):1179–1310, 1997.
- [82] Jacqueline Bouvier and Julien Bok. Van Hove singularity and “pseudo-gap” in HTSC. *Journal of Superconductivity*, 10(6):673–675, 1997.
- [83] Julien Bok and Jacqueline Bouvier. Superconductivity and the Van Hove Scenario. *Journal of Superconductivity and Novel Magnetism*, 25(3):657–667, 2012.
- [84] R. S. Markiewicz, I. G. Buda, P. Mistark, C. Lane, and A. Bansil. Entropic Origin of Pseudogap Physics and a Mott-Slater Transition in Cuprates. *Scientific Reports*, 7(1):44008, 2017.
- [85] H.-B. Yang, J. D. Rameau, P. D. Johnson, T. Valla, A. Tsvelik, and G. D. Gu. Emergence of preformed Cooper pairs from the doped Mott insulating state in $\text{Bi}_2\text{Sr}_2\text{CaCu}_2\text{O}_{8+\delta}$. *Nature*, 456(7218):77–80, 2008.
- [86] B. Keimer, S. A. Kivelson, M. R. Norman, S. Uchida, and Jan Zaanen. From quantum matter to high-temperature superconductivity in copper oxides. *Nature*, 518(7538):179–186, 2015.
- [87] Mark Buchanan. Mind the pseudogap. *Nature*, 409(6816):8–11, 2001.

- [88] Tom Timusk and Bryan Statt. The pseudogap in high-temperature superconductors: an experimental survey. *Reports on Progress in Physics*, 62(1):61–122, 1999.
- [89] Takasada Shibauchi, Lia Krusin-Elbaum, Ming Li, M. P. Maley, and P. H. Kes. Closing the Pseudogap by Zeeman Splitting in $\text{Bi}_2\text{Sr}_2\text{CaCu}_2\text{O}_{8+y}$ at High Magnetic Fields. *Physical Review Letters*, 86(25):5763–5766, 2001.
- [90] R. Daou, Nicolas Doiron-Leyraud, David LeBoeuf, S. Y. Li, Francis Laliberté, Olivier Cyr-Choinière, Y. J. Jo, L. Balicas, J.-Q. Yan, J.-S. Zhou, J. B. Goodenough, and Louis Taillefer. Linear temperature dependence of resistivity and change in the Fermi surface at the pseudogap critical point of a high- T_c superconductor. *Nature Physics*, 5(1):31–34, 2009.
- [91] Tomohiro Usui, Daiki Fujiwara, Shintaro Adachi, Hironobu Kudo, Kosuke Murata, Haruki Kushibiki, Takao Watanabe, Kazutaka Kudo, Terukazu Nishizaki, Norio Kobayashi, Shojiro Kimura, Kazuyoshi Yamada, Tomoyuki Naito, Takashi Noji, and Yoji Koike. Doping Dependencies of Onset Temperatures for the Pseudogap and Superconductive Fluctuation in $\text{Bi}_2\text{Sr}_2\text{CaCu}_2\text{O}_{8+\delta}$, Studied from Both In-Plane and Out-of-Plane Magnetoresistance Measurements. *Journal of the Physical Society of Japan*, 83(6):064713, 2014.
- [92] C. Collignon, S. Badoux, S. A. A. Afshar, B. Michon, F. Laliberté, Olivier Cyr-Choinière, J.-S. Zhou, S. Licciardello, Steffen Wiedmann, Nicolas Doiron-Leyraud, and Louis Taillefer. Fermi-surface transformation across the pseudogap critical point of the cuprate superconductor $\text{La}_{1.6-x}\text{Nd}_{0.4}\text{Sr}_x\text{CuO}_4$. *Physical Review B*, 95(22):224517, 2017.
- [93] N. Morozov, Lia Krusin-Elbaum, T. Shibauchi, L. N. Bulaevskii, M. P. Maley, Yu. I. Latyshev, and T. Yamashita. High-Field Quasiparticle Tunneling in $\text{Bi}_2\text{Sr}_2\text{CaCu}_2\text{O}_{8+\delta}$: Negative Magnetoresistance in the Superconducting State. *Physical Review Letters*, 84(8):1784–1787, 2000.
- [94] H Y Hwang, B Batlogg, H Takagi, H. L. Kao, J. Kwo, R. J. Cava, J. J. Krajewski, and W. F. Peck. Scaling of the temperature de-

- pendent Hall effect in $\text{La}_{2-x}\text{Sr}_x\text{CuO}_4$. *Physical Review Letters*, 72(16):2636–2639, 1994.
- [95] Julien Bok and Jacqueline Bouvier. Hall effect in the normal state of high- T_c cuprates. *Physica C: Superconductivity*, 408-410:242–243, 2004.
- [96] David LeBoeuf, Nicolas Doiron-Leyraud, B. Vignolle, Mike Sutherland, B. J. Ramshaw, J. Levallois, R. Daou, Francis Laliberté, Olivier Cyr-Choinière, Johan Chang, Y. J. Jo, L. Balicas, Ruixing Liang, D. A. Bonn, W. N. Hardy, Cyril Proust, and Louis Taillefer. Lifshitz critical point in the cuprate superconductor $\text{YBa}_2\text{Cu}_3\text{O}_y$ from high-field Hall effect measurements. *Physical Review B*, 83(5):054506, 2011.
- [97] S. Badoux, W. Tabis, F. Laliberté, G. Grissonnanche, B. Vignolle, D. Vignolles, J. Béard, D. A. Bonn, W. N. Hardy, R. Liang, Nicolas Doiron-Leyraud, Louis Taillefer, and Cyril Proust. Change of carrier density at the pseudogap critical point of a cuprate superconductor. *Nature*, 531(7593):210–214, 2016.
- [98] Wei Wu, Mathias S. Scheurer, Michel Ferrero, and Antoine Georges. Effect of Van Hove singularities in the onset of pseudogap states in Mott insulators. *Physical Review Research*, 2(3):033067, 2020.
- [99] D. V. Evtushinsky, A. A. Kordyuk, V. B. Zabolotnyy, D. S. Inosov, B. Büchner, H. Berger, L. Patthey, R. Follath, and S. V. Borisenko. Pseudogap-Driven Sign Reversal of the Hall Effect. *Physical Review Letters*, 100(23):236402, 2008.
- [100] K. Kechedzhi, E. McCann, V. I. Fal’ko, H. Suzuura, T. Ando, and B. L. Altshuler. Weak localization in monolayer and bilayer graphene. *The European Physical Journal Special Topics*, 148(1):39–54, 2007.
- [101] S Hikami, A. I. Larkin, and Y Nagaoka. Spin-Orbit Interaction and Magnetoresistance in the Two Dimensional Random System. *Progress of Theoretical Physics*, 63(2):707–710, 1980.
- [102] Matthias Kühne, Federico Paolucci, Jelena Popovic, Pavel M. Ostrovsky, Joachim Maier, and Jurgen H. Smet. Ultrafast lithium diffusion in bilayer graphene. *Nature Nanotechnology*, 12(9):895–900, 2017.

- [103] Gregory M. Stephen, Owen A. Vail, Jiwei Lu, William A. Beck, Patrick J. Taylor, and Adam L. Friedman. Weak Antilocalization and Anisotropic Magnetoresistance as a Probe of Surface States in Topological $\text{Bi}_2\text{TexSe}_{3-x}$ Thin Films. *Scientific Reports*, 10(1):4845, 2020.
- [104] B. L. Altshuler, A. G. Aronov, and P. A. Lee. Interaction Effects in Disordered Fermi Systems in Two Dimensions. *Physical Review Letters*, 44(19):1288–1291, 1980.
- [105] B. Jouault, B. Jabakhanji, N. Camara, W. Desrat, C. Consejo, and J. Camassel. Interplay between interferences and electron-electron interactions in epitaxial graphene. *Physical Review B*, 83(19):195417, 2011.
- [106] Johannes Jobst, Daniel Waldmann, Igor V. Gornyi, Alexander D. Mirlin, and Heiko B. Weber. Electron-Electron Interaction in the Magnetoresistance of Graphene. *Physical Review Letters*, 108(10):106601, 2012.
- [107] D. N. McIlroy, S. Moore, Daqing Zhang, J. Wharton, B. Kempton, R. Littleton, M. Wilson, T. M. Tritt, and C. G. Olson. Observation of a semimetal–semiconductor phase transition in the intermetallic ZrTe_5 . *Journal of Physics: Condensed Matter*, 16(30):359–365, 2004.
- [108] Yun Wu, Na Hyun Jo, Masayuki Ochi, Lunan Huang, Daixiang Mou, Sergey L. Bud’ko, P. C. Canfield, Nandini Trivedi, Ryotaro Arita, and Adam Kaminski. Temperature-Induced Lifshitz Transition in WTe_2 . *Physical Review Letters*, 115(16):166602, 2015.
- [109] Yan Zhang, Chenlu Wang, Li Yu, Guodong Liu, Aiji Liang, Jianwei Huang, Simin Nie, Xuan Sun, Yuxiao Zhang, Bing Shen, Jing Liu, Hongming Weng, Lingxiao Zhao, Genfu Chen, Xiaowen Jia, Cheng Hu, Ying Ding, Wenjuan Zhao, Qiang Gao, Cong Li, Shaolong He, Lin Zhao, Fengfeng Zhang, Shenjin Zhang, Feng Yang, Zhimin Wang, Qinjun Peng, Xi Dai, Zhong Fang, Zuyan Xu, Chuangtian Chen, and X. J. Zhou. Electronic evidence of temperature-induced Lifshitz transition and topological nature in ZrTe_5 . *Nature Communications*, 8(1):15512, 2017.

- [110] Pekka Pyykkö. Magically magnetic gadolinium. *Nature Chemistry*, 7(8):680, 2015.
- [111] Nikola Tesla. Valvular conduit, US Patent 1329559, 1920.
- [112] Iacopo Torre, Andrea Tomadin, Andre K. Geim, and Marco Polini. Nonlocal transport and the hydrodynamic shear viscosity in graphene. *Physical Review B*, 92(16):165433, 2015.
- [113] Jonathan Mayzel, Victor Steinberg, and Atul Varshney. Stokes flow analogous to viscous electron current in graphene. *Nature Communications*, 10:937, 2019.
- [114] Ronald Louis Bardell. *The Diodicity Mechanism of Tesla-Type No-Moving Parts Valves*. PhD thesis, University of Washington, 2000.
- [115] Kamran Behnia and Hervé Aubin. Nernst effect in metals and superconductors: a review of concepts and experiments. *Reports on Progress in Physics*, 79(4):046502, 2016.
- [116] M. Kim, S. G. Xu, A. I. Berdyugin, A. Principi, S. Slizovskiy, N. Xin, P. Kumaravadivel, W. Kuang, M. Hamer, R. Krishna Kumar, R. V. Gorbachev, K. Watanabe, T. Taniguchi, I. V. Grigorieva, V. I. Fal’ko, Marco Polini, and A. K. Geim. Control of electron-electron interaction in graphene by proximity screening. *Nature Communications*, 11:2339, 2020.
- [117] Jay L. Reed. Fluidic Rectifier, US Patent 5265636, 1993.
- [118] Denis A. Bandurin, Andrey V. Shytov, Leonid S. Levitov, Roshan Krishna Kumar, Alexey I. Berdyugin, Moshe Ben Shalom, Irina V. Grigorieva, Andre K. Geim, and Gregory Falkovich. Fluidity onset in graphene. *Nature Communications*, 9:4533, 2018.
- [119] Zibo Wang, Haiwen Liu, Hua Jiang, and X. C. Xie. Numerical study of negative nonlocal resistance and backflow current in a ballistic graphene system. *Physical Review B*, 100(15):155423, 2019.
- [120] Kristof Moors, Thomas L. Schmidt, and Oleksiy Kashuba. Supersonic flow and negative local resistance in hydrodynamic Dirac electron nozzles. *arXiv:1905.01247*, 2019.

- [121] M. Mendoza, H. J. Herrmann, and S. Succi. Preturbulent Regimes in Graphene Flow. *Physical Review Letters*, 106(15):156601, 2011.
- [122] Jan Zaanen. Planckian dissipation, minimal viscosity and the transport in cuprate strange metals. *SciPost Physics*, 6(5):061, 2019.
- [123] Andre K. Geim and K. S. Novoselov. The rise of graphene. *Nature Materials*, 6(3):183–191, 2007.
- [124] Cory R. Dean, L Wang, P. Maher, C Forsythe, F Ghahari, Y Gao, J Katoch, M Ishigami, Pilkyung Moon, Mikito Koshino, Takashi Taniguchi, K. Watanabe, Kenneth L. Shepard, J Hone, and Philip Kim. Hofstadter’s butterfly and the fractal quantum Hall effect in Moiré superlattices. *Nature*, 497(7451):598–602, 2013.
- [125] Yuan Cao, Valla Fatemi, Shiang Fang, Kenji Watanabe, Takashi Taniguchi, Efthimios Kaxiras, and Pablo Jarillo-Herrero. Unconventional superconductivity in magic-angle graphene superlattices. *Nature*, 556(7699):43–50, 2018.
- [126] D. C. Elias, R. R. Nair, T. M. G. Mohiuddin, S. V. Morozov, P. Blake, M. P. Halsall, A. C. Ferrari, D. W. Boukhvalov, Mikhail I. Katsnelson, A. K. Geim, and K. S. Novoselov. Control of Graphene’s Properties by Reversible Hydrogenation: Evidence for Graphane. *Science*, 323(5914):610–613, 2009.
- [127] Guoxing Li, Yuliang Li, Huibiao Liu, Yanbing Guo, Yongjun Li, and Daoben Zhu. Architecture of graphdiyne nanoscale films. *Chemical Communications*, 46(19):3256, 2010.
- [128] Andreas Hirsch. The era of carbon allotropes. *Nature Materials*, 9(11):868–871, 2010.
- [129] Albert Boretti, Sarim Al-Zubaidy, Miroslava Vaclavikova, Mohammed Al-Abri, Stefania Castelletto, and Sergey Mikhailovsky. Outlook for graphene-based desalination membranes. *npj Clean Water*, 1(1):5, 2018.